

Contents

1 Theory	3
1.1 Sesquioxides	3
1.1.1 Chromium Oxide	4
1.1.2 Gallium Oxide	6
1.2 X-ray Diffraction Principles	8
1.2.1 Scattering at Lattices	8
1.2.2 X-rays	9
1.3 Heteroepitaxy	10
1.3.1 Pseudomorphic Growth	10
1.3.2 Relaxed Growth	12
Dislocations	12
Slip Systems for Sesquioxide Heterostructures	13
2 Experimental Methods	15
2.1 Pulsed Laser Deposition	15
2.1.1 Setup	16
2.1.2 Plasma Dynamics	16
2.1.3 Segmented Target Approach	18
2.2 X-Ray Diffraction Measurement	18
2.2.1 2θ - ω -scans	19
2.2.2 ω -scans	20
2.2.3 φ -scans	21
2.2.4 Reciprocal Space Maps	21
2.2.5 Technical Aspects	24
2.3 Further Methods	24
2.3.1 Thermal Evaporation	24
2.3.2 Resistivity Measurement	25
2.3.3 Thickness Determination	26
2.3.4 Spectral Transmission	27
3 Experiment, Results and Discussion	29
3.1 Preliminary Investigations	29
3.1.1 Experiment	30
3.1.2 Results	30
Oxygen Partial Pressure Variation on <i>m</i> -plane Sapphire	30
Growth Temperature Variation on <i>m</i> -plane Sapphire	33
Influence of Growth Rate on Crystal Structure	35

	Deposition on <i>c</i> -, <i>r</i> -, <i>m</i> - and <i>a</i> -plane Sapphire	37
3.1.3	Conclusion	38
3.2	Doping of Cr ₂ O ₃ Thin Films	40
3.2.1	Experiment	40
3.2.2	Results	41
	Laser Position Variation for Different Targets	41
	Ohmic Contact Optimization	48
3.2.3	Conclusion	48
3.3	Strain Analysis	50
3.3.1	Experiment	50
	Sample Fabrication	50
	Measurements	51
3.3.2	Results	53
	<i>c</i> -plane: Laser Spot Size Variation	55
	<i>c</i> -plane: Pulse Energy Variation	57
	<i>r</i> -plane: Laser Spot Size Variation	59
	<i>r</i> -plane: Pulse Energy Variation	60
	<i>m</i> - and <i>a</i> -plane: Laser Spot Size Variation	62
	<i>m</i> - and <i>a</i> -plane: Pulse Energy Variation	63
3.3.3	Conclusion	66
3.4	Cr ₂ O ₃ Buffer Layers for α -Ga ₂ O ₃	68
3.4.1	Experiment	68
3.4.2	Results	69
3.4.3	Conclusion	73
	Appendices	77
	A Calculations	79
A.1	<i>m</i> -plane lattice constants	79
A.2	<i>a</i> -plane lattice constants	80
	B Figures	81
	Bibliography	87

Chapter 1

Theory

Contents

1.1	Sesquioxides	3
1.1.1	Chromium Oxide	4
1.1.2	Gallium Oxide	6
1.2	X-ray Diffraction Principles	8
1.2.1	Scattering at Lattices	8
1.2.2	X-rays	9
1.3	Heteroepitaxy	10
1.3.1	Pseudomorphic Growth	10
1.3.2	Relaxed Growth	12

1.1 Sesquioxides

Transparent Conductive Oxides (TCOs) are materials that combine the properties of having low absorption coefficient in the visible spectrum and being conductive at the same time [1]. The interest in these materials is motivated by possible applications in portable and flexible electronics [2], displays [3], solar cells [4] and more [1]. Not only the focus on a small number of materials in the past (SnO_2 , In_2O_3 , ZnO) [1], but also the scarcity and concerns about availability⁽¹⁾ of fundamental compounds [5] increases the demand for new materials. This includes fabrication of *p*-type TCOs as well as compounds with even larger band gaps than 3 eV, called Ultrawide-bandgap (UWBG) materials. Because the critical electrical field – at which breakdown occurs – is depending on the band gap [6], UWBG materials can serve for high-power electronic devices as well as for deep ultra-violet (UV) optoelectronics [7]. Candidates for this material class are group-III sesquioxides⁽²⁾, of which Ga_2O_3 with its several polymorphs

⁽¹⁾ China controls 75 % of the world's indium reserves, and limited the export of this material already in the past [5].

⁽²⁾ A sesquioxide is an oxide with formula unit Me_2O_3 , where Me is a metal with oxidation state +3. Transition metal sesquioxides are, e.g., Y_2O_3 , Rh_2O_3 or In_2O_3 .

[8] recently gained interest in the scientific community – in particular the metastable corundum structured $\alpha\text{-Ga}_2\text{O}_3$.

The sesquioxide Cr_2O_3 , being a possible *p*-type TCO, is isomorphic to group-III sesquioxide $\alpha\text{-Ga}_2\text{O}_3$ with quite similar lattice parameters (cf. Tab. 1.1). This enables the use of Cr_2O_3 as a buffer layer between $\alpha\text{-Ga}_2\text{O}_3$ and isomorphic $\alpha\text{-Al}_2\text{O}_3$ (sapphire) substrates to improve the deposition process [9]. The lower band gap also makes band gap engineering with isostructural sesquioxides possible [10] and finally, Cr_2O_3 exhibits increased conductivity upon doping [11] and could thus serve as *p*-type component in a *p-n*-heterojunction with $\alpha\text{-Ga}_2\text{O}_3$. In the following, an overview of the two mentioned sesquioxides will be presented with focus on the physical properties being relevant to this work.

1.1.1 Chromium Oxide

“Chromia” or “Eskolaite” is a sesquioxide composed of the transition metal chromium and oxygen with formula unit Cr_2O_3 . Among other chromium oxides (e.g. metallic CrO_2 , toxic CrO_3 etc.), it is the thermodynamically most stable phase [12–14], making it the abundant chromium oxide on earth [15]. Cr_2O_3 occurs in the α -phase⁽³⁾ and henceforth, “ Cr_2O_3 ” will refer to this phase.

As coating material, Cr_2O_3 is commonly used due to its high hardness [17], sufficient transparency for low thicknesses [18] as well as its resistance against corrosion and oxidation [19]. This also explains its use-case as component of stainless steel to form passive films [14]. Cr_2O_3 thin films absorb electromagnetic waves with wavelengths smaller than 400 nm, making it opaque in the UV-spectrum [20, 21]. It is transparent in the visible spectrum with, e.g., a reported transmittance of 40 % at 700 nm for 0.5 μm thick films by Cheng *et al.* (1996) [20].

Cr_2O_3 crystallizes in the corundum structure, which has trigonal symmetry (space group $R\bar{3}c$) and belongs to the hexagonal crystal family. One unit cell contains six formula units, i.e. 12 chromium cations and 18 oxygen anions [14]. The oxygen atoms arrange in a hexagonal close-packed manner, where two thirds of the formed octahedrons are filled with Cr atoms [22]. The unit cell is spanned by a principal axis, called *c*-axis⁽⁴⁾, and a hexagonal basal plane with lattice constant *a*. The numerical values for those lattice parameters differ depending on the publication [9, 15, 23–25], and henceforth the values in Tab. 1.1 will be used [15, 26, 27].

Several techniques combined with various substrates were applied for depositing chromia thin films, including: Chemical Vapor Deposition (CVD) on silicon Si(111) [28, 29] and glass [20], Molecular Beam Epitaxy (MBE) on *c*-plane sapphire [23, 30], thermal evaporation on platinum Pt(111) [12], electron-beam evaporation on glass [13], spray pyrolysis on glass [31], radio-frequency (RF) sputtering on *c*-plane sapphire [9, 32] and *r*-plane sapphire [33], reactive direct current (DC) sputtering on glass [21], reactive Pulsed Laser Deposition (PLD) on silicon Si(100) [34] and *r*-plane sapphire

⁽³⁾ Only one study is known to the author that states another cubic spinel γ -phase with random missing Cr point defects [12]. This information is based on Wyckoff (1963) [16], but the source is not available, so no further information can be given about the stability or other properties of this potential phase.

⁽⁴⁾ The spins of the Cr atoms along this direction are alternating $3 \uparrow$ and $3 \downarrow$ [23], making the crystal antiferromagnetic [14, 22].

	<i>a</i>	<i>c</i>	Ref.
$\alpha\text{-Al}_2\text{O}_3$	4.76 Å	13.00 Å	Pishchik <i>et al.</i> (2009) [26]
$\alpha\text{-Cr}_2\text{O}_3$	4.96 Å	13.59 Å	Mi <i>et al.</i> (2018) [15]
$\alpha\text{-Ga}_2\text{O}_3$	4.98 Å	13.43 Å	Marezio and Remeika (1967) [27]

Table 1.1: Lattice constants of selected corundum structured sesquioxides.

[35], and non-reactive PLD on *c*-plane sapphire [23, 36, 37]. The first deposition via PLD was done by Tabbal *et al.* (2006) [38].

Electronic Structure Experimental and theoretical studies reveal that chromia exhibits a band gap of 3.2 to 3.4 eV [12, 14, 15, 25] making it a wide band gap material. Its insulating behavior [25] is classified as both Mott-Hubbard type and charge-transfer type, which are models to describe the electronic behavior of compounds containing transition metals with partly filled $3d^n$ orbitals⁽⁵⁾ [14, 15, 22]: Density Functional Theory (DFT) calculations show that the Cr-3d states are almost solely responsible for electronic states in the conduction band and that they are also present in the valence band [14, 15]. Thus, $3d \rightarrow 3d$ band transitions are possible, favoring the Mott-Hubbard model of this compound [14]. Furthermore, the O-2p states are mainly present in the valence band, at similar energies as the Cr-3d states, which leads to hybridization and thus favoring the charge-transfer model [14].

However, several studies agree on Cr_2O_3 being a semiconductor with *p*-type conductivity⁽⁶⁾ at room temperature and atmospheric conditions [14, 15, 20, 32, 34, 36, 40]. Calculating the impact of different crystal point defects on the band structure may give insight into these observations. Indeed, when considering a missing chromium atom (“vacancy” V_{Cr}) the band structure changes in two ways: The band gap itself is reduced [15], but not sufficiently to make excitations of valence electrons into the conduction band more probable than for defectless chromia. Additionally, there is a new defect band introduced slightly above the Fermi level (cf. Fig. 1.1), which acts as an unoccupied acceptor level [15]. This defect state is mainly composed of O-2p orbitals of the oxygen anions surrounding the vacancy [14]. Effectively, a missing neutral chromium atom removes the Cr^{3+} cation as well as three electrons bound to the adjacent O^{2-} anions, thus creating three holes [14] explaining the *p*-type conductivity.

Note that there are also other possible defects with different effects: a chromium FRENKEL point defect describes a Cr atom leaving its position and occupying a formerly unoccupied cavity in one of the oxygen-octahedrons. This FRENKEL defect creates a new band below the Fermi level, acting as an occupied donor level [14]. A similar defect state is introduced by oxygen vacancies [15]. Note that the Fermi level is located only slightly above the Valence Band Maximum (VBM) and thus the new occupied donor level is not significantly closer to the Conduction Band Minimum (CBM), which

⁽⁵⁾ $n = 5$ for Cr.

⁽⁶⁾ Cheng *et al.* (2001) [39] actually find Cr_2O_3 to be insulating. It is noted that they examined Cr_2O_3 as an 2 nm thick oxide surface on CrO_2 films deposited by CVD. Farrell *et al.* (2015) [30] also find that their high quality epitaxial films of Cr_2O_3 grown by MBE exhibit no *p*-type conductivity. Similar results were found by Kehoe *et al.* (2016) [23] for MBE and PLD deposited films.

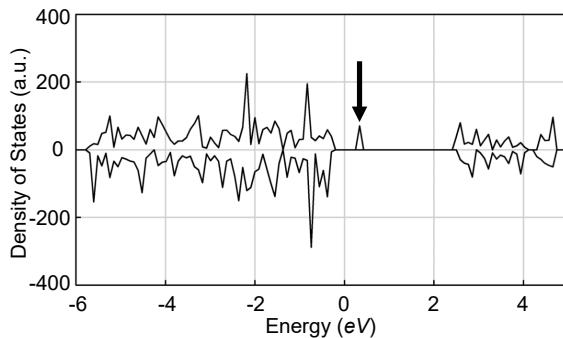


Figure 1.1: Calculated density of states (DOS) of chromia, taking a V_{Cr} into account. The arrow marks the new acceptor level. Reprinted with permission from Lebreau *et al.* (2014) [14]. Copyright © 2014 American Chemical Society.

means that electrons still have to overcome the band gap energy to get into conducting states. This favors the formation of holes via Cr vacancies ($\text{O}-2p$ acceptor states) rather than electrons via Cr Frenkel defects and O vacancies (Cr- $3d$ donor states).

Doping Several attempts have been made to alter the conductivity of chromia thin films deliberately, including incorporation of magnesium [11, 30, 31], nickel [37], or lithium [41, 42] to achieve better p -type conductivity

On the other hand, incorporation of titanium yields electrons as majority carriers [43] due to the higher valent state of Ti when substituting Cr sites (Ti_{Cr}) [40].

Due to interest in the electrical properties of p -type TCOs, the influence on Mg-doped Cr_2O_3 thin films has been investigated by several studies [11, 23, 25, 30, 31, 37, 43]. Substituting Cr atoms with less valent hole providers – compared to structural defects of pure Cr_2O_3 – does not only allow for a more controlled defect incorporation, but is also energetically more favorable due to a lower formation energy of Mg_{Cr} compared to V_{Cr} [23]. Uekawa and Kaneko (1996) [11] report an increase in conductivity of five orders of magnitude for $\text{Cr}_2\text{O}_3:\text{Mg}$ thin films prepared by the polymer precursor method. This result can be further improved by postannealing [30] and deposition at higher oxygen partial pressures [30, 43]. These effects are attributed to homogenization of magnesium inside the thin films and increased MgO incorporation during deposition, respectively. An observed side-effect of Mg-doping is a color change to a brownish tint [11, 25]. Uekawa and Kaneko (1996) [11] discuss that this may be the result of a mixed valence state of chromium (Cr^{4+} or Cr^{6+}), formed upon doping, as observed by X-ray Photoelectron Spectroscopy (XPS). This may establish an unoccupied state, favoring charge-transfer transitions from $\text{O}-2p$ orbitals to this low-energetic state, resulting in a different visual appearance of the thin films. However, it has been shown that the overall transparency can be increased by codoping of Mg with nitrogen which also reduces the decolorization substantially [25, 31].

1.1.2 Gallium Oxide

Ga_2O_3 is a group-III sesquioxide with four⁽⁷⁾ different polymorphs, of which $\beta\text{-}\text{Ga}_2\text{O}_3$

⁽⁷⁾ Five, if the δ -phase is not considered as a form of the α -phase [8].

is the thermodynamically most stable one at ambient conditions [8, 44, 45]. The corundum-structured α -Ga₂O₃ phase, which is of most relevance for this work, is isomorphic to Cr₂O₃ (cf. 1.1.1), with lattice parameters as listed in Tab. 1.1. α -Ga₂O₃ is thermodynamically metastable [46], i.e. the phase can exist under ambient conditions, even though β -Ga₂O₃ has a lower energy state up to 1800 °C [47]. The thermodynamic equilibrium – which determines the favored phase – can also be changed by strain due to lattice mismatch occurring during heteroepitaxy⁽⁸⁾. [45] This approach is of particular interest due to the possibility of deposition on cheap⁽⁹⁾ and readily available sapphire substrates which are isomorphic to α -Ga₂O₃ [33, 46, 47]. Note that deposition of β -Ga₂O₃ on sapphire is also possible, but only with restriction to formation of more than one crystal domain [48]. On the other hand, highly crystalline [47] α -Ga₂O₃ thin films can be grown without rotational domains [45, 48].

Deposition of α -Ga₂O₃ on sapphire has been done by several deposition techniques, including [48]: Halide Vapor Phase Epitaxy (HVPE), mist CVD [49], MBE [44], Atomic Layer Deposition and metalorganic CVD. Phase-pure deposition via PLD has also been achieved [44, 45, 50]. Despite being isomorphic to each other, α -Ga₂O₃ and sapphire still exhibit a lattice mismatch of around 4.8% along the *a*-axis [46]. This induces semicoherent growth with a fairly high dislocation density, which has been reported to be around $7 \times 10^{10} \text{ cm}^{-2}$ [49]. In particular, this becomes a problem regarding carrier mobility which is tremendously hindered by dislocation scattering [46].

To overcome the problems of lattice mismatch between sapphire substrates and α -Ga₂O₃ thin films, quasi-continuous gradients from Al₂O₃ to α -Ga₂O₃ have been applied, utilizing the capability of alloying the respective compounds [51]. Furthermore, buffer layers of isomorphic Cr₂O₃ have been used to decrease the high dislocation density for deposition on *c*-oriented [9, 32] as well as *r*-oriented sapphire [33]. Deposition on other than *c*-oriented substrates also decreases parasitic phases because of the suppression of *c*-plane facets on *m*- and *a*-plane sapphire [52]. Deposition on prismatic *m*-plane sapphire also yields much higher carrier mobilities when compared to *c*-plane sapphire [53]. It has to be noted that despite the difficulties occurring upon lattice mismatch, pseudomorphic growth seems to be feasible without buffer layers for different deposition techniques, at least for some monolayers [44].

With 5.0 to 5.3 eV [48], α -Ga₂O₃ has the highest band gap of the four polymorphs [47]. Band gap engineering is possible by alloying with Al₂O₃ [52] or In₂O₃ [54]. The crystal structure also allows for alloying with other corundum structured compounds [48], in particular other transition metal oxides such as Cr₂O₃ [32, 33]. The conduction band is mainly composed of Ga-4s states with an effective electron mass of $0.3 m_e$. The valence band is very flat and mainly composed of O-2p orbitals, yielding a high effective electron mass and thus strong localization [47]. This hinders the realization of *p*-type α -Ga₂O₃. Next to band gap engineering, *n*-type doping via Sn, Si and Ge [50], as well as Zr [55] incorporation has been accomplished.

⁽⁸⁾ However, the possibility of formation of parasitic β -phase still has to be taken into account [45].

⁽⁹⁾ Compared to bulk β -Ga₂O₃ substrates [46, 48].

1.2 X-ray Diffraction Principles

1.2.1 Scattering at Lattices

To elucidate the working principles behind X-ray diffraction (XRD) as a measurement method (cf. 2.2), a brief description of reciprocal space and constructive interference will be provided. Those derivations are based on Ashcroft and Mermin (1976) [56].

A periodic point-like structure with translational symmetry (“BRAVAIS lattice”) can be described by three vectors \mathbf{a}_i that span a so-called “unit cell”. Every lattice point \mathbf{R} is a linear combination of those unit cell vectors. For such a lattice, there exists a so-called “reciprocal lattice”, which consists of all vectors \mathbf{K} satisfying the condition⁽¹⁰⁾:

$$e^{i\langle \mathbf{K}, \mathbf{R} \rangle} = 1, \quad (1.1)$$

$$\Leftrightarrow \langle \mathbf{K}, \mathbf{R} \rangle = 2\pi m, \quad (1.2)$$

with $m \in \mathbb{N}$. This is again a BRAVAIS lattice with unit cell vectors \mathbf{a}_j^* :

$$\mathbf{K}_{hkl} = h\mathbf{a}_1^* + k\mathbf{a}_2^* + l\mathbf{a}_3^*. \quad (1.3)$$

It follows that for any i, j :

$$\langle \mathbf{a}_i^*, \mathbf{a}_j \rangle = 2\pi\delta_{ij}, \quad (1.4)$$

with the KRONECKER delta δ_{ij} . A major application of reciprocal space vectors is their ability to describe lattice planes. Any lattice plane can be described by the shortest possible reciprocal space vector \mathbf{K}_{hkl} perpendicular to it. Consequently, the lattice plane is denoted by (hkl) . The distance between equivalent lattice planes can be calculated via

$$d_{hkl} = |\mathbf{K}_{hkl}|^{-1}. \quad (1.5)$$

Note that for non-cubic crystals, the lattice plane (hkl) is in general *not* perpendicular to the lattice direction $[hkl]$.

With those preliminaries, the conditions for constructive interference during diffraction of radiation at BRAVAIS lattices can be derived. Consider two scattering centers separated by \mathbf{d} (Fig. 1.2) and incident radiation with wave vector \mathbf{k} :

$$\mathbf{k} = \frac{2\pi}{\lambda}\hat{\mathbf{n}}, \quad (1.6)$$

with wavelength λ and direction $\hat{\mathbf{n}}$. For the case of elastic scattering, the outgoing wave vector \mathbf{k}' has the same wavelength λ but different direction $\hat{\mathbf{n}'}$. The phase difference of two photons scattered at the 1st and 2nd scattering center, respectively, can be calculated from their path difference, which reads

$$\langle \mathbf{d}, \hat{\mathbf{n}} \rangle + \langle -\mathbf{d}, \hat{\mathbf{n}'} \rangle. \quad (1.7)$$

Constructive interference occurs, if the phase difference is an integral multiple of the wavelength, so it must follow that

$$\langle \mathbf{d}, (\hat{\mathbf{n}} - \hat{\mathbf{n}'}) \rangle = m\lambda \quad (1.8)$$

$$\Leftrightarrow \langle \mathbf{d}, (\hat{\mathbf{k}} - \hat{\mathbf{k}'}) \rangle = 2\pi m, \quad (1.9)$$

⁽¹⁰⁾ The definition of \mathbf{K} by (1.1) is a consequence of demanding that the plane wave described by $f_{\mathbf{K}}(\mathbf{r}) = \exp(i\langle \mathbf{K}, \mathbf{r} \rangle)$ has the same symmetry as the BRAVAIS lattice [56].

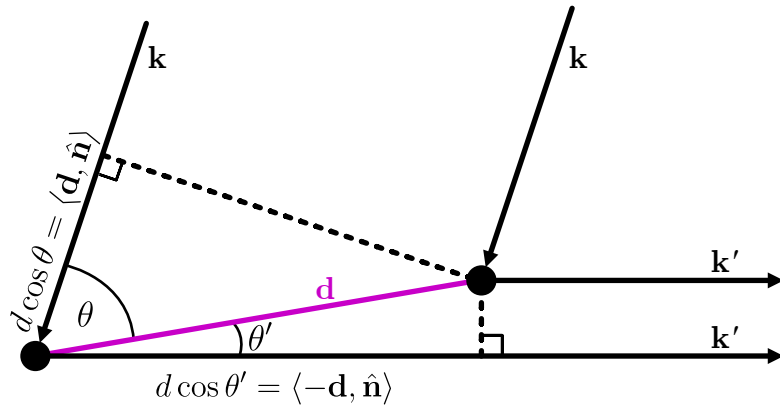


Figure 1.2: The geometry of two scattering centers displaced by \mathbf{d} , as well as incident and reflected X-rays \mathbf{k} and \mathbf{k}' , respectively.

with $m \in \mathbb{N}$. Comparing with Equ. (1.2) reveals that $\hat{\mathbf{k}} - \hat{\mathbf{k}'}$ is a reciprocal space vector, because the separation \mathbf{d} of the two scattering centers is a lattice vector \mathbf{R} . So constructive interference (observing a reflection) occurs if and only if the scattering geometry (determined by angle of incidence and refraction, as well as wavelength) matches the lattice symmetry in the sense that there is a corresponding lattice translation vector \mathbf{d} fulfilling Equ. (1.9). Thus, from the position of reflections in reciprocal space, one can deduce the lattice symmetry.

Note that this description of X-ray scattering is equivalent to the BRAGG condition:

$$m\lambda = 2d_{hkl} \sin(\theta), \quad (1.10)$$

where the angle of incidence θ and λ are contained in $\hat{\mathbf{k}} - \hat{\mathbf{k}'}$. Furthermore, when a lattice point is not equivalent to a single atom, but represents several scattering centers, an additional geometrical structure factor has to be taken into account to determine whether a certain geometry allows reflexes. This is important, e.g., for structures with trigonal symmetry. They are described with a conventional hexagonal unit cell, although not every plane (hkl) exhibits constructive interference⁽¹¹⁾.

1.2.2 X-rays

Atomic distances in solids are of the order of several Å, so the radiation for probing those structures must have a similarly sized wavelength, which is fulfilled by X-rays [58]. The following description of X-rays is based on Spieß (2009) [59].

The basis of any X-ray tube are high-energy electrons which are produced by thermionic emission in a cathode, which is usually made out of tungsten⁽¹²⁾. An electric field of several kV accelerates the electrons to the anode, where they are stopped such that around 99 % of their kinetic energy dissipates. The momentum change of electrons,

⁽¹¹⁾ The condition for allowed reflections is $-h + k + l = 3n$, with $n \in \mathbb{N}_0$ [57].

⁽¹²⁾ Tungsten is the element with the second highest melting point of around 3400 °C. This ensures a low contamination of the anode with cathode material, reducing the intensity of observed peaks in XRD patterns that correspond to tungsten (cf. 2.2).

which are charged particles, leads to emission of bremsstrahlung. Furthermore, the electrons ionize atoms of the anode material which leads to unoccupied electron states. If those states are filled by electrons with higher quantum number n , the difference in energy of those levels is emitted as radiation with a discrete spectrum, called characteristic X-ray. Important for XRD measurements is a part of the characteristic spectrum, called K-radiation, which originates in occupation of empty $1s$ -orbitals. The occupying electron must come from an orbital with angular momentum quantum number $l = 1$, i.e. a p -orbital, because Δl cannot be zero for intraatomic electron transitions. The radiation is termed $K\alpha$ - or $K\beta$ -radiation, depending on whether the previous orbital was $2p$ or $3p$, respectively. Furthermore, one distinguishes $K\alpha_1$ - and $K\alpha_2$ -radiation, depending on the magnetic quantum number of the previous orbital, which can be $\frac{3}{2}$ or $\frac{1}{2}$, respectively. $K\alpha$ -radiation is desired for probing crystal structures.

1.3 Heteroepitaxy

1.3.1 Pseudomorphic Growth

When a body is deformed (“strained”) from its original state of equilibrium (“bulk”), forces will arise that tend to return the body to this equilibrium. Molecular forces are the driving element behind these stresses [60]. In continuum mechanics, stress σ_{ij} and strain ϵ_{kl} are symmetric rank-2 tensors that are linearly connected by the elasticity tensor with components C_{ijkl} :

$$\sigma_{ij} = \sum_{k,l} C_{ijkl} \epsilon_{kl}. \quad (1.11)$$

Note that Equ. (1.11) represents a set of 9 linear equations.

If the in-plane (i.p.) lattice constants of two isomorphic compounds match at the interface of a heterostructure, one refers to “pseudomorphic” growth. This confines a part of the system of equations (1.11):

1. The thin film i.p. lattice constants have to match the substrate i.p. lattice constants. This defines the magnitude of i.p. strain of the thin film material.
2. On the other hand, due to vertical growth, the out-of-plane (o.o.p.) stress of the thin film is demanded to be zero.

The resulting o.o.p. strain as well as non-diagonal strain components can be derived by solving the system of equations (1.11) with these two boundary conditions. In Grundmann (2018) [61], formulas are derived for the unknown strains in the special case of pseudomorphic heterostructures with threefold rhombohedral symmetry. For quantitative predictions of those strains, the elasticity tensor C_{ijkl} of the thin film compound has to be known. Depending on the symmetry of the crystal structure, its components collapse into a lower number of independent entries⁽¹³⁾: for rhombohedral crystals, six independent components are left [56]. The entries of the elasticity tensor of the two sesquioxides important for this work are given in Tab. 1.2.

⁽¹³⁾ Due to symmetry reasons [56], the nine indices ij of the strain tensor can be unambiguously expressed by one index with six possible values: $11 \rightarrow 1, 22 \rightarrow 2, 33 \rightarrow 3, 23 \rightarrow 4, 13 \rightarrow 5, 12 \rightarrow 6$ [61]. This allows for a 6×6 -matrix representation of the elasticity tensor $C_{ijkl} \rightarrow C_{\mu\nu}$.

Table 1.2: The six independent entries of the elasticity tensor for rhombohedral Cr₂O₃ [62] and α -Ga₂O₃ [61]. All values are in units of 100 GPa.

Material	C_{11}	C_{12}	C_{13}	C_{33}	C_{44}	C_{14}
α -Cr ₂ O ₃	3.74	1.48	1.75	3.62	1.59	-0.19
α -Ga ₂ O ₃	3.82	1.74	1.26	3.46	0.78	-0.17

Because of its direct influence on the o.o.p. lattice plane distance and thus on the XRD patterns of 2 θ - ω -scans (cf. 2.2), the strain component perpendicular to the sample surface, ϵ_{zz} , is of particular interest. In the following, the formulas for the case of rhombohedral crystal structures are stated as derived in Grundmann (2018) [61]. They depend on the respective i.p. strains ϵ_{xx} and ϵ_{yy} caused by the lattice mismatch between film and substrate. Note that here, $\mathbf{r} = (x, y, z)$ describes coordinates in the laboratory system – in contrary to Ref. [61], where \mathbf{r} and \mathbf{r}' are used to describe cartesian coordinates in the crystal and laboratory system, respectively.

One derives for (11.0)-plane (a -orientation):

$$\epsilon_{zz,a} = -\frac{C_{13}\epsilon_{xx,a} + C_{12}\epsilon_{yy,a}}{C_{11}}, \quad (1.12)$$

for (10.0)-plane (m -orientation):

$$\epsilon_{zz,m} = -\frac{C_{13}C_{44}\epsilon_{xx,m} + (C_{12}C_{44} + C_{14}^2)\epsilon_{yy,m}}{C_{11}C_{44} - C_{14}^2}, \quad (1.13)$$

and for (00.1)-plane (c -orientation):

$$\epsilon_{zz,c} = -\frac{2C_{13}}{C_{33}}\epsilon_{yy,c}, \quad (1.14)$$

with $\epsilon_{xx,a} = c_S/c_F - 1$ and $\epsilon_{yy,a} = a_S/a_F - 1$, depending on the lattice parameters of substrate (a_S , c_S) and film (a_F , c_F). Note that

$$\begin{aligned} \epsilon_{xx,a} &= \epsilon_{xx,m}, \\ \epsilon_{yy,a} &= \epsilon_{yy,m}, \\ \epsilon_{yy,c} &= \epsilon_{yy,a}. \end{aligned}$$

For (01.2)-plane (r -orientation), more complex relations arise as it was demonstrated by Grundmann (2020) [63]. The distance of lattice planes d orthogonal to the sample surface are then strained, such that:

$$d_{\text{strained}} = d(1 + \epsilon_{zz}). \quad (1.15)$$

Assuming pseudomorphic growth of Cr₂O₃ on Al₂O₃, one can compare the strained lattice plane distances to the unstrained bulk values, by utilizing (1.15). The numerical values, calculated from the lattice constants (Tab. 1.1) and the elasticity tensor (Tab. 1.2), are listed in Tab. 1.3a.

Table 1.3: (a) Comparison of d and d_{str} , which are the o.o.p. lattice plane distances for bulk Cr₂O₃ and pseudomorphic Cr₂O₃ on Al₂O₃, respectively. The corresponding o.o.p.-strain ϵ_{zz} is also given, as well as the corresponding angles of typical reflections in diffraction patterns of 2θ-ω-scans. (b) The resulting tilt of the thin film depending on substrate orientation for relaxed growth. The results follow from considerations on the possible slip systems and BURGER's vectors.

Orientation (X-ray reflection)	(a) Pseudomorphic				(b) Relaxed	
	d (nm)	d_{str} (nm)	ϵ_{zz} (%)	2θ (°)	$2\theta_{\text{str}}$ (°)	$\theta_{T,x}$
c (00.6)	13.59	14.12	3.90	39.75	38.20	—
a (11.0)	2.48	2.57	3.63	36.18	34.87	no
m (30.0)	4.30	4.45	3.67	65.06	62.49	yes
r (02.4)	3.63	3.72	2.41	50.19	48.93	yes

1.3.2 Relaxed Growth

Dislocations

When the lattice mismatch is not resolved by adaption to the substrate (cf. 1.3.1), the strain is relieved by formation of “dislocations”, which facilitate a relaxed growth mode of the film [64]. The highest disturbance from equilibrium spacing occurs close to the “dislocation line” which extends through the material – far away from this line, the crystallinity is restored. In which fashion the distortion happens, can be characterized by the BURGER's vector \mathbf{b} . The relation of the BURGER's vector to the dislocation line determines the type of the dislocation: if they are orthogonal, one refers to an *edge* dislocation; if they are parallel, one refers to a *screw* dislocation. For a “perfect” dislocation⁽¹⁴⁾, the BURGER's vector is a lattice translation vector. Note that in general, dislocations exhibit both edge- and screw-character [66].

Dislocations are not static, but can move (“glide”) inside the crystal. The movement happens typically inside a plane which has highest density of atoms (“glide plane”) and along the BURGER's vector which is responsible for the dislocation [66]. The arrangement of glide plane and direction of movement is called “slip system”, e.g. for hexagonal structures, one finds {00.1}/⟨11.0⟩ to be one prevailing slip system [66].

For some slip systems occurring on heterostructures, the relaxation results in an additional tilt of the deposited film. This happens because a BURGER's vector \mathbf{b} has more than one component: the edge component b_{\parallel} causes strain relaxation along b_{\parallel} ; but if \mathbf{b} also exhibits a component b_{\perp} orthogonal to the sample surface and the dislocation line, a tilt angle θ_T will result between substrate and relaxed film [64, 67]:

$$\theta_{T,i} = \epsilon_{ii} \frac{b_{i,\perp}}{b_{i,\parallel}}, \quad (1.16)$$

where i denotes the axis of strain relaxation. This is schematically depicted in Fig. 1.3. Note that Equ. (1.16) is formulated for partially relaxed systems in Kneiß *et al.* (2021) [64], but here the relaxation parameter ρ_i was omitted, therefore assuming fully relaxed thin films.

⁽¹⁴⁾ Also referred to as “full” dislocation [65].

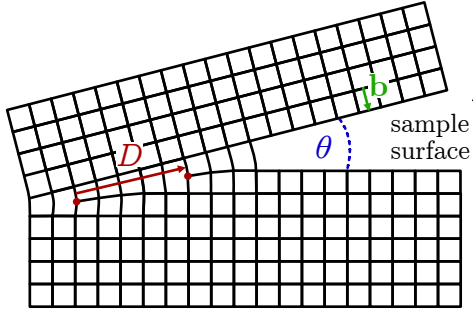


Figure 1.3: Edge dislocation with BURGER’s vector perpendicular to the sample surface. The edge dislocation lines are indicated by the red dots and are perpendicular to the image plane. Consequently, the direction of the edge BURGER’s vector is indicated by the red arrow, whose length D denotes the distance between dislocation lines. The green BURGER’s vector \mathbf{b} is the orthogonal component b_{\perp} mentioned in the text.

Slip Systems for Sesquioxide Heterostructures

For heteroepitaxial growth of $(\text{Al}_x\text{Ga}_{1-x})_2\text{O}_3$ with low Al content on Al_2O_3 , studies have been conducted on the prevailing relaxation mechanisms for r -oriented [67, 68], as well as a - and m -oriented [64] growth directions. In the following, those results will be summarized. Note that the x -axis points along the c -axis for m - and a -oriented heterostructures, and similarly along the projection of the c -axis on the sample surface for r -oriented heterostructures.

(01.2)-plane (r -orientation) The two relevant slip systems are $\{00.1\}/\frac{1}{3}\langle11.0\rangle$ and $\{11.0\}/\frac{1}{3}\langle\bar{1}\bar{1}.1\rangle$, which contain the “basal” and “prismatic” glide plane, respectively [67]. The former allows relaxation along the direction containing the projection of the c -axis (x -axis), whereas the latter allows relaxation perpendicular to it (y -axis). For the basal system, one can determine two possible independent BURGER’s vectors \mathbf{b}_c with differing screw components but otherwise same tilt and edge components $b_{c,\perp}$ and $b_{c,\parallel}$, respectively. The tilt along x -direction can then be calculated via:

$$\theta_{T,x} = \epsilon_{xx} \frac{b_{c,\perp}}{b_{c,\parallel}} = \frac{1}{\sqrt{3}} \zeta_F \epsilon_{xx}. \quad (1.17)$$

with $\zeta_F = c_F/a_F$. For the prismatic slip system, the possible BURGER’s vectors facilitate relaxation along the y -direction via $b_{a,\parallel}$. But in contrast to the basal system, the tilt components $b_{a,\perp}$ cancel out on average, thus resulting in no net tilt along the y -direction: $\theta_{T,y} = 0$.

(10.0)-plane (m -orientation) Neither basal (00.1) nor prismatic (11.0) and (10.0) slip systems can resolve strain along the x -axis: The (00.1)-plane is perpendicular to the surface and x -direction, thus the BURGER’s vector can only have components in the y - z -plane. But for strain release along x , the BURGER’s vector should have non-zero component in this direction, which cannot be the case. The prismatic planes, on the other hand, are perpendicular to the surface but parallel to the x -axis. This results in a dislocation line along the x -direction. To release strain, the BURGER’s vector would

have x -component, which does not apply for edge dislocations. So the prevailing slip system must have (01.2)-plane (r -orientation) or (11.2)-plane (s -orientation) character, which are called “pyramidal” slip systems. Three different r -planes contribute to strain release, because there is dislocation line component along the y -axis and BURGER’s vector’s components along the x -axis. With Equ. (1.16) and substituting the possible BURGER’s vectors one finds:

$$\theta_{T,x} = \frac{2}{3} \frac{\sqrt{3}}{\frac{20\zeta}{24+6\zeta^2} + \zeta} \left(\frac{c_S}{c_F} - 1 \right) \quad (1.18)$$

(11.0)-plane (a -orientation) The same argument as for the m -oriented heterostructure holds, why only pyramidal slip systems are possible. But in this case, only two r -planes contribute to strain relaxation, because the third plane is perpendicular to the surface, thus can only exhibit BURGER’s vectors without in-plane components which results in no possible edge dislocations. Furthermore, in this case, the BURGER’s vectors of the two remaining r -planes have opposite tilt components, i.e. they point outwards and inwards of the surface, respectively. Regarding Equ. (1.16), this will result in no net tilt of the thin film.

Chapter 2

Experimental Methods

Contents

2.1 Pulsed Laser Deposition	15
2.1.1 Setup	16
2.1.2 Plasma Dynamics	16
2.1.3 Segmented Target Approach	18
2.2 X-Ray Diffraction Measurement	18
2.2.1 2θ - ω -scans	19
2.2.2 ω -scans	20
2.2.3 φ -scans	21
2.2.4 Reciprocal Space Maps	21
2.2.5 Technical Aspects	24
2.3 Further Methods	24
2.3.1 Thermal Evaporation	24
2.3.2 Resistivity Measurement	25
2.3.3 Thickness Determination	26
2.3.4 Spectral Transmission	27

2.1 Pulsed Laser Deposition

PLD is a Physical Vapor Deposition (PVD) technique, which essentially utilizes absorption of laser energy by a target and subsequent condensation of evaporated target material on a substrate. Like MBE or CVD, it is used for deposition of thin film materials. Although not true in general [69], a stoichiometric transfer of target composition to the substrate is attributed to PLD. In the following, the PLD setup used for this work (Fig. 2.1a) is described. Furthermore, an overview of the basic physical processes interplaying during a PLD process is given, based on Lorenz (2019) [69].

2.1.1 Setup

The desired thin film material is provided by a ceramic pellet of the respective compound called *target*. It is fabricated by pressing powder with high pressure into cylindrical form, before it is sintered at high temperatures. The crystal growth takes place on a substrate, whose material is chosen to be sapphire (Al_2O_3) of different crystal orientation⁽¹⁾, because it matches the symmetry of the here investigated sesquioxides. They are 500 μm thick with an edge length of 5 mm. In this work, oxygen is chosen as background gas to ensure fabrication of oxide thin film materials. To control the partial pressure of the background gas, the process takes place in a vacuum chamber, called PLD chamber. Inside the chamber, a target holder is placed 90 cm opposite a sample holder, which both are capable of carrying up to four pellets and substrates, respectively. The latter is equipped with a resistive heater, allowing growth temperatures above 700 °C. To ensure homogenous ablation and deposition, both target and substrate can be rotated, whereby a frequency of 120 min^{-1} and 8 min^{-1} is chosen, respectively. Furthermore, an offset ε between the rotation centers of target and substrate is applied, i.e. the plasma plume does not hit the center of the substrate. To achieve homogeneous thickness distributions of the deposited material, $\varepsilon = 7.5 \text{ mm}$ is chosen. Outside the PLD chamber, a KrF excimer laser produces pulsed radiation, which is redirected by a mirror and enters the chamber through a fused silica window. With a wavelength of 248 nm, a UV lens is needed to project the beam on the target surface, where the laser energy is absorbed. By repositioning the lens, the laser spot size can be controlled. The energy per pulse can be adjusted and is several hundred mJ with a duration of about 20 ns, resulting in thousands of kW cm^{-2} on the target surface [69].

The laser energy density, called fluence F , can be calculated by taking the energy per pulse E and the lens position L into account. For an applied $E = 650 \text{ mJ}$, 75 % of the energy are absorbed by mirror, lens and entrance window⁽²⁾. This transmittance is assumed to be independent of E . The resulting fluence dependence $F(E, L) = \frac{0.25E}{A(L)}$ is visualized in Fig. 2.2, whereby the laser spot size A was measured for some L and fitted by assuming parabolic behavior.

2.1.2 Plasma Dynamics

The PLD procedure can be broken down into three physical processes: (i) energy absorption on the target surface, (ii) formation of a plasma and (iii) condensation on the substrate:

- (i) After being projected on the surface of the pellet, the radiation penetrates the material only by a fraction of a μm . Electrons are excited and oscillate in the electromagnetic field of the laser pulse. Those electrons collide with bulk atoms of the surface region, which are subsequently heated up and vaporize. This process is supported by breaking of chemical bonds due to laser radiation.
- (ii) A material cloud expands perpendicular to the target surface due to Coulomb repulsion and recoil. Absorption of remaining laser radiation results in a plasma plume which is strongly forward directed for low background pressures below

⁽¹⁾ c -, r -, m - and a -plane.

⁽²⁾ This was estimated using an energy monitor device and conducted by M. Sc. J. Bredow.

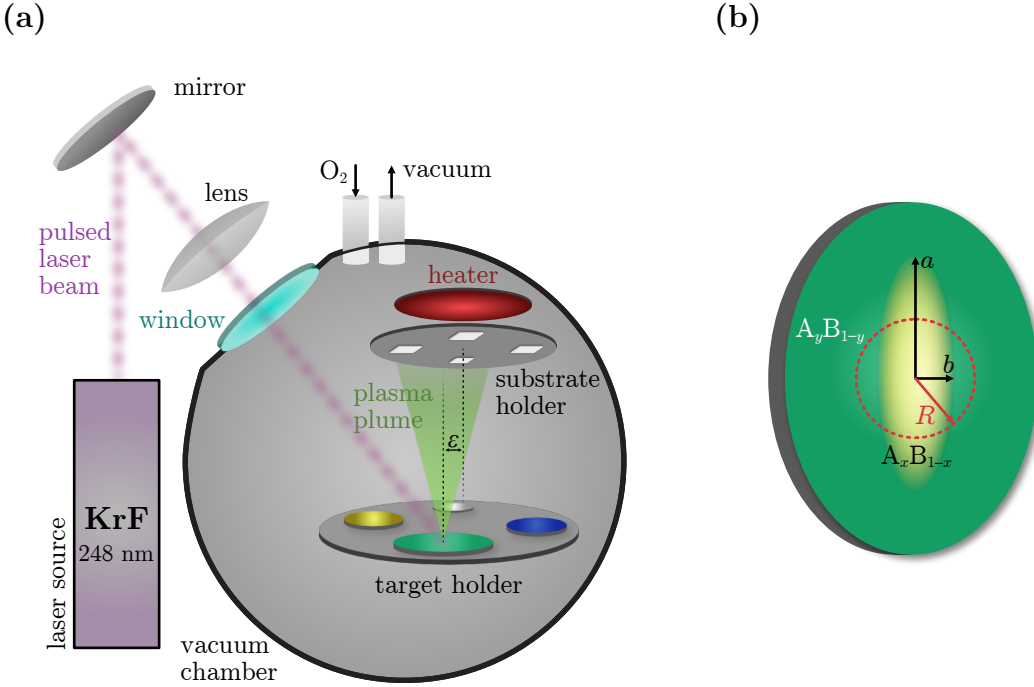


Figure 2.1: (a) Schematic of a PLD setup as described in 2.1.1 (b) Schematic of an elliptically segmented pellet used as target for DCS-PLD (cf. 2.1.3). a and b are semi-major and semi-minor axis of the ellipse, respectively. R denotes the radius of the circular laser spot path on the target surface. The composition of the inner and outer segment is $A_x B_{1-x}$ and $A_y B_{1-y}$, respectively.

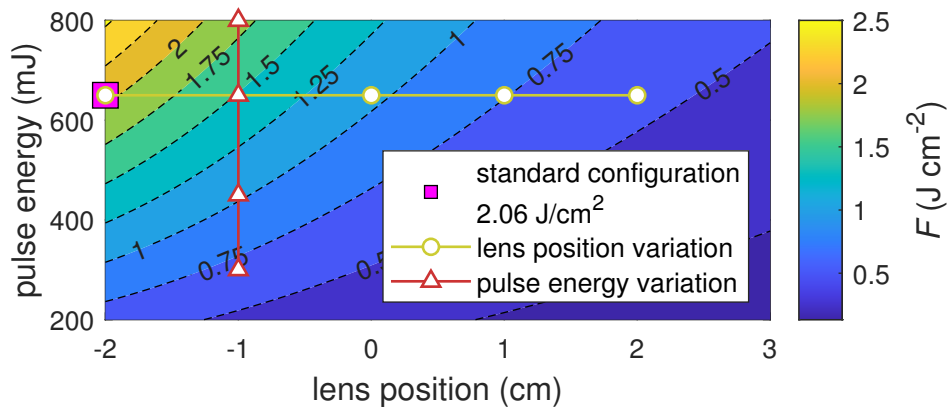


Figure 2.2: Laser energy density depending on the applied pulse energy and lens position. Smaller lens positions yield smaller spot sizes. A value of -2 cm corresponds to the lens being as close as possible to the laser entrance window in the setup used for this work. The default configuration of 650 mJ and -2 cm yields typical fluences of about 2 J cm^{-2} . The triangles and circles represent the variation of laser fluence in this work, achieved by varying the pulse energy and lens position, respectively.

10^{-4} mbar. The target is rotating and laterally moving during this process to minimize the deflection of the plasma due to target degradation. The kinetic energy of the material in the plasma plume is crucial for the deposition process and can be controlled by background partial pressure and laser energy density on the target.

- (iii) The plasma plume hits the substrate which can result in resputtering of already deposited material, which condenses together with the plasma, resulting in thermal equilibrium and thus thin film nucleation. A large number of adatoms results in many nucleation centers which are responsible for smooth films.

It becomes clear, that PLD is a non-equilibrium process, making empirical optimization of growth parameters an essential part of thin film manufacturing [69].

2.1.3 Segmented Target Approach

To provide a discrete material library – a set of different samples with homogeneous composition each –, a segmented target approach as described in Wenckstern *et al.* (2020) [70] is applied. Specifically, the Discrete Combinatorial Synthesis (DCS) method utilizes a radially segmented target, i.e. a target with distinct regions of different material composition. By varying the laser spot position on the target, different plasma compositions can be achieved. Because the target is rotating during PLD, the material distribution must be in such a way that when the radial position R of the laser on the target changes, the average ablated composition $\chi(R)$ changes. This can be realized with an elliptical segmentation, i.e. a target pellet with overall composition A_yB_{1-y} , but containing an inner ellipse with composition A_xB_{1-x} (Fig. 2.1b). By this means, any homogeneous composition $A_\chi B_{1-\chi}$ with χ between x and y can be realized with only one target. χ is related to the path lengths of the moving laser spot on the inner and outer segment, respectively. The composition in the plasma can be calculated via [70]:

$$\chi(R) = y - (y - x) \frac{2}{\pi} \arccos \left[\frac{1}{\delta} \sqrt{1 - \left(\frac{b}{R} \right)^2} \right] \quad (2.1)$$

where δ and b are eccentricity and semi-minor axis of the ellipse, respectively⁽³⁾. Small and large R will result in a composition equal to the composition of the inner and outer segment, respectively. To model the process more accurately one has to take into account that the laser illuminates an area rather than a point-like spot. This is done in 3.2, in particular refer to Fig. 3.11.

2.2 X-Ray Diffraction Measurement

As described in 1.2.2, constructive interference of incoming and scattered X-rays may give insight in the symmetry of exposed crystal structures. This can be utilized for thin film investigation and is called XRD. The XRD device used for this work, namely an

⁽³⁾ The eccentricity is defined as $\delta = \sqrt{1 - b^2/a^2}$, where a is the length of the semi-major axis.

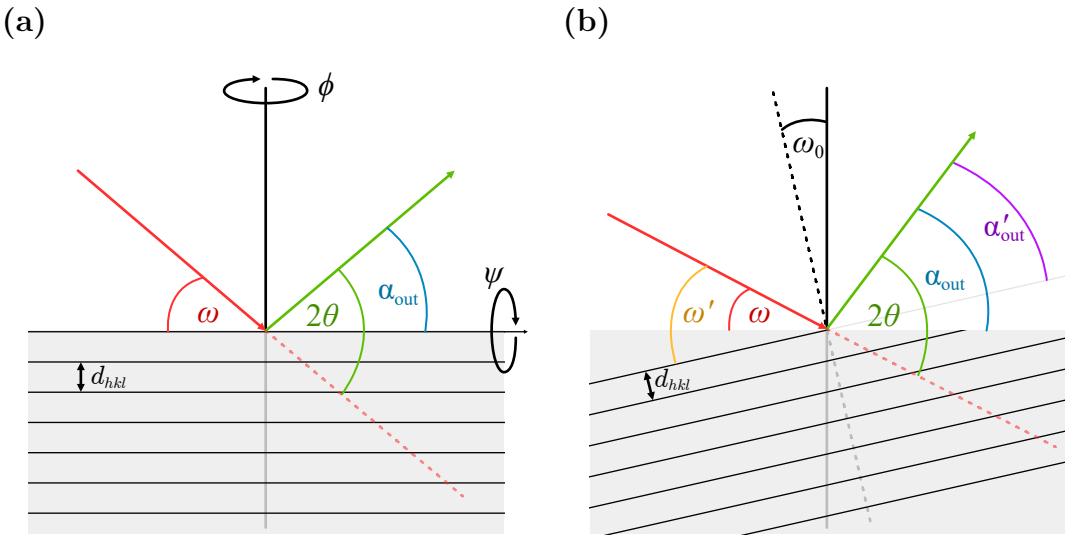


Figure 2.3: (a) Geometry for a 2θ - ω -scan without offset. (b) Scattering geometry containing an offset ω_0 . Angle of incidence and angle of diffraction decrease and increase, respectively. Note that 2θ is not affected by this offset.

X’Pert Pro (Malvern Panalytical Ltd.), as well as the applied scanning techniques will be presented in the following.

A sample with surface normal parallel to the z -axis of the laboratory system is exposed with X-rays at an angle ω between sample surface and incident radiation. The diffracted radiation is measured at an angle α_{out} between sample surface and detector. 2θ is used to describe the angle between outgoing beam and the extension of the incoming beam, which both span the scattering plane. It follows that $2\theta = \omega + \alpha_{\text{out}}$. Note that θ in Equ. (1.10) is the same angle as half of 2θ . The scattering plane is depicted in Fig. 2.3a. The sample can be rotated by ϕ (“azimuth”) and ψ around an axis parallel to the surface normal and parallel to the intersection of sample surface and scattering plane, respectively.

2.2.1 2θ - ω -scans

When probing for lattice plane distances using the BRAGG condition in its simplest form, it is assumed that the scattering planes are parallel to the sample surface (cf. Fig. 2.3a). It is necessary that $\omega = \alpha_{\text{out}}$ which implies $2\theta = 2\omega$. So the angle of incidence ω is coupled to 2θ which represents the distance between lattice planes (cf. Equ. (1.10)). Measuring the diffracted X-ray intensity while varying 2θ and maintaining the condition $2\theta = 2\omega$, is called a 2θ - ω -scan. This results in a 2θ - ω diffraction pattern, where peaks correspond to constructive interference and thus to certain lattice plane distances.

When analyzing 2θ - ω diffraction patterns, one usually compares to predicted peak positions of the expected phase of the compound which is investigated. This reference diffraction pattern stems from powder samples of the respective compound, containing all crystal orientations during one 2θ - ω -scan. When a peak is identified, a possible peak shift is determined and the shape of the peak is investigated. Peak shifts may be due

to residual stress, substrate induced strain or compositional gradients in the thin film [58]. A minimum amount of peak broadening is always present due to convergence of the incident beam as well as convolution of $K\alpha_1$ - and $K\alpha_2$ -radiation (cf. 1.2.2), which is called instrumental broadening [58]. The Full Width at Half Maximum (FWHM) of the highly crystalline substrate peaks may give a reference for broadening of peaks in 2θ - ω diffraction data.

This method can be extended to measure lattice planes which are not parallel to the sample surface but tilted by ω_0 . This is done by rotating the reference frame of the sample in such a way that the BRAGG condition is fulfilled again. Note that 2θ does not change upon rotation, as can be seen in Fig. 2.3b. When probing for plane distances of the rotated lattice, one finds for the coupling between 2θ and ω :

$$\begin{aligned}\omega' &= \alpha'_{\text{out}} \\ \omega + \omega_0 &= \alpha_{\text{out}} - \omega_0 \\ \omega + \omega_0 &= (2\theta - \omega) - \omega_0 \\ \Rightarrow 2\theta &= 2(\omega + \omega_0) = 2\omega'.\end{aligned}$$

This coupling is equivalent to a 2θ - ω -scan but with an offset ω_0 applied to the angle of incidence. There are several use cases for applying an offset ω_0 :

- (i) It is assumed that ω denotes the angle between incident X-ray beam and the sample surface. But a perfect alignment between sample and sample holder is not always possible. So to correct this tilt between expected sample position and its real inclination, the offset ω_0 can be set to really probe for lattice planes parallel to the sample surface. This is done before measuring a 2θ - ω -scan to achieve preciser results.
- (ii) When probing for lattice planes which are not parallel to the sample surface (“asymmetric reflections”), one can apply the expected inclination angle as an offset ω_0 . This is the case in Fig. 2.3b.
- (iii) When 2θ is fixed, but ω_0 is varied, an ω -*scan* is performed, which enables quantification of mosaicity (cf. 2.2.2).

2.2.2 ω -scans

Thin films may exhibit a distribution of lattice plane inclination, called mosaicity. This results in an observation of diffraction peaks for several offsets ω_0 . The mosaicity can thus be quantified by fixing 2θ , representing a certain lattice plane distance, and then vary ω_0 and measure the X-ray intensity. This is called an ω -*scan*, and the FWHM of the observed diffraction pattern (also called *Rocking curve*) is a measure for the mosaicity [58]. ω -scans are particularly useful when comparing a set of thin films of varying deposition parameters to optimise growth conditions. In particular, recording Rocking curves of symmetric and asymmetric lattice planes allows the calculation of dislocation densities in the thin film [71].

2.2.3 φ -scans

A 2θ - ω -scan is not capable of resolving in-plane rotations of crystal domains, because the distance of lattice planes parallel to the surface are not affected. Those rotational domains can be detected by probing for lattice planes which are inclined with respect to the surface, i.e. by fixing 2θ to the expected lattice plane distance and ω_0 to the inclination angle (cf. Fig. 2.3b). Depending on the symmetry of the inspected material, constructive interference should only appear for distinct values of ϕ . So by rotating the sample by 360° and simultaneously recording the X-ray intensity, a φ -scan (also called *Azimuth-scan*) can yield information about the existence of rotational domains. If the number of observed peaks in the φ -scan diffraction pattern exceeds the theoretically expected number for a single crystal, rotational domains are present [58]. Furthermore, comparing the φ -scan diffraction data of thin film and substrate reveals whether the film has grown with an in-plane rotation with respect to the substrate. Finally, if the thin film grows in a tilted manner on the substrate, a φ -scan prior to an ω -scan can ensure the correct positioning before alignment. Then, the BRAGG condition is fulfilled for performing a 2θ - ω -scan.

2.2.4 Reciprocal Space Maps

Because the BRAGG condition is equal to the description of diffraction with $\mathbf{k}' - \mathbf{k}$ and reciprocal space vectors \mathbf{K}_{hkl} (cf. 1.2.2), both can be used depending on context. Henceforth, $\mathbf{k}' - \mathbf{k}$ will be denoted by the *scattering vector* \mathbf{q} . Note that \mathbf{k} and \mathbf{k}' are parallel to incoming and outgoing beam, respectively. From the definition of angles, it follows that

$$\mathbf{q} = \begin{pmatrix} q_{\parallel} \\ q_{\perp} \end{pmatrix} = \mathbf{k}' - \mathbf{k} \quad (2.2)$$

$$= \frac{1}{\lambda} \begin{pmatrix} \cos \alpha_{\text{out}} \\ \sin \alpha_{\text{out}} \end{pmatrix} - \frac{1}{\lambda} \begin{pmatrix} \cos \omega \\ -\sin \omega \end{pmatrix} \quad (2.3)$$

$$= \frac{1}{\lambda} \begin{pmatrix} \cos(2\theta - \omega) - \cos(\omega) \\ \sin(2\theta - \omega) + \sin(\omega) \end{pmatrix}. \quad (2.4)$$

From Equ. (2.4), two properties follow for the scattering vector:

$$-q_{\parallel}/q_{\perp} = -\tan \left(\omega - \frac{2\theta}{2} \right) = \tan \omega_0, \quad (2.5)$$

$$|\mathbf{q}| = \sqrt{q_{\parallel}^2 + q_{\perp}^2} = \frac{1}{\lambda} 2 \sin \theta \stackrel{\text{Bragg}}{=} \frac{1}{d_{hkl}}, \quad (2.6)$$

where the last equality of Equ. (2.6) holds, if \mathbf{q} is a reciprocal lattice vector \mathbf{K}_{hkl} . The scattering vector, together with the corresponding XRD geometry is depicted in Fig. 2.4a. Because 2θ and ω can simultaneously be represented by \mathbf{q} , it is possible to measure intensities for several \mathbf{q} , such that a part of the reciprocal space $Q \ni \mathbf{q}$ is mapped. Consequently, this is called a Reciprocal Space Map (RSM). According to Equ. (1.9), a peak in 2D reciprocal space Q should be observed if \mathbf{q} is a reciprocal space vector. In this case, $\mathbf{q} = \mathbf{K}_{hkl}$ is called a *reflection*. With Equ. (2.5) one can determine

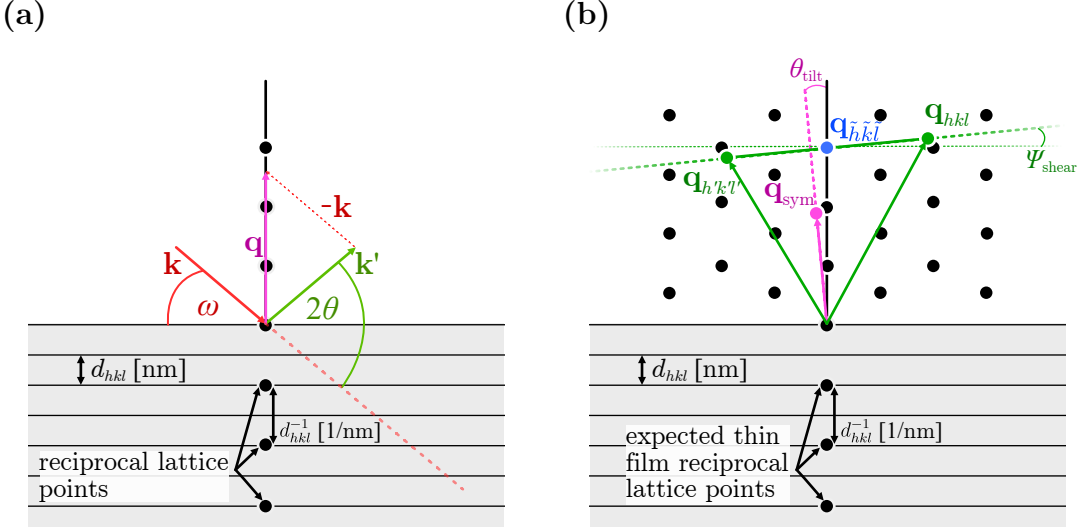


Figure 2.4: (a) Construction of the scattering vector (magenta) from incoming (red) and outgoing (green) beam, according to Equ. (2.4). The reciprocal lattice points are visualized together with the lattice planes. It has to be noted that the distances between lattice planes and between reciprocal lattice points have different dimensions. (b) Expected reciprocal lattice (black circles) and different deviations due to lattice distortions: Thin film tilt can be determined from symmetric reflections (magenta). However, shear angles do not manifest in symmetric reflections (blue), but in asymmetric reflections (green).

ω_0 – the direction of the corresponding lattice planes⁽⁴⁾, and with Equ. (2.6) the lattice plane distance d_{hkl} can be calculated. Note that for rhombohedral crystals, d_{hkl} can also be predicted from the lattice constants a and c with the following equation [61]:

$$d_{hkl} = \left(\frac{4}{3} \frac{h^2 + k^2 + hk}{a^2} + \frac{l^2}{c^2} \right)^{-1/2}. \quad (2.7)$$

The inclination with respect to the c -axis can be determined via [67]

$$\alpha_{hkl|c} \arccos \left(\frac{l}{\sqrt{\frac{4c^2}{3} \frac{h^2+k^2+hk}{a^2} + l^2}} \right). \quad (2.8)$$

A 2θ - ω -scan corresponds to a set of \mathbf{q} with fixed direction in reciprocal space, but varying length. For scanning symmetric reflections, \mathbf{q} is parallel to the surface normal (as in Fig. 2.4a). On the other hand, an ω -scan corresponds to a set \mathbf{q} with fixed length but varying direction. The mosaicity can therefore approximately quantified by the broadening of a reflection perpendicular to the direction of \mathbf{K}_{hkl} . Because anisotropic strain has an effect on direction and length of inclined lattice planes, asymmetric reflections, i.e. $\omega_0 \neq 0$, can be deconvoluted into an in-plane and out-of-plane component. By this means, RSMs enable the calculation of lattice constants. To precisely calculate the latter, several corrections are applied to the recorded RSMs, as proposed in Kneiß *et al.* (2021) [64]:

⁽⁴⁾ Note that the “ $-$ ” in $-q_{||}/q_{\perp}$ is necessary, such that this fraction is the tangens the angle between \mathbf{q} and surface normal with correct sense of rotation.

- High-quality sapphire substrates are used for deposition of thin films. It can be assumed that they have the expected crystal structure of bulk $\alpha\text{-Al}_2\text{O}_3$ (cf. Tab. 1.1). So any deviation of the observed reflection $\mathbf{q}_{hkl}^{\text{Al}_2\text{O}_3,\text{obs}}$ from the expected peak position $\mathbf{q}_{hkl}^{\text{Al}_2\text{O}_3,\text{lit}}$ is corrected by a rotation \mathbf{R} and scaling ρ of reciprocal space Q :

$$\mathbf{q}^{\text{cor}} = \rho \mathbf{R} \cdot \mathbf{q}^{\text{obs}} \quad , \quad \mathbf{q}^{\text{obs}} \in Q , \quad (2.9)$$

with

$$\mathbf{R} = \begin{pmatrix} \cos \gamma & -\sin \gamma \\ \sin \gamma & \cos \gamma \end{pmatrix} \quad , \quad \gamma = \arccos \left(\frac{\mathbf{q}_{hkl}^{\text{Al}_2\text{O}_3,\text{lit}} \cdot \mathbf{q}_{hkl}^{\text{Al}_2\text{O}_3,\text{obs}}}{|\mathbf{q}_{hkl}^{\text{Al}_2\text{O}_3,\text{lit}}| \cdot |\mathbf{q}_{hkl}^{\text{Al}_2\text{O}_3,\text{obs}}|} \right) \quad (2.10)$$

$$\rho = \frac{|\mathbf{q}_{hkl}^{\text{Al}_2\text{O}_3,\text{lit}}|}{|\mathbf{q}_{hkl}^{\text{Al}_2\text{O}_3,\text{obs}}|} . \quad (2.11)$$

- If the thin film grows tilted (e.g. due to slip systems, cf. 1.3.2), a symmetric reflection – having scattering vector parallel to the surface normal in theory – will exhibit an in-plane component $q_{\parallel,hkl}^{\text{film}} \neq 0$. The tilt angle can be calculated by Equ. (2.5):

$$\theta_{\text{tilt}} = \arctan \left(-\frac{q_{\parallel,hkl}^{\text{film}}}{q_{\perp,hkl}^{\text{film}}} \right) . \quad (2.12)$$

To determine the lattice constants from asymmetric peaks, the reciprocal space is again rotated as in 2.10 but with rotation angle $-\theta_{\text{tilt}}$. This scenario is depicted in Fig. 2.4b, where the magenta colored reflection deviates from the expected symmetric position.

- If the thin film is sheared, a symmetric reflection $\mathbf{q}_{\tilde{h}\tilde{k}\tilde{l}}^{\text{film}}$ will be unaffected. On the contrary, an asymmetric reflection with both in- and out-of-plane component is affected. To get reliable results for the lattice constants, this shear angle Ψ_{shear} has also to be corrected, and can be calculated from two inclined lattice planes (hkl) and ($h'k'l'$), i.e. scattering vectors with non-zero in-plane component. Those vectors must have symmetry of a mirror plane perpendicular to the scattering plane⁽⁵⁾. The geometry is depicted in Fig. 2.4b, with the blue and green reflections representing the symmetric and asymmetric reflections, respectively. The shear angle can be calculated with

$$\Psi_{\text{shear}} = \arctan \left(\frac{q_{\perp,hkl}^{\text{film}} - q_{\perp,h'k'l'}^{\text{film}}}{q_{\parallel,hkl}^{\text{film}} - q_{\parallel,h'k'l'}^{\text{film}}} \right) . \quad (2.13)$$

To correct the shear, a rotation around the corresponding symmetric reciprocal lattice point $\mathbf{q}_{\tilde{h}\tilde{k}\tilde{l}}^{\text{film}}$ with the same expected out-of-plane component must be applied.

⁽⁵⁾ This can be achieved by probing for a plane (hkl) and then rotate the sample around ϕ by 180° .

Table 2.1: Configurations for the applied XRD scans.

scan type	detector mode	step size ($^{\circ}$)	active channels	effective width
2 θ - ω -scan	1D Scanning Line	0.005	255	2.51 $^{\circ}$
ω -scan	0D Receiving Slit	0.005	55	3.025 mm
ω -optimization	0D Receiving Slit	0.02	37	2.035 mm
φ -scan	0D Receiving Slit	0.05	55	3.025 mm
φ -optimization	0D Receiving Slit	0.5	55	3.025 mm
RSMs	1D Frame Based	0.005	255	2.51 $^{\circ}$

2.2.5 Technical Aspects

The radiation is produced by a copper anode, resulting in a wavelength of $\lambda = 1.5406 \text{ \AA}$ for Cu-K α_1 radiation. Note that Cu-K α_2 and Cu-K β radiation is not filtered out, resulting in additional low-intensity peaks in the diffractograms. Furthermore, contamination of the anode with tungsten results in an observable W-L α_1 contribution with energy between Cu-K α - and Cu-K β -radiation. During the course of the conducted experiments, the contaminated anode has been replaced, so the peaks corresponding to W-L α_1 -radiation are not present in every diffractogram.

The diffracted radiation is detected with a *PIXcel^{3D}* (*Malvern Panalytical Ltd.*) detector. For 2 θ - ω -scans (cf. 2.2.1), the detector is operating in **Scanning Line** mode. For scans fixing the 2 θ position, i.e. ω - (cf. 2.2.2) and φ -scans (cf. 2.2.3), the detector is operated in **Receiving Slit** mode. RSMs are recorded with the **Frame Based** mode. The settings for the various scans are listed in Tab. 2.1. Note that it is distinguished between scans and optimizations. The latter were applied for aligning the sample correctly, depending on the measurement. For example, before a 2 θ - ω -scan of *m*-plane oriented rhombohedral samples, a φ -scan has been applied for the inclined (30.6) reflection to find the correct azimuth of the *c*-axis, which is called φ -optimization. Afterwards, a Rocking curve has been recorded and ω set to the maximum of the peak to compensate for the expected lattice tilt (cf. 1.3.2), called an ω -optimization.

2.3 Further Methods

2.3.1 Thermal Evaporation

The ohmic contacts for electrical characterization of Cr₂O₃ thin films were deposited by means of thermal evaporation. This method was already utilized for successfully contacting α -Ga₂O₃ thin films [50], thus also applied for similarly structured Cr₂O₃ thin films. This PVD method utilizes a *boat* made of a material with high melting temperature (tungsten W or molybdenum Mo) that is loaded with the target material in form of powder or filament. A vacuum chamber is used to achieve pressures of around $5 \times 10^{-5} \text{ mbar}$. A high current is driven through the contacted boat, such that resistive heating ensures melting of the target material and subsequent evaporation. The evaporated material spreads out due to the pressure gradient and condensates on the sample which is mounted to a rotating holder. A metal mask ensures that only the

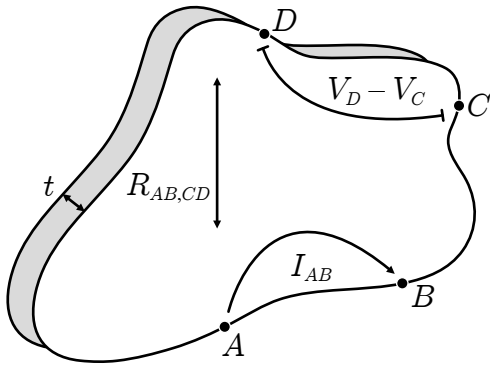


Figure 2.5: The geometry for measuring the specific resistance of a thin film, proposed by Pauw (1958) [72].

corners of the sample are contacted.

The contacts are either a stacking of titanium, aluminum, and gold (henceforth referred to as *Ti-Al-Au*) or only titanium and gold (*Ti-Au*). The thickness of each material layer is around 30 nm, measured with a crystal oscillator during the process. The currents used for evaporating Ti, Al and Au are 60 A, 50 A and 45 A, respectively.

2.3.2 Resistivity Measurement

As shown by Pauw (1958) [72], it is possible to determine the specific resistivity of a flat sample by only making four small contacts at arbitrary points at its edge and measure the thickness t as well as the following resistances⁽⁶⁾:

$$R_{AB,CD} = \frac{V_D - V_C}{I_{AB}} \quad , \quad R_{BC,DA} = \frac{V_A - V_D}{I_{BC}}, \quad (2.14)$$

where $V_D - V_C$ is the potential difference between points C and D , measured while applying I_{AB} , the current entering the sample at point A and leaving it at point B . The geometry⁽⁷⁾ is depicted in Fig. 2.5a. The specific resistivity ρ can then be calculated via

$$\rho = \frac{\pi t}{\ln 2} \frac{R_{AB,CD} + R_{BC,DA}}{2} \cdot f \left(\frac{R_{AB,CD}}{R_{BC,DA}} \right), \quad (2.15)$$

where f is a function equal to 1, if the two measured resistances are equal; f decreases for higher ratios of the two measured resistances [72]. The geometry can further be used to determine the Hall mobility μ_H and carrier concentration n , but due to low

⁽⁶⁾ The unit of those quantities is Ω , thus the name.

⁽⁷⁾ Note that Equ. (2.15) is restricted to these conditions: “(a) The contacts are at the circumference of the sample. (b) The contacts are sufficiently small. (c) The sample is homogeneous in thickness. (d) The surface of the sample is singly connected, i.e., the sample does not have isolated holes.” (Pauw (1958) [72])

conductivities of the here investigated Cr_2O_3 thin films, this method yields no reliable information about μ_H and n .

Temperature-dependent resistivity measurements are conducted with a Hall probe station *CRX-VF* controlled by the measurement setup *HM-8425* (Lake Shore Cryotronics, Inc.), cooled via a *Model 336 cryogenic temperature controller* (Lake Shore). The samples are measured in a vacuum and the temperature can be controlled between 10 K and 390 K.

2.3.3 Thickness Determination

The optical constants and thickness t of a thin film can be measured by the change of polarization state upon light reflection. If the probing light covers several wavelengths at once, one refers to spectroscopic ellipsometry, which will be presented in the following, based on Fujiwara (2007) [73]. The incoming light can be represented by an electromagnetic wave, decomposed into two components being parallel (p) and perpendicular (s) to the scattering plane:

$$\mathcal{E} = \mathcal{E}_{\text{ip}} + \mathcal{E}_{\text{is}}. \quad (2.16)$$

In general, the amplitudes of p- and s-polarized light change in a different manner after reflection, so the overall polarization of the reflected light is changed. This change is described by the fraction

$$\rho = \frac{r_p}{r_s} := \tan \Psi \cdot \exp(i\Delta), \quad (2.17)$$

where r_p and r_s are the amplitude reflection coefficients⁽⁸⁾ for the p- and s-polarized component, respectively. For simple structures, Ψ is essentially the refractive index n , and Δ represents the extinction coefficient k . In general, they can be calculated from the JONES-matrix – representing the reflection – and depend on the angle of incidence as well as the photon energy.

To determine the sample thickness, the spectra of Ψ and Δ can be generated using a model for the sample structure, which is then fitted to the experimental data. In this work, this model consists of an Al_2O_3 substrate without backscattering from the backside (infinite thickness); a Cr_2O_3 thin film of thickness t ; and a mixed layer of air and Cr_2O_3 , approximating the roughness of the sample. Because the measured spectra were confined to the visible regime of the thin film (approx. < 2.8 eV), one can apply the CAUCHY model [73], approximating the refractive index by

$$n(\lambda) = A + \frac{B}{\lambda^2} + \frac{C}{\lambda^4} + \mathcal{O}(\lambda^{-6}) \quad , \quad k = 0. \quad (2.18)$$

The spectroscopic ellipsometry measurements are done with an *M-2000VI* (J.A. Woolam Co., Inc.) and the data is analyzed using the software *WVASE* (J.A. Woolam). The angles of incidence are chosen to be 50°, 60° and 70°, and the modelled spectral range is 0.75 to 2.8 eV. If samples of different orientation were fabricated in the same process, one can assume similar thicknesses, and a measurement with three angles was conducted only for one sample of the batch. The other samples were measured with

⁽⁸⁾ They are defined by the amplitude of incoming (i) and reflected (r) radiation: $r = |\mathcal{E}_r|/|\mathcal{E}_i|$.

only one angle, if the determined thickness did not differ significantly from the more accurately measured one.

Note that the investigated thin films are not isotropic in general, which is why the validity of the determined thickness is checked by profilometer measurements with a *Dektak XT Stylus Profiler* (Bruker Corporation). The edges of the quadratic substrates are masked by the sample holder during deposition, which is why they are not deposited with the target material. Consequently, measuring the height profile ranging from an edge to coated regions of the sample yields an approximation for t by the height of the observed step edge.

2.3.4 Spectral Transmission

For optical characterization, spectral transmission measurements were conducted: Monochromatic light is used to compare a reference beam with the intensity of radiation transmitting a sample of thickness t . The fraction of both is defined as the transmittance $T(E)$ which depends on the photon energy $E = \hbar\omega$. In a simple model, neglecting reflection on the sample surface as well as thin film interference [74], the absorption coefficient α can be defined via the LAMBERT-BEER-law:

$$T \propto e^{-\alpha t}, \quad (2.19)$$

which states an exponential decay of intensity with increasing thickness t . The absorption coefficient is based on the transition rate between valence band and conduction band at photon energy E . This rate depends on the energy-dependent coupling matrix element for this transition, as well as the joint electron and hole density of states (DOS) [75]. If matrix element and DOS are assumed to be constant and parabolic, respectively [76], then $\alpha = 0$ for energies below the band gap, and for direct transitions it follows [75]:

$$\alpha \propto (E - E_g)^{1/2}. \quad (2.20)$$

This allows extrapolating an α^2 vs. E plot to the abscissa to determine the band gap E_g . For indirect transitions, phonons with energy $\hbar\Omega$ must be considered which leads to

$$\alpha \propto (E + \hbar\Omega - E_g)^2, \quad (2.21)$$

which itself allows the determination of the band gap by extrapolating an $\alpha^{1/2}$ vs. E plot, if the phonon energy is neglected [75]. According to Zanatta (2019) [75], these two methods are often mislabeled as TAUC plots α^η vs. E with exponent η defining the direct or indirect nature of the transition. Actually, those methods are based on the description of *crystalline* solids, whereas the original “TAUC plot” was an empirical description of *amorphous* germanium, leading to an $(\alpha E)^{1/2}$ vs. E plot [76]. This method has been applied [13, 20, 30, 36], to determine the band gap of crystalline solids, which is an inappropriate use of the TAUC method, which can be only applied if localized energy states are present, as in amorphous solids or nanoparticles [77]. In this work, a direct band gap of Cr_2O_3 is assumed and therefore the α^2 vs. E plot is utilized. This is described in more detail in 3.1.

In general, it has to be noted that the value obtained from extrapolating any of those plots to the abscissa is affected by several approximations: no COULOMB interaction between holes and electrons is considered; defect states that could enable absorption

below E_g are neglected; the parabolic nature of the DOS is only true for $k \approx 0$ and not for large energies $\hbar\omega \gg E_g$; differences in selecting the regime that is selected for fitting may result in substantial deviations for the values of E_g [75]. Due to those considerations, the value extrapolated from α^2 vs. E plots will be called optical gap E_{opt} . Due to the fact that the intersection of

$$\alpha = \text{const.} \cdot (E - E_{\text{opt}})^{1/2}$$

with the abscissa does not depend on the value of const., the α^2 vs. E plots are visualized with arbitrary units on the ordinate (cf. Fig. 3.5b or Fig. 3.32).

The measurements were conducted in a spectral range of 200 to 2800 nm, realized by two light sources with a *Lambda 40* (Perkin-Elmer). The spectra are corrected with a corresponding reference substrate. The measurements were done by M. Hahn.

Chapter 3

Experiment, Results and Discussion

Contents

3.1	Preliminary Investigations	29
3.1.1	Experiment	30
3.1.2	Results	30
3.1.3	Conclusion	38
3.2	Doping of Cr₂O₃ Thin Films	40
3.2.1	Experiment	40
3.2.2	Results	41
3.2.3	Conclusion	48
3.3	Strain Analysis	50
3.3.1	Experiment	50
3.3.2	Results	53
3.3.3	Conclusion	66
3.4	Cr₂O₃ Buffer Layers for α-Ga₂O₃	68
3.4.1	Experiment	68
3.4.2	Results	69
3.4.3	Conclusion	73

3.1 Preliminary Investigations

In the following, the feasibility of depositing Cr₂O₃ thin films via PLD as well as their resulting properties are investigated. Since α -Cr₂O₃ is the only phase of chromia (cf. 1.1.1), it is expected that the growth results in either rhombohedral or amorphous films. Furthermore, if a crystalline phase is present, the orientation with respect to the sapphire substrates is of interest. Because Al₂O₃ and Cr₂O₃ exhibit the same crystal symmetry, it is expected that the crystal orientation of the film matches the corresponding substrate orientation. Finally, deposition parameters should be optimized to obtain the best crystal quality.

3.1.1 Experiment

Due to the similar crystal structure of Cr_2O_3 and $\alpha\text{-Ga}_2\text{O}_3$, the deposition parameters of the latter were chosen as a starting point to deposit chromia thin films on $10 \times 10 \text{ mm}^2$ sapphire substrates with *m*-plane orientation. Namely, a pulse energy of 650 mJ and a pulse frequency of 20 Hz were applied for a total of 30 000 pulses. To investigate the influence of deposition parameters, three batches were produced:

1. variation of oxygen partial pressure from 8×10^{-5} to 1×10^{-2} mbar with a fixed temperature of 745°C ,
2. variation of growth temperature from 725 to 765°C with a fixed oxygen partial pressure of 1×10^{-3} mbar, and
3. variation of substrate orientation between *c*- (00.1), *r*- (01.2) *m*- (10.0) and *a*-plane (11.0) $5 \times 5 \text{ mm}^2$ sapphire substrates⁽¹⁾ with a fixed oxygen partial pressure of 1×10^{-3} mbar and a growth temperature of 715°C .

Structural properties of those thin films were determined by $2\theta\text{-}\omega$ -scans, ω -scans and φ -scans. The thickness was determined via spectroscopic ellipsometry, and transmission spectra were recorded for two samples of the 1st batch to determine the optical band gap. Temperature dependent resistivity measurements were performed only for the samples of the 3rd batch, because all *m*-plane oriented samples showed no conductivity at room temperature.

3.1.2 Results

Oxygen Partial Pressure Variation on *m*-plane Sapphire

In the following, the results for the samples produced at four different oxygen partial pressures are analyzed. In Fig. 3.1, the $2\theta\text{-}\omega$ -patterns are depicted. For each pattern, the two peaks (solid line) at around 68° correspond to the (30.0) reflection of the *m*-plane oriented sapphire substrate. The splitting occurs due to the similar wavelength of $\text{Cu-K}\alpha_1$ and $\text{Cu-K}\alpha_2$ radiation. The additional peaks also stem mainly from the (30.0) reflection of Al_2O_3 and are caused by $\text{W-L}\beta_2$ -, $\text{W-L}\beta_1$ -, $\text{Cu-K}\beta$ -, $\text{W-L}\alpha_1$ - and $\text{W-L}\alpha_2$ -radiation (increasing angles).⁽²⁾ In the vicinity of the calculated peak position for the (30.0) reflection of Cr_2O_3 (cf. 1.3), there is a peak observed for each sample, indicating that the α -phase of Cr_2O_3 is present. Note that the peak position is varying depending on the chosen oxygen partial pressure. The difference to the expected peak position $2\theta_0$ is expressed as o.o.p. strain ϵ_{zz} using the Bragg equation Equ. (1.10) and then

$$\epsilon_{zz} = \frac{d - d_0}{d_0} = \left(\frac{1}{\sin(2\theta/2)} - \frac{1}{\sin(2\theta_0/2)} \right) \cdot \sin(2\theta_0/2). \quad (3.1)$$

In Fig. 3.2a, the calculated strain is shown in dependence of the corresponding oxygen partial pressure. The strain decreases from approx. 0.95 % to 0.45 % with increasing

⁽¹⁾ In the following, the BRAVAIS-MILLER-indices will be omitted.

⁽²⁾ **Klar wäre das besser das im plot an die linien zu schreiben, aber das war mir irgendwie zu auffällig es schön zu machen. Gehts auch so?**

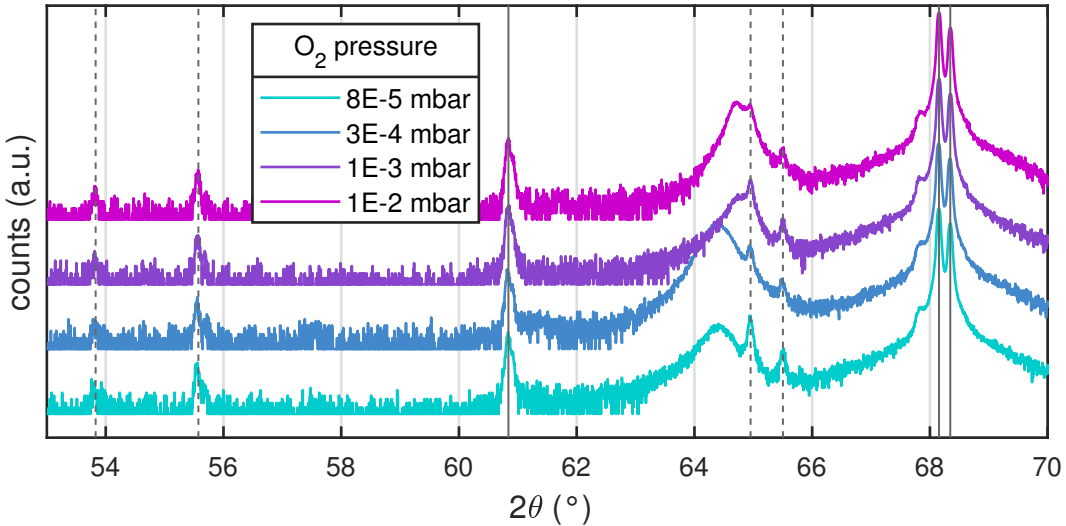


Figure 3.1: 2θ - ω -patterns of Cr_2O_3 thin films deposited on *m*-plane sapphire for various oxygen partial pressures. The solid lines indicate (30.0) substrate reflections corresponding to copper radiation, whereas the dashed lines indicate (30.0) substrate reflections corresponding to tungsten radiation.

pressure. This strain reduction may therefore be the result of increased background gas scattering which results in less kinetic energy of the specimen reaching the heated substrate (cf. 2.1.1).

For each sample, the 2θ angle was fixed to the observed (30.0) reflection of Cr_2O_3 and an ω -scan was performed. The FWHM of the ω -patterns (henceforth “ ω -FWHM”) are depicted in Fig. 3.2b. The values vary between approx. $30'$ and $50'$ and show a dependence on oxygen partial pressure, which is less pronounced compared with o.o.p. strain (Fig. 3.2a). Still, since ω -FWHM is connected to the mosaicity of the thin film, higher oxygen partial pressures yield slightly better crystal qualities. Note that due to the fact that an oxygen partial pressure of 1×10^{-3} mbar yielded the best crystal quality, this value is used for future deposition processes.

To probe for rotational domains of the thin films, φ -scans were performed by fixing 2θ and ω to the corresponding angles of the (30.6) plane of Cr_2O_3 , which has an inclination angle of 32.4° with respect to the (30.0) plane. The diffraction patterns are depicted in Fig. 3.3. The observed peaks of the thin film align with the peaks of the single crystal substrate, indicating that the film has no in-plane rotation with respect to the substrate. Furthermore, the absence of additional peaks indicates that there exists only a single domain of the thin film⁽³⁾.

The growth rate g varies between 3 pm pulse^{-1} and 7 pm pulse^{-1} and is depicted in Fig. 3.4a. No systematic dependence on the oxygen partial pressure can be observed.

The transmission spectra of two selected Cr_2O_3 thin films are shown in Fig. 3.5a. The samples are not fully transparent in the visible spectrum and they exhibit a greenish tint, as can also be seen in Fig. 3.4b. To determine the onset of absorption E_{opt} , an α^2 vs. E plot (Fig. 3.5b) is utilized (cf. 2.3.4). Although the publications used for reference

⁽³⁾ Vielleicht müsste ich noch erwähnen warum die beiden Reflections hier bei $+55^\circ$ und -55° liegen, also 110° auseinander. Aber das versteh ich selber nicht so richtig :(ich würde erwarten dass sie 180° auseinander liegen.

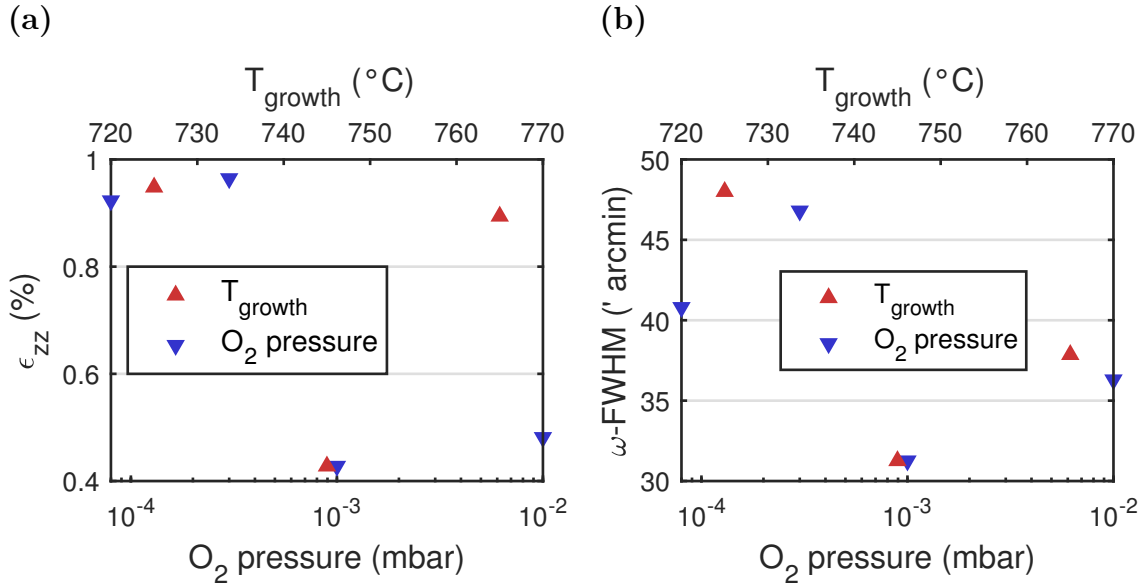


Figure 3.2: (a) o.o.p. strain calculated with Equ. (3.1) and (b) ω -FWHMs for samples from growth temperature series (red triangles, top x -axis) and oxygen partial pressure series (blue triangles, bottom x -axis).

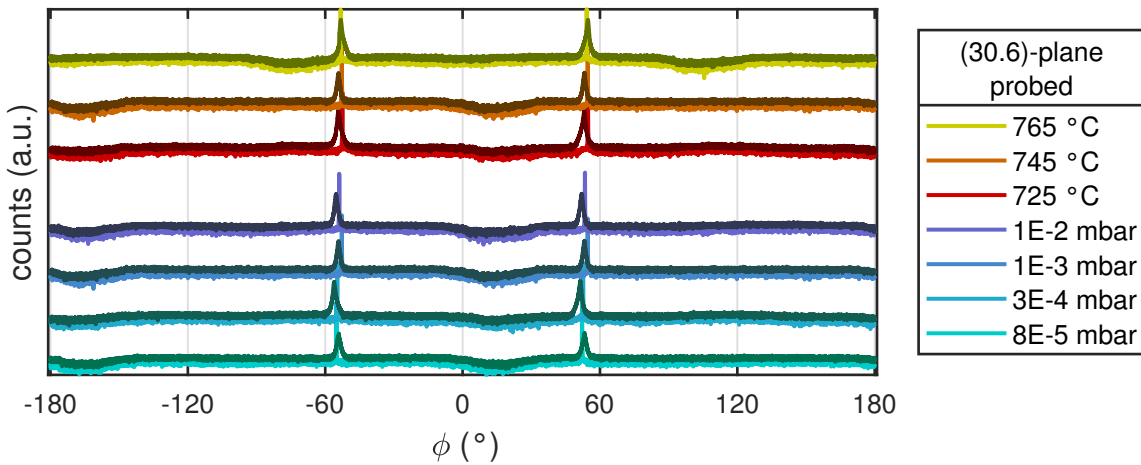


Figure 3.3: Diffraction patterns of ϕ -scans performed on the inclined (30.6) reflections for m -plane Cr₂O₃ (darker color) and Al₂O₃ (brighter color). The diffraction patterns cover the samples from variation of oxygen partial pressure (teal to blue colored) and variation of growth temperature (red to yellow colored).

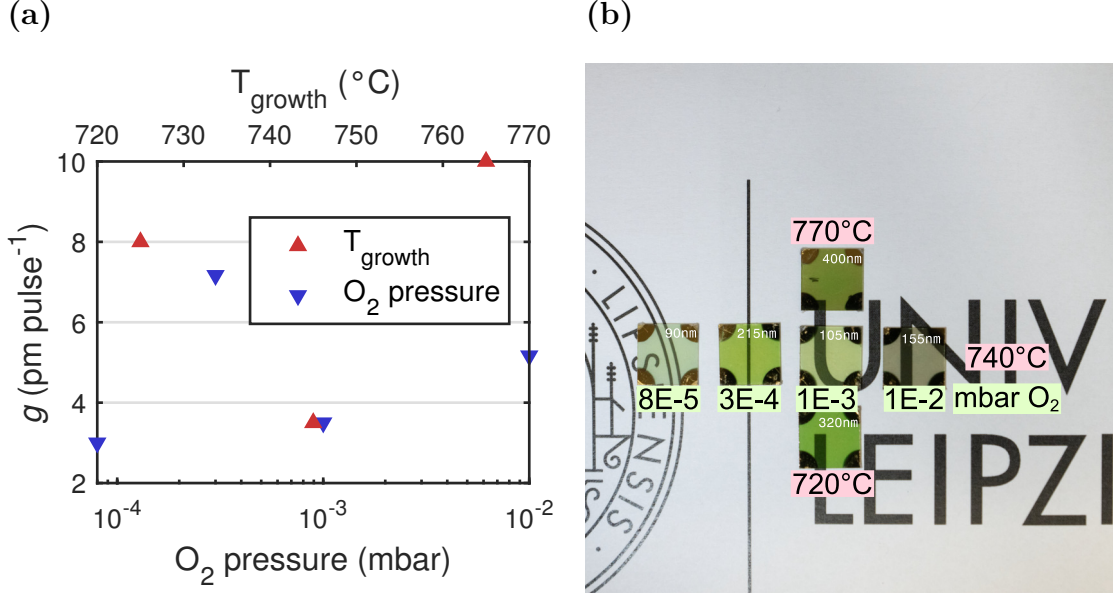


Figure 3.4: (a) Growth rates g for samples from growth temperature series (red triangles, top x -axis) and oxygen partial pressure series (blue triangles, bottom x -axis). (b) Image of the samples produced at different oxygen partial pressures and different growth temperatures.

in this work support the direct transition nature of Cr_2O_3 [15, 30], it has to be noted that there exist studies determining the optical band gap of Cr_2O_3 by assuming an indirect transition nature [13, 20]. However, all of them utilize a TAUC plot $(\alpha E)^n$ vs. E , which is an unappropriate method for crystalline solids as discussed in 2.3.4. Therefore, the method based on the assumption of parabolic shape of bands as well as direct transitions (cf. 2.3.4) is used. Fitting the linear regime in the onset of absorption results in $E_{\text{opt}} \approx 3.6$ eV for both samples, which differ in strain and ω -FWHM by a factor of approx. 2 and 0.3, respectively.

Growth Temperature Variation on m -plane Sapphire

In the following, the results for the three samples produced at different growth temperatures are presented. Similar to the previous results, the (30.0) reflection of the α -phase of Cr_2O_3 can be observed (Fig. 3.6). Note that the additional peaks are corresponding to the (30.0) reflection of the substrate and stem from various radiation wavelengths. The calculated o.o.p. strain is shown in Fig. 3.2a and a large spread of strain can be observed, varying between 0.4 % and 1 %. Note that there is no systematic dependence on growth temperature. The ω -FWHMs of the Cr_2O_3 (30.0) reflection are shown in Fig. 3.2b and exhibit a similar spread as the samples with varying oxygen partial pressure, but similar to the o.o.p. strain, no dependence on growth temperature is observed. The φ -scans (Fig. 3.3) show that the thin films are in-plane aligned with the respective substrate and that no rotational domains are present. Finally, the growth rate varies between $3.5 \text{ pm pulse}^{-1}$ and 10 pm pulse^{-1} with no observable dependence on growth temperature.

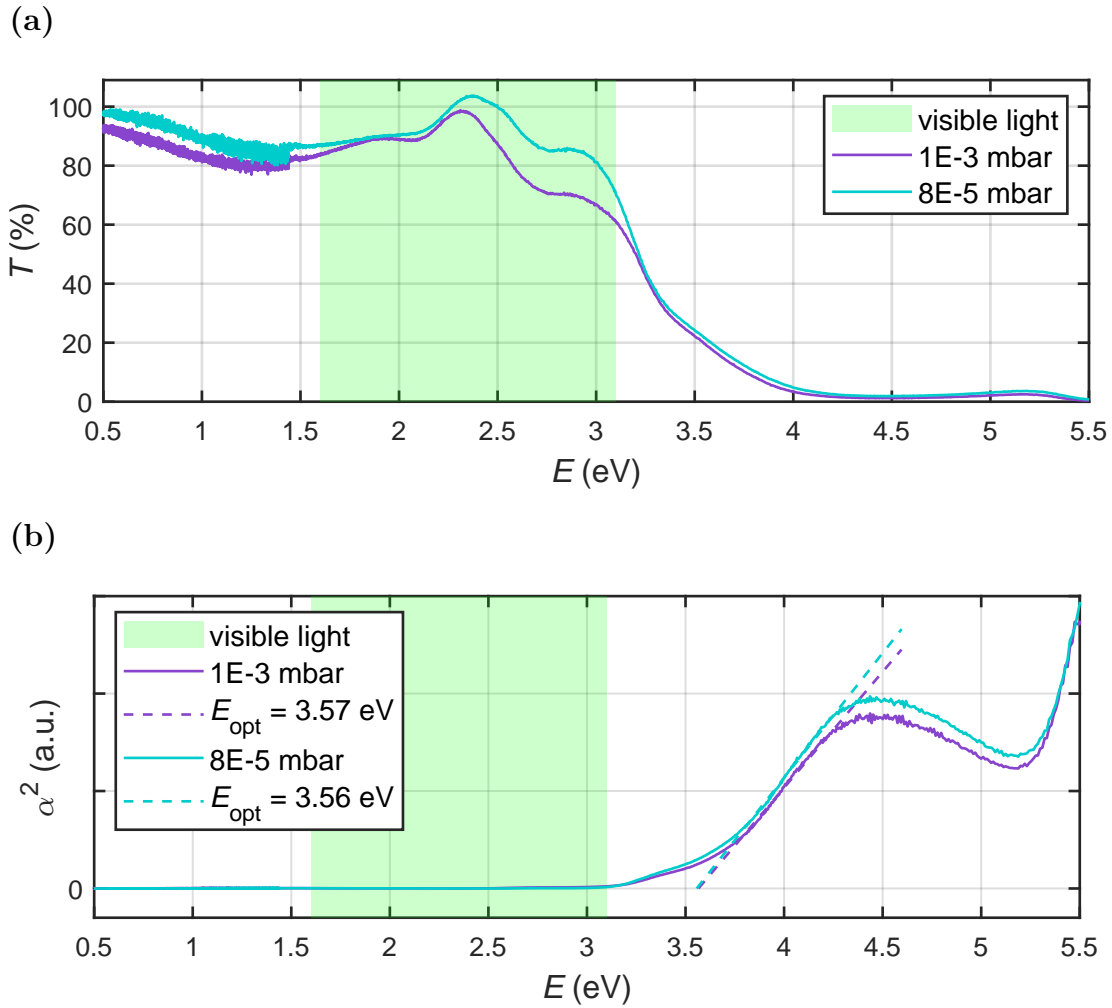


Figure 3.5: (a) Transmission spectra of two selected Cr_2O_3 thin films, deposited with different oxygen partial pressures. The spectra are normalized to a corresponding uncoated m -plane sapphire substrate. (b) α^2 vs. E plot of the above-mentioned samples. It is assumed that Cr_2O_3 has a direct bandgap [15, 30]. The fitting regime is chosen to be between 3.75 eV and 4.3 eV.

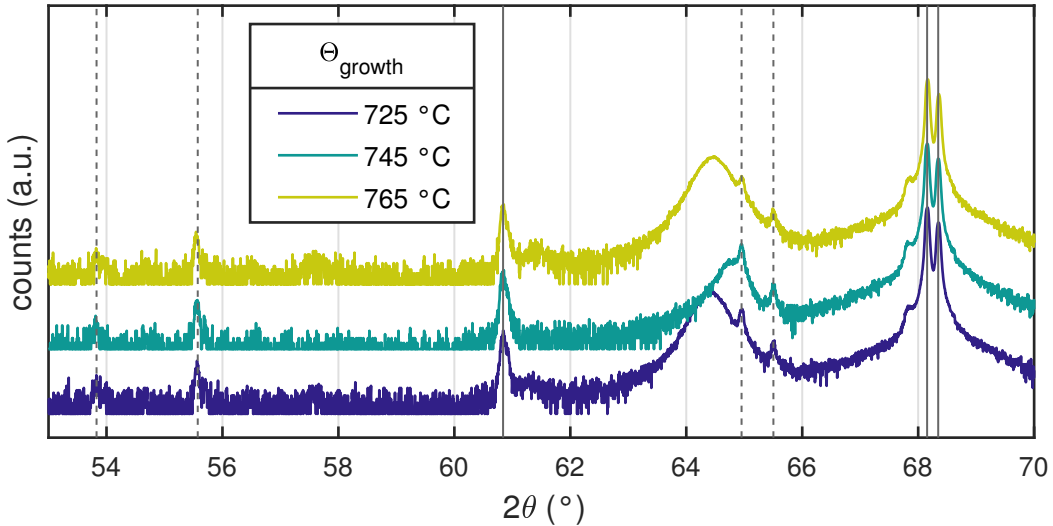


Figure 3.6: 2θ - ω -pattern of Cr₂O₃ thin films deposited on *m*-plane sapphire for three different growth temperatures. The lines indicate substrate reflections that stem from copper and tungsten radiation (cf. 3.1)

Influence of Growth Rate on Crystal Structure

It has to be noted that there is a large spread in strain and ω -FWHM for the samples that were deposited at different growth temperatures. The range of temperature variation was only 40 °C and has no significant influence on the distribution of strain and ω -FWHM (Fig. 3.2). Because all the other process parameters were kept the same⁽⁴⁾, this indicates that another parameter influences the crystal quality. This is supported by the fact that the growth rate correlates with the magnitude of strain and ω -FWHM, as can be seen in Fig. 3.7a. Although strain is related to ω -FWHM, it has to be noted that for a small regime of o.o.p. strain around approx. 0.9 %, the ω -FWHM scatters between approx. 37' and 47'.

The origin of the varying growth rate – and therefore varying crystal quality – can be found when taking the number of processes into account that were performed before. In Fig. 3.7b, the growth rate is visualized depending on the order of sample fabrication. It is also indicated when the laser entrance window has been cleaned. It is common practice to clean the latter every couple of processes due to coating with target material which absorbs laser energy. But from Fig. 3.7b it becomes clear that this should be done much more frequently when working with Cr₂O₃. Note that the laser has a wavelength of 248 nm, corresponding to 5.0 eV, which is not transmitted by Cr₂O₃ thin films⁽⁵⁾, as can be seen in Fig. 3.5a. Therefore, the increasing coating of the laser entrance window with each new process absorbs a large amount of laser pulse energy, resulting in less fluence on the PLD target. This results in less ablated target material and less kinetic energy of the ablated species, which leads to a reduced growth rate and different crystal growth conditions that have higher strain and ω -FWHM as a result.

⁽⁴⁾ In fact, for the last two samples produced ($\Theta = 725$ °C and $\Theta = 765$ °C), the pulse number was increased to 40 000 pulses. This was due to the fact that the growthrate decreased.

⁽⁵⁾ To be precise, the transmission spectrum in Fig. 3.5a is recorded for *m*-plane oriented *crystalline* Cr₂O₃ thin films. This may not be the present phase when Cr₂O₃ deposits on the (colder) window made out of glass, where it may form an amorphous phase.

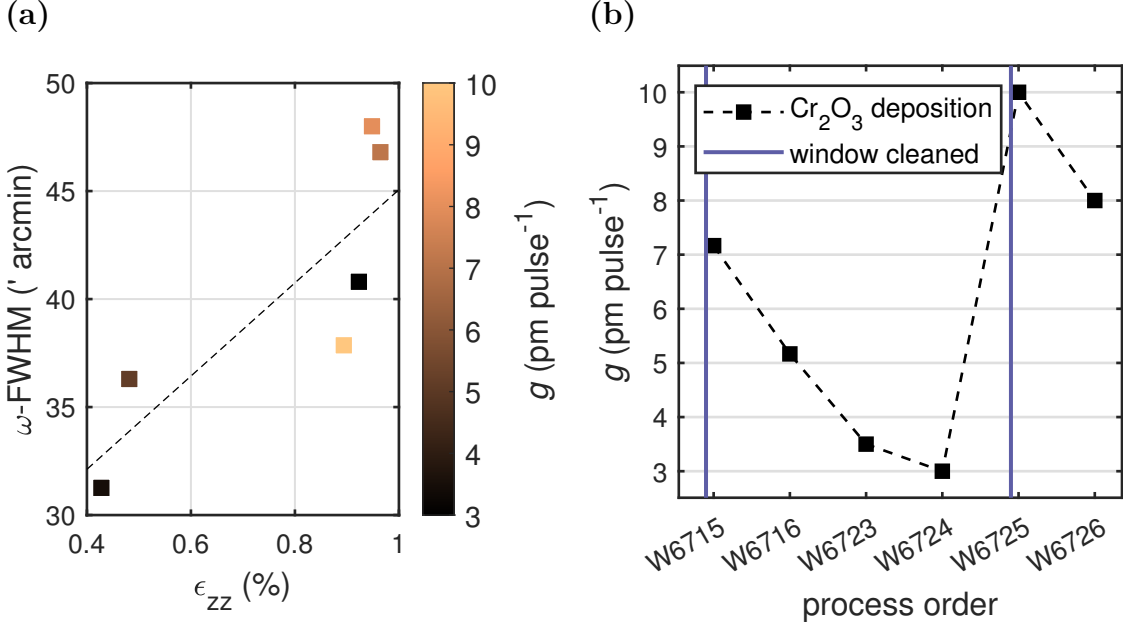


Figure 3.7: (a) Correlation of ω -FWHM with o.o.p. strain, as well as correlation of both with growth rate g (false color). The dashed line is a linear fit serving as guide to the eye. (b)

This explanation is supported by the dependence of crystal quality on oxygen partial pressure (cf. Fig. 3.2). There, the increment of crystal quality with higher oxygen pressures is attributed to the increased background gas scattering resulting in less kinetic energy of the plasma material. This also explains the outlier in Fig. 3.7a, where one sample corresponds to a higher strain and ω -FWHM of approx. 0.9 % and 41', respectively (black square). This is not expected when considering the rather small growth rate of 3 pm pulse $^{-1}$ (W6724 in Fig. 3.7b). But when taking account for the fact that this sample is fabricated at a very low oxygen partial pressure of 8×10^{-5} mbar, it becomes clear that although the reduced fluence on the target would generally lower the kinetic energy of the plasma material, the limited scattering with the background gas counteracts this effect, resulting in the observed crystal quality.

It is noteworthy that the observed strain (cf. Fig. 3.2a) is distributed around two distinct values of approx. 0.4 % and 0.9 %. A prior reported thin film tilt for m -plane oriented rhombohedral heterostructures [64] may be the reason for this observation: the samples are installed in the XRD device in such a way that the c -axis is either parallel or orthogonal to the scattering plane. This orientation is arbitrary, and thus the (expected) thin film tilt is either along the X-ray beam or perpendicular to it, which could result in unexpected results when calculating the o.o.p. lattice plane distance from the observed peak position. To check if this is the origin of the observed strain, for two samples of different strain according to Fig. 3.2, four $2\theta-\omega$ -scans were performed with incrementing the azimuth by 90° after each measurement. The resulting diffraction patterns are depicted in Fig. 3.8. The strain is independent of azimuth, only the peak intensity is altered by the in-plane rotation of the sample. For both samples, an azimuth of 0° and 180° results in a lower intensity, supporting the hypothesis that the (expected) thin film tilt is perpendicular to scattering plane which results in a deviation from the BRAGG condition. Therefore, the distribution of observed strain is not a measurement

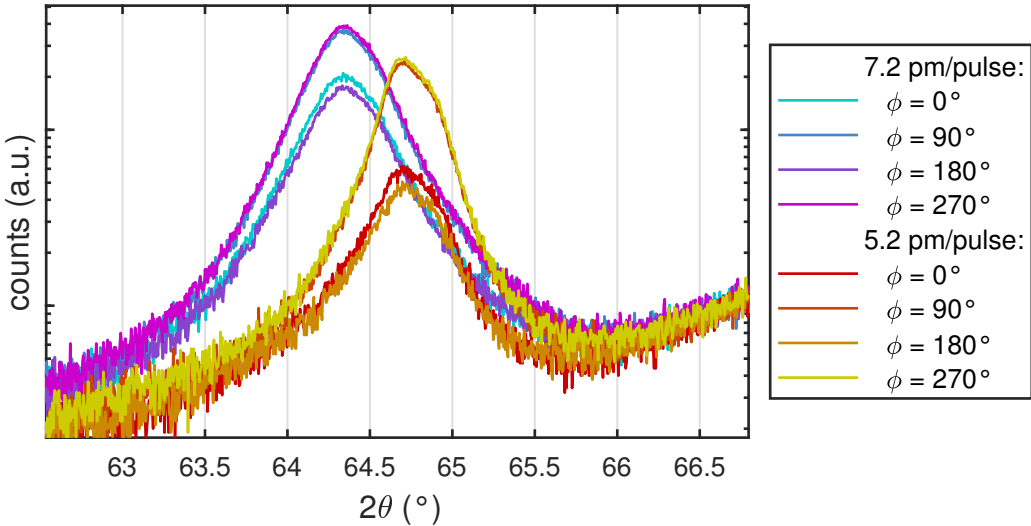


Figure 3.8: 2θ - ω -patterns for two samples in four different azimuths each.

Table 3.1: Structural parameters, approximate resistivity at room temperature and activation energy for Cr_2O_3 thin films of different orientation.

Plane	ϵ_{zz} (%)	ω -FWHM (')	ρ ($\Omega \text{ cm}$)	E_A (meV)
<i>c</i>	1.71	42.6	3	57, 34
<i>r</i>	0.72	38.4	120	117
<i>m</i>	0.55	42.6	3600	240
<i>a</i>	1.41	32.4	4900	259

artifact.

Deposition on *c*-, *r*-, *m*- and *a*-plane Sapphire

For the samples deposited on substrates with different orientation, 2θ - ω -patterns were recorded (Fig. 3.9). For each sample, the expected substrate peaks are observed: (00.6) and (00.12) for *c*-plane; (01.2), (02.4), (03.6) and (04.8) for *r*-plane; (30.0) for *m*-plane; (11.0) and (22.0) for *a*-plane. Several smaller peaks also correspond to those reflections but stem from other X-rays than Cu-K α (cf. Fig. 3.1). The mentioned reflections are also observed for the Cr_2O_3 thin film, but with a shift in 2θ position similar to the previously investigated *m*-plane samples (Tab. 3.1). Note that for *r*-plane, the higher order reflections of Cr_2O_3 cannot be observed. It can be concluded that Cr_2O_3 grows in the α -phase on sapphire substrates of different orientation, where the thin film orientation matches the corresponding substrate. Henceforth, “*c*-plane Cr_2O_3 ” will refer to a Cr_2O_3 thin film deposited on *c*-plane oriented $5 \times 5 \text{ mm}^2$ sapphire substrates, and so on. For each sample, ω -scans were performed on the (00.6), (02.4), (30.0) and (11.0) reflections for *c*-, *r*-, *m*- and *a*-plane, respectively. The resulting ω -FWHMs are in the range of approx. $30'$ to $40'$ (Tab. 3.1).

Because the resistivity of all samples was too high to measure Hall effect, only resistivity measurements (cf. 2.3.2) were performed for several temperatures (Fig. 3.10). The resistivity depends strongly on the orientation of the thin film, the resistivities at

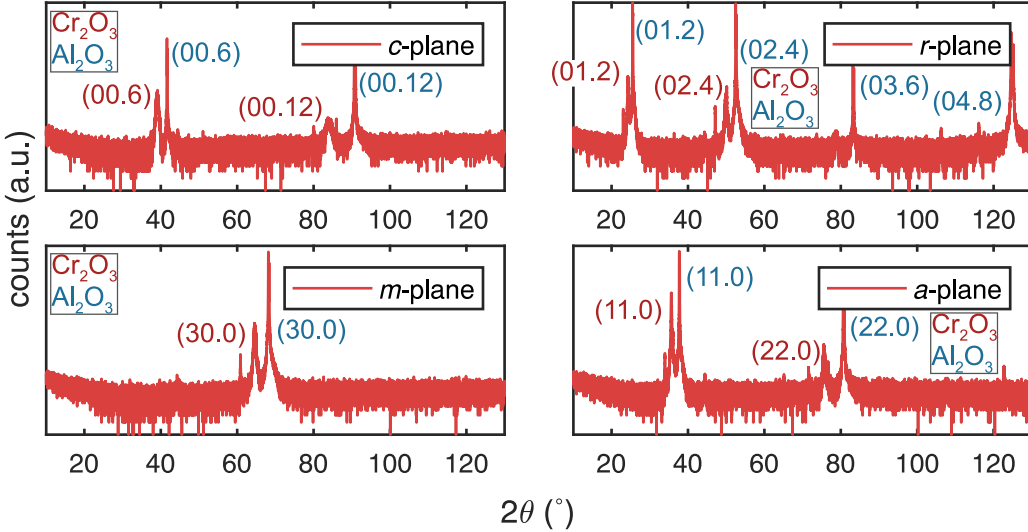


Figure 3.9: 2θ - ω -patterns of Cr_2O_3 thin films deposited on *c*-, *r*-, *m*- and *a*-plane sapphire.

room temperature are listed in Tab. 3.1. A difference of more than three orders of magnitude between *c*-plane and *a*-plane samples is observed. The linear behavior of the ARRHENIUS-plot⁽⁶⁾ indicates a thermally activated mechanism for conductivity, and thus semiconductive behavior. Note that no further conclusions can be drawn on the conduction mechanisms due to the missing carrier concentration and mobility data. By assuming a behavior of the form

$$\rho \propto \exp\left(\frac{E_A}{k_B T}\right), \quad (3.2)$$

with BOLTZMANN constant k_B , an activation energy E_A can be estimated. Those energies are also listed in Tab. 3.1. For *c*-plane Cr_2O_3 , two linear regimes can be distinguished, favoring a dependence of the form

$$\rho \propto a \exp\left(\frac{E_{A,1}}{k_B T}\right) + b \exp\left(\frac{E_{A,2}}{k_B T}\right), \quad (3.3)$$

thus two activation energies are determined.

3.1.3 Conclusion

m-plane Cr_2O_3 thin films can be deposited over a wide range of oxygen partial pressure of more than 2 orders of magnitude. It turned out that the main influence on the crystal quality correlates with the growth rate and is due to a variation of the laser pulse fluence on the target. Nevertheless, an oxygen partial pressure of 1×10^{-3} mbar and a growth temperature of 750°C are chosen for deposition of subsequent thin films. α - Cr_2O_3 could also be deposited on *c*-, *r*- and *a*-plane sapphire, with the thin films crystallizing in the respective orientation. Note that all deposited thin films showed a discrepancy between observed o.o.p. lattice plane distance and values predicted from Tab. 1.1. The

⁽⁶⁾ Visualization of $f(T)$ as $f'(\tau)$ with $f' = \log f$ and $\tau = 1/T$.

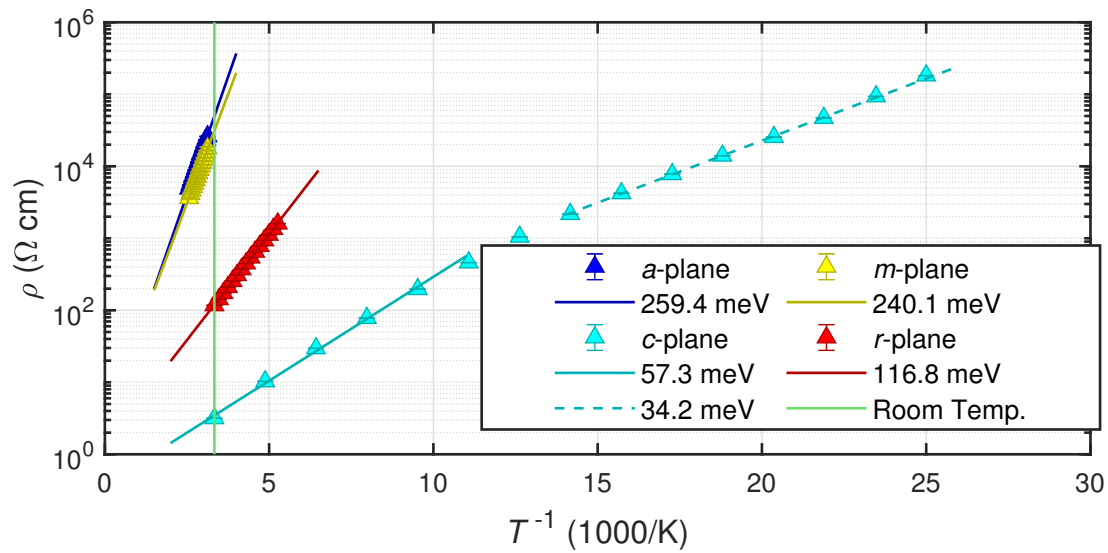


Figure 3.10: Temperature dependent resistivity measurements for samples with different orientations.

conductivity is strongly dependent on the crystal orientation and was very low for the prismatic orientations, but with 0.3 S cm^{-1} three orders of magnitude higher for the basal orientation.

3.2 Doping of Cr₂O₃ Thin Films

The resistivity of the Cr₂O₃ thin films showed strong dependence on thin film orientation. To improve and tailor the conductivity, it is tried to incorporate acceptors into the *p*-type material. The elements chosen for this are Cu and Zn, because doping has already been accomplished on *c*-plane sapphire with magnesium via MgO [30]. Furthermore, it is tried to reduce the sheet resistance of the contacts of the thin films.

3.2.1 Experiment

To fabricate doped thin films, three different PLD targets were applied. Each target was elliptically segmented (cf. 2.1.1), with the outer region consisting of pure Cr₂O₃. The inner region (ellipse) was also Cr₂O₃ but with a fraction of dopant, namely:

1. 0.01 wt.% CuO, called “CuO-doped”,
2. 0.01 wt.% ZnO, called “ZnO-doped (low)” and
3. 1 wt.% ZnO, called “ZnO-doped (high)”.

For each target, several processes were done with the laser spot position varying on the target. For each process, deposition was done on all of the 4 aforementioned substrate orientations to check whether the conductivity of the prismatic orientations could be improved. The composition of the ablated material can be calculated via Equ. (2.1), but this does not account for the finite area illuminated by the laser pulse. A simple model for including this effect can be achieved by simulating N several randomly distributed points r_i in the range Δr around a radial laser position r_{PLD} . Then, the composition x_D can be calculated as the mean of the N calculated compositions for each r_i . The resulting dependence of x_D on r_{PLD} is visualized in Fig. 3.11a, where a higher value of Δr results in more smeared out graphs. A target with inner concentration of 0.01 wt.% dopant was assumed (Cu-doped target or Zn-doped (low) target). The Monte Carlo simulations can further be approximated by a linear fit, which was done for $\Delta r = 2$ mm (blue dotted line in Fig. 3.11a). Henceforth, the different samples fabricated with different radial laser spot positions r_{PLD} are characterized by the expected composition x_D calculated from this linear fit. The reason for this is that according to Equ. (2.1), when applying r_{PLD} smaller than the length of the semi-minor axis of the inner ellipse, no variation in composition would be observed, even though the real finite laser spot size results in a different result. Note further that due to the small concentration of dopant, it is not possible to resolve those fractions via element sensitive measurements. Dr. Daniel Splith kindly performed Energy-dispersive X-Ray Spectroscopy (EDX) measurements that resulted in no signal for either Cu or Zn that was above the noise level.

To improve the contacts for resistivity measurements, samples were produced using the ZnO-doped (low) target and a fixed $r_{PLD} = 3$ mm. Only *c*- and *r*-plane sapphire substrates were used and the deposition temperature was varied between 560 °C and 680 °C. For each growth temperature, subsequent contacting was done with Ti-Al-Au for a *c*-plane and an *r*-plane sample, as well as Ti-Au for a *c*-plane and an *r*-plane sample. Furthermore, the *c*-plane samples contacted with Ti-Al-Au were compared before and after annealing at 210 °C in nitrogen atmosphere.

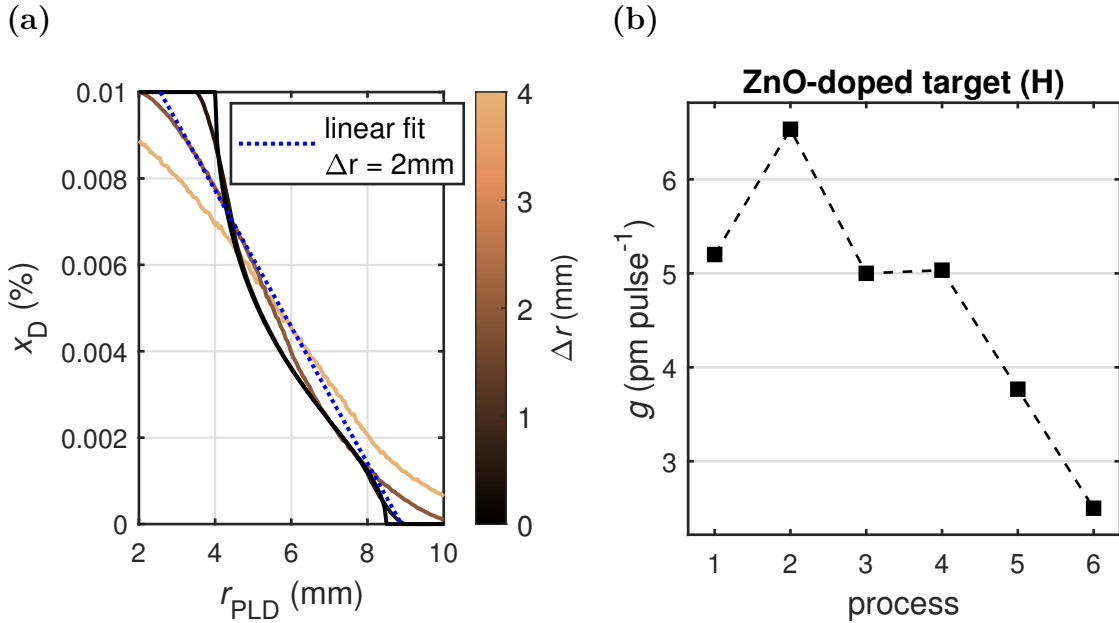


Figure 3.11: (a) Predictions for the plasma plume composition x_D using Monte Carlo simulations with $N = 10\,000$ and different values for Δr . The blue dotted line is a fit for the Graph calculated with $r = 2$ mm. (b) Growth rate depending on the process order for the samples fabricated from the ZnO-doped (high) target. The laser entrance window was cleaned after each process.

2 θ - ω -scans were performed for every sample, but ω -scans for c - and r -plane samples only. The thickness was determined using spectroscopic ellipsometry. Resistivity measurements at room temperature were done using the PAUW method, which was also applied when conducting temperature dependent resistivity measurements on one c -plane sample of each target. Note that the effect of infrequent cleaning of the laser entrance window that was described in 3.1 was discovered during the execution of those experiments, which is why the samples produced from the ZnO-doped (high) target were the only ones for which this effect could be prevented. Furthermore, 40 000 pulses were applied for the samples fabricated from the CuO-doped and ZnO-doped (low) target, as well as one sample from the batch made with the ZnO-doped (high) target. All other samples from this batch were deposited with 30 000 pulses.

3.2.2 Results

Laser Position Variation for Different Targets

The growth rates of the samples produced from the CuO-doped and ZnO-doped (low) target are depicted in Fig. 3.12. The growth rates vary between 3 and 6 pm pulse $^{-1}$ and depend strongly on the number of deposition processes that were conducted before. After cleaning the laser entrance window, and thus reducing laser energy absorption, the growth rate can be increased. This is similar to the results obtained in 3.1.

However, the growth rates depending on the fabrication order for the ZnO-doped (high) samples are depicted in Fig. 3.11b. Note that the growth rate varies from approx. 2.5 to 6.5 pm pulse $^{-1}$, even though the laser entrance window was cleaned after each

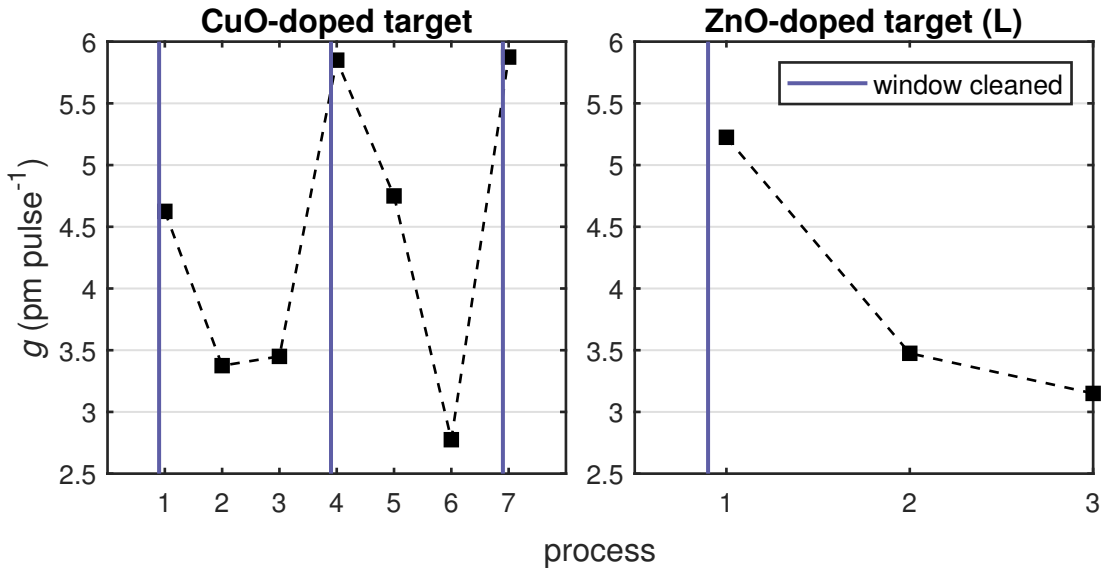


Figure 3.12: Growth rate depending on the process order for the samples fabricated from the CuO-doped and ZnO-doped (low) target. It is indicated when the laser entrance window was cleaned.

process. So this variation in growth rate must be traced back to another effect. Only the first sample was fabricated with 40 000 pulses, which explains the increment of growth rate between the first and second process: Due to the higher number of pulses, the laser entrance window gets more coated and thus the last 10 000 pulses reduce the average growth rate. Furthermore, the second process was done with $r_{PLD} = 6$ mm, which is rather outside compared to the 1st, 3rd and 4th process with 3 mm, 4 mm and 2 mm, respectively. This results in a larger total ablated area and in less target degradation. Therefore, the hypothesis is that target degradation during deposition has an influence on the growth rate. This is supported by the observation of incremental reduction of growth rate for processes 1, 5 and 6. Note that all these samples were fabricated with $r_{PLD} = 3$ mm and otherwise the same deposition parameters. The only variation is that tracks are carved into the target by the laser (Fig. 3.13c). This is probably the reason for a crucial change in plasma dynamics and therefore a reduction of the growth rate from approx. 5 to 2.5 pm pulse $^{-1}$.

For the samples with high conductivity, namely c -plane and r -plane, ω -scans were performed on the (00.6) and (02.4) reflection, respectively. The extracted ω -FWHMs are depicted in Fig. 3.14 depending on the growth rate for the respective process. A general trend is that the crystallinity increases for lower growth rates. It is not relevant, whether this reduction in growth rate is due to less fluence on the laser target due to infrequent window cleaning (CuO-doped and ZnO-doped (low) target) or due to target degradation (ZnO-doped (high) target). The better FWHM is achieved for c -plane samples. Note that for the deposition of Cr₂O₃ on r -plane sapphire from the ZnO-doped (high) target, no thin film peaks in 2θ - ω -scans (see below) were observed. Those X-ray-amorphous films are presumably a result of the drastically altered plasma dynamics due to target degradation.

In Fig. 3.15a, the measured resistivity at room temperature depending on the predicted dopant concentration is depicted. From the unsystematic variation in resistivity

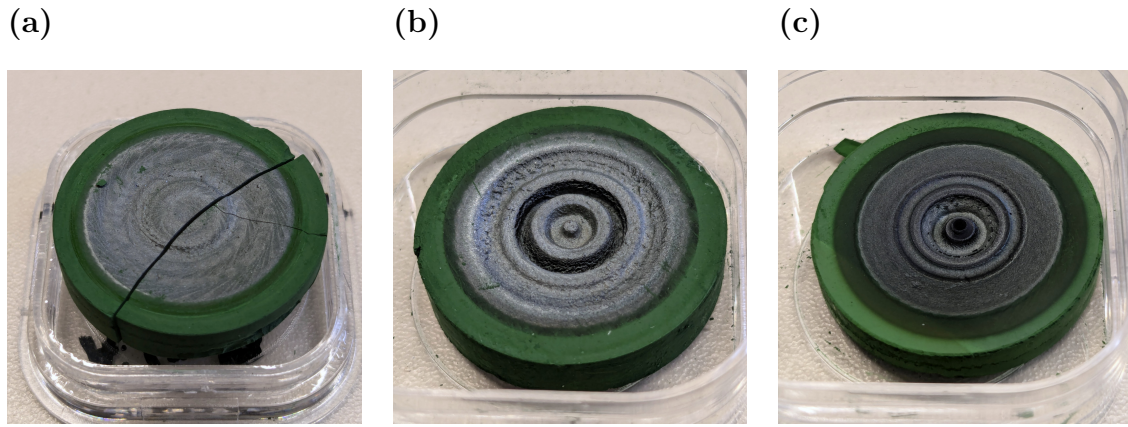


Figure 3.13: Photograph of the (a) CuO-doped, (b) ZnO-doped (low) and (c) ZnO-doped (high) target. The CuO-doped target broke during the last process where it was used. The silverish tint is presumably due to formation of metallic chromium oxide on the target surface.

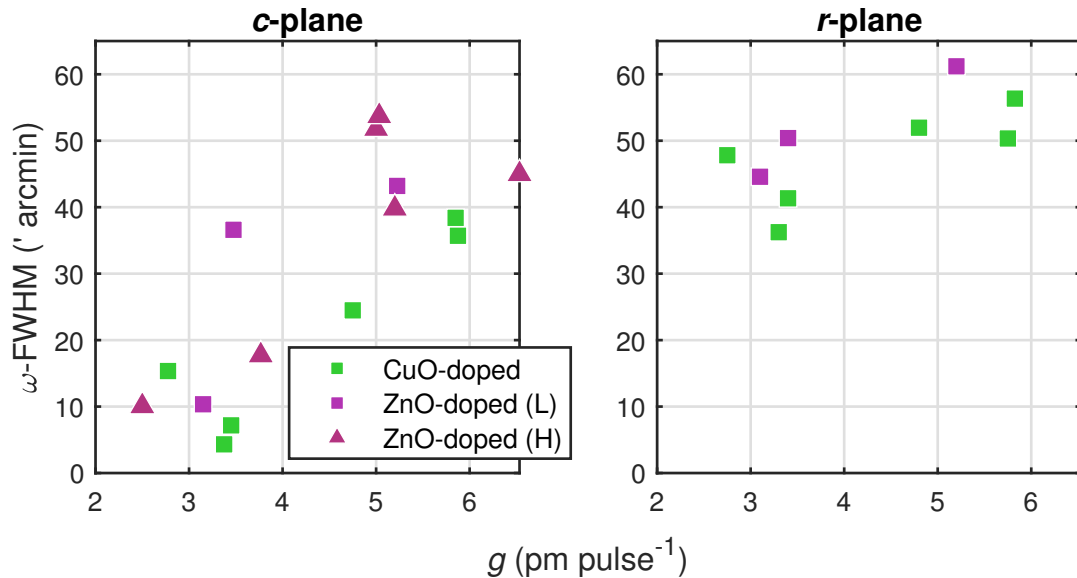


Figure 3.14: ω -FWHM for *c*- and *r*-plane samples that were fabricated from the three radially segmented targets.

Table 3.2: Activation energies E_A extracted from the linear regimes in the temperature dependent resistivity measurements (Fig. 3.16).

target	E_A (meV)	
	< 100 K	> 100 K
CuO-doped	53	83
ZnO-doped (low)	35	61
ZnO-doped (high)	31	50
pure Cr_2O_3	35	54

(2 to $500 \Omega \text{cm}$), it can be concluded that the attempt of doping the Cr_2O_3 thin films resulted in no improvement of conductivity. Using the two targets with different concentration of ZnO in the inner ellipse, no change was observed when adjusting x_D between 0.001 % and 1 %. Note the aforementioned samples that were all fabricated with $r_{\text{PLD}} = 3 \text{ mm}$ on the ZnO-doped (high) target, corresponding to the triangles in Fig. 3.15a at approx. $x_D = 1 \%$: here, the same process parameters yield samples differing in resistivity by 2 orders of magnitude. Because those samples showed different growth rates due to target degradation, it is plausible that this also influences the conductivity.

The growth rate influences the crystal quality (cf. Fig. 3.14) and therefore, in Fig. 3.15b, the resistivity depending on the ω -FWHM is depicted. It becomes clear that a higher mosaicity results in higher conductivity. Since more dislocations correspond to more crystal defects (cf. 1.3.2), this result is in accordance to the predicted influence of crystal defects on the electrical properties of Cr_2O_3 thin films (cf. 1.1.1). It has to be noted that this effect is less pronounced for r -plane samples compared to c -plane samples. Furthermore, this does not explain why m - and a -plane Cr_2O_3 exhibit such higher resistivity, because their ω -FWHM is comparable to the basal and pyramidal orientations (cf. Tab. 3.1).

For each target, one c -plane sample with presumably highest doping concentration (smallest r_{PLD}) was chosen to perform temperature dependent resistivity measurements in the range of 40 to 390 K (Fig. 3.16). For all samples, an ARRHENIUS-like behavior is observed with two linear regimes above and below 100 K, respectively. By applying Equ. (3.3), two activation energies can be extracted that are listed in Tab. 3.2.⁽⁷⁾ Note that the (arbitrary) choice, which samples were measured for each target, determined the absolute difference in resistivity: There are in fact samples fabricated from the CuO-doped target that have lower resistivity than samples fabricated from the ZnO-doped targets (cf. Fig. 3.15).

Even though the doping resulted in no improvement of the electrical properties of the thin films, the several samples fabricated at different growth conditions⁽⁸⁾ may serve as an insight into the o.o.p. strain that was already observed in 3.1. To check whether the hypothesis of increasing strain with increasing growth rate is also true for orientations other than m -plane, the o.o.p. strain dependent on the growth rate is depicted in

⁽⁷⁾ **Soll ich dazu noch mehr sagen? Ich weiß nicht, ob man sehr viel aus diesen Zahlen lernen kann.**

⁽⁸⁾ Even though these differences were achieved accidentally: by infrequent laser entrance window cleaning and repeated ablation on targets with the same laser spot position r_{PLD} .

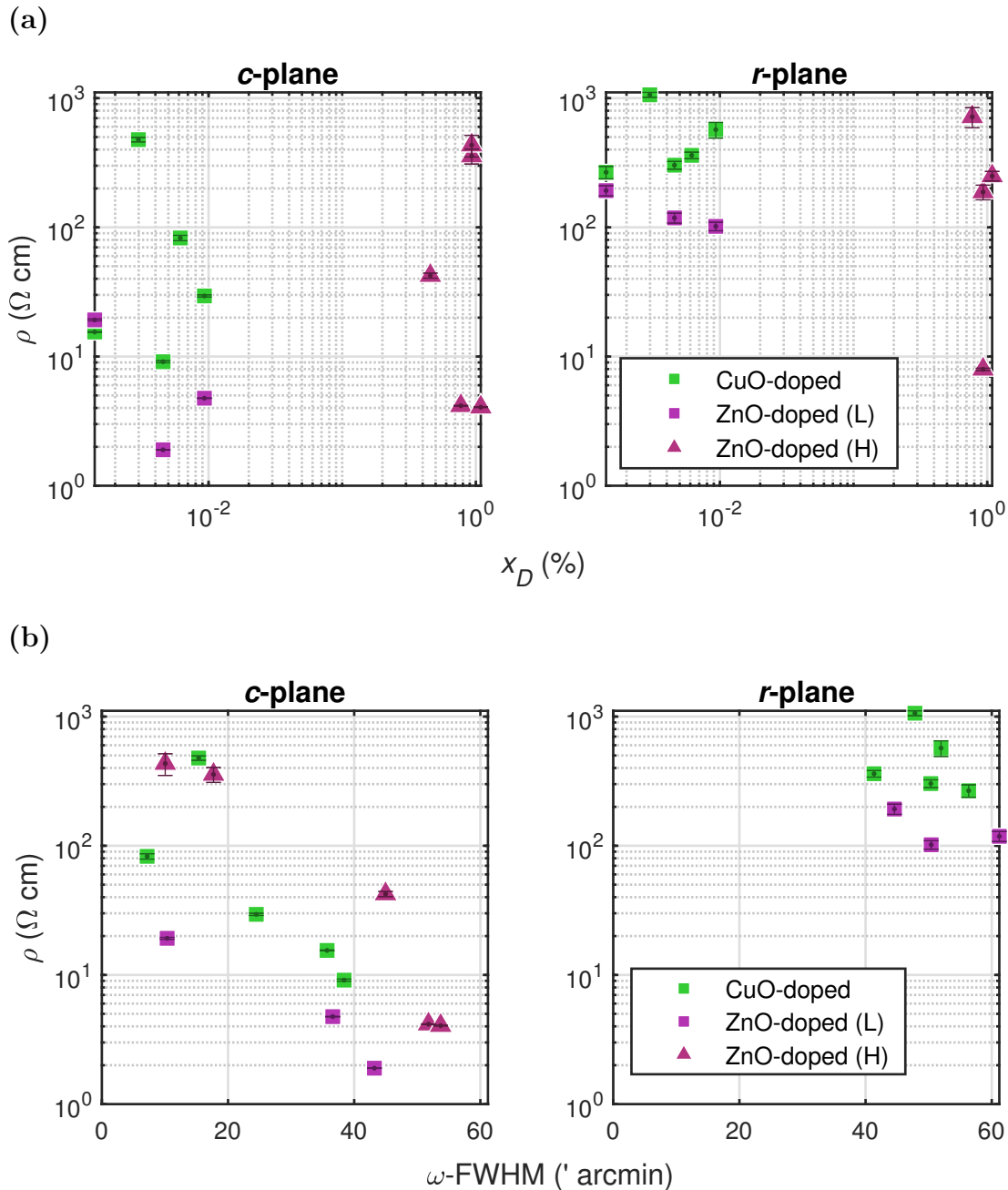


Figure 3.15: (a) Resistivity vs. predicted dopant concentration for *c*- and *r*-plane samples fabricated from all three radially segmented targets. (b) Resistivity vs. ω -FWHM (' arcmin) of the aforementioned samples.

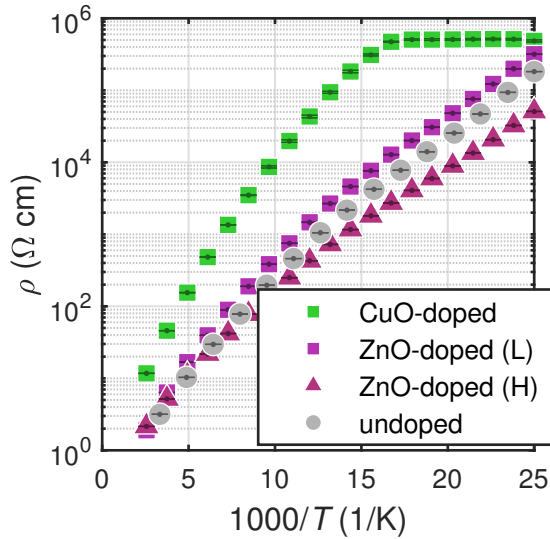


Figure 3.16: Temperature dependent resistivity measurements for *c*-plane samples fabricated from the different radially segmented targets, as well as a pure Cr_2O_3 target. The clipping of the sample from the CuO-doped target (green squares) is due to the limited resolution of the measurement device and the artifact nature of this saturation is confirmed by repeated measurements with different current applied during measurement (not shown).

Fig. 3.17a. For *m*- and *a*-plane, this behavior can indeed be observed. However, the slope of this relation differs depending on the target: the samples fabricated from the CuO-doped target showed less strain depending on growth rate than the samples fabricated from the ZnO-doped (high) target. This may be explained by the fact that the target degradation for the former (cf. Fig. 3.13a) was not so pronounced when compared to the latter (cf. Fig. 3.13c).

A reverse behavior is observed for *c*-plane samples: the strain is increasing with higher growth rates. But compared to *m*- and *a*-plane, there is no significant difference between the samples fabricated from different targets. This leads to the assumption that the plasma dynamics do not determine the o.o.p. strain for this orientation. It has to be noted that due to the constant pulse number, a change in growth rate corresponds to a change in thickness of the thin films. Therefore, it may be possible that the strain of the thin samples (low growth rate) is due to pseudomorphic growth on the corresponding Al_2O_3 substrate. Note that this leads not to the conclusion that the origin of the strain in *m*- and *a*-plane samples is also pseudomorphic growth: There, the thicker samples show more strain which is not expected because far away from the interface, dislocations should form to propagate relaxed growth. For *r*-plane samples, the overall strain is smaller and shows a less pronounced trend similar to *m*- and *a*-orientation. Because *r*-plane has both basal and prismatic character, both thickness and plasma dynamics effects may contribute to the observed strain.

The qualitative difference between *c*-plane and the other orientations can also be observed in Fig. 3.17b, where the ω -FWHM is shown depending on the o.o.p. strain. Compared to the previous results (cf. Fig. 3.7a), both factors characterizing crystal quality (strain and ω -FWHM) are not minimized simultaneously.

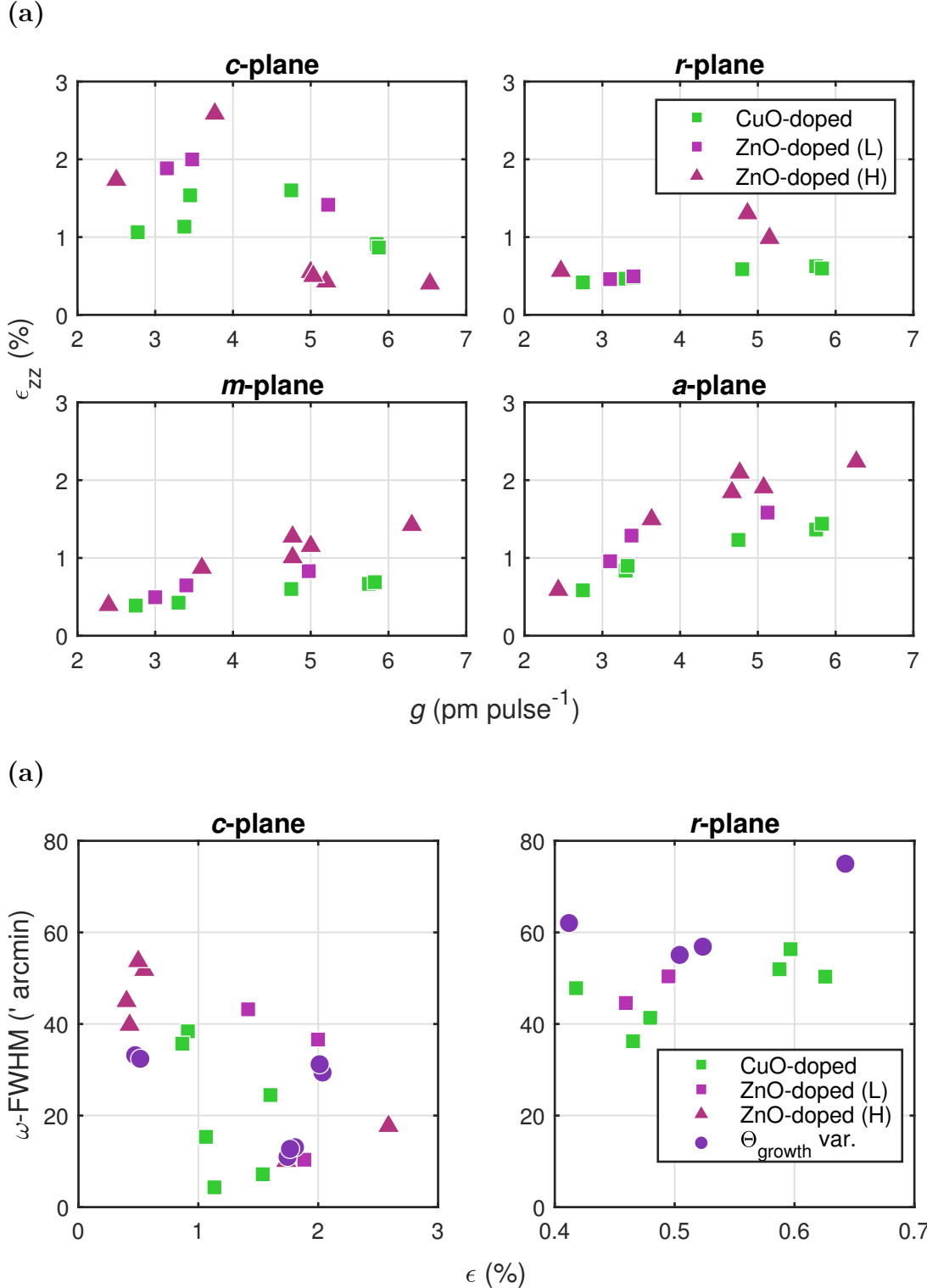


Figure 3.17: (a) Strain extracted from the peak positions in $2\theta\text{-}\omega$ -scans for samples fabricated from the three radially segmented targets. (b) Correlation between strain and $\omega\text{-FWHM}$ for *c*- and *r*-plane samples. The samples fabricated at different growth temperatures are also included.

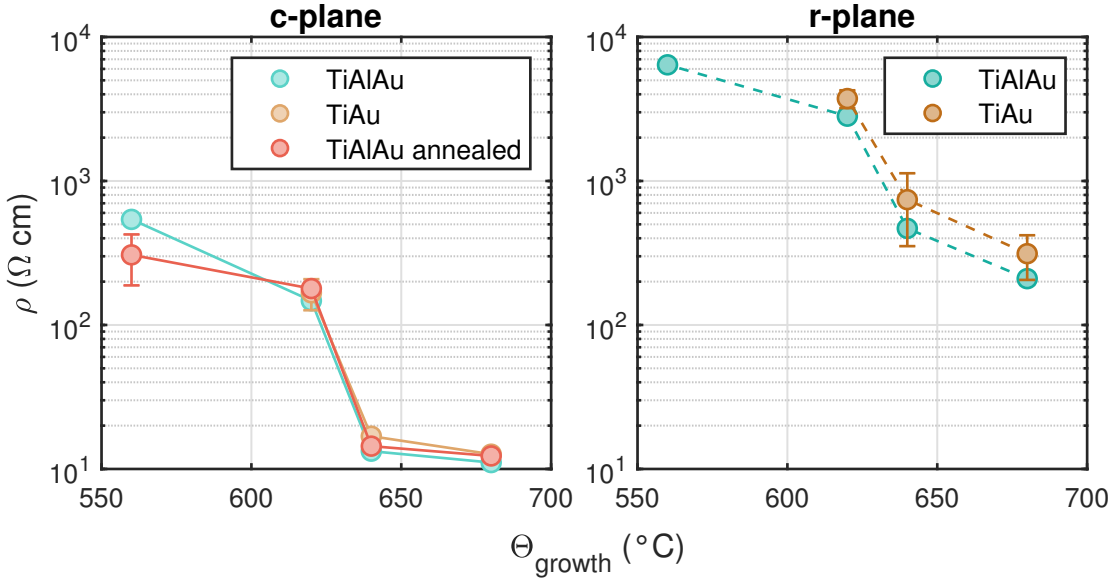


Figure 3.18: Resistivity measured at room temperature depending on growth temperature. Three different contact types were applied.

Ohmic Contact Optimization

For both *r*- and *c*-plane, a reduction in growth temperature results in higher crystallinity (not shown). Lower growth temperatures also yield higher resistivities, as shown in Fig. 3.18. This confirms the previously observed result, that the crystallinity reduces conductivity. It has to be noted that several effects influence the change in ω -FWHM: The first process was done at highest temperature, which was then gradually reduced. So the temperature reduction is convoluted with a process order effect. This is important, because for every sample, the same radial laser spot position $r_{\text{PLD}} = 3 \text{ mm}$ was used on the ZnO-doped (low) target, which led to increasing surface degradation (cf. Fig. 3.13b). This results, as shown before, in lower growth rates and higher crystallinities. This effect is supported by the fact that the window was cleaned before the first process only, which also adds to the subsequent reduction of laser fluence on the target surface. Therefore, the effect of temperature variation is covered by those growth rate effects, which makes it difficult to deconvolute the influence of growth temperature on conductivity. As can also be seen in Fig. 3.18, no significant change in resistivity was observed for both the variation between Ti-Al-Au and Ti-Au contacts, as well as between annealed and as-deposited contacts. For *r*-plane, the Ti-Al-Au contacts yielded slightly better conductivities.

3.2.3 Conclusion

The incorporation of CuO or ZnO had no effect on the conductivity of *c*- and *r*-plane oriented Cr_2O_3 thin films. None of the *m*- or *a*-plane oriented films became conductive. However, the conductivity depends strongly on the crystallinity, which indicates intrinsic defects as the origin of charge carriers. The crystallinity is mainly influenced by target degradation due to repeated ablation with the same laser spot position on the target. This results in lower growth rates and presumably less kinetic energy of

the plasma species which deposits on the substrate. Even though the doping attempt showed no effect, a discrete material library of Cr_2O_3 thin films with different strains was provided. A fundamental difference between *c*-plane and the other common orientations was observed, regarding the origin of the observed o.o.p. strain. Further measurements must be conducted to deconvolute the effects of (i) thickness, (ii) laser fluence on target and (iii) target degradation.

3.3 Strain Analysis

The structural properties of the thin film, namely its mosaicity and lattice distortion depend crucially on the growth process. It turned out that the absorption of energy at the laser entrance window alters the growth rate and the crystallinity much more dominantly than the growth temperature or the oxygen partial pressure (cf. 3.1). A similar effect was observed when targets were used for fabrication that exhibit a non-planar surface and tracks that were carved during previous ablations (cf. 3.2). Because the structural properties of the thin film also influence its electrical properties (cf. 3.2), the following investigations focus on the origin of the observed variations in strain and ω -FWHM. This is further motivated by the observation that a deliberate and controlled variation of laser spot size on the target surface yields a large reduction of ω -FWHM as well as a reduced shift of the peak position in the 2θ - ω -pattern (Fig. 3.19). This was achieved by varying the lens position (cf. 2.1) such that the laser spot size increases, yielding smaller fluence and larger ablation area on the target surface.

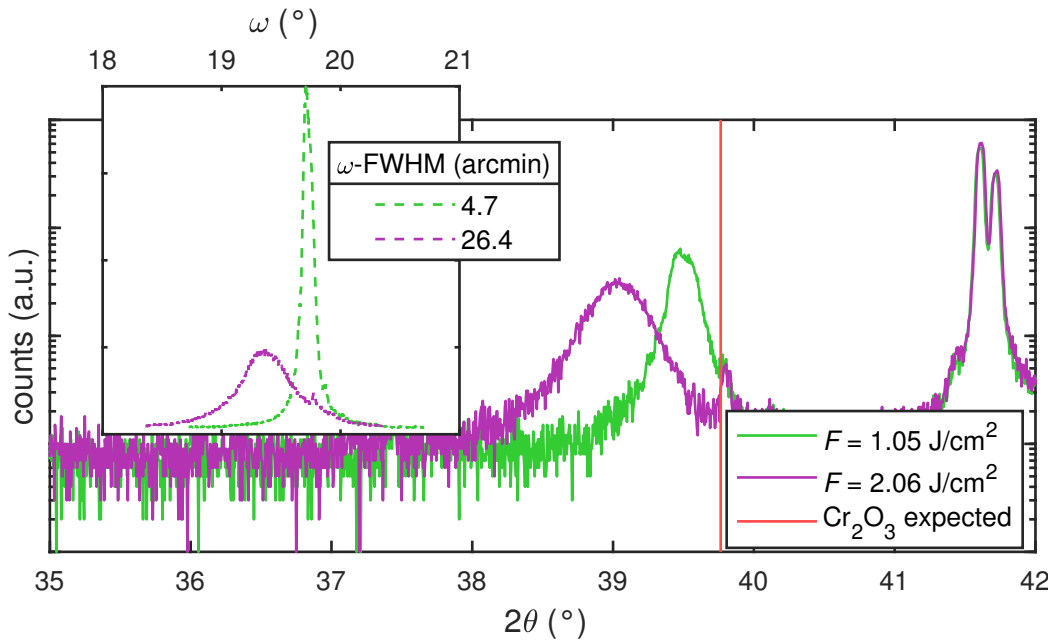


Figure 3.19: 2θ - ω -patterns for two *c*-plane samples fabricated with different laser focus on the target. The inset displays the diffractograms of the corresponding ω -scans performed on the respective reflections. The ZnO-doped (low) target was used without a fixed *rPLD* but with uniform ablation on the whole target surface.

3.3.1 Experiment

Sample Fabrication

For all following depositions, the laser entrance window was cleaned before each process. A pure Cr_2O_3 target was used for deposition of thin films on $5 \times 5 \text{ mm}^2$ sapphire substrates in the four aforementioned orientations. The first batch of samples was produced by only varying the pulse number to achieve a series of thin films with varying thickness but constant laser fluence during deposition. This is necessary, because the

series of thicknesses that was achieved in the prior experiments was correlated to a series of growth rates. The pulse energy was set to 650 mJ and the lens position⁽⁹⁾ to -2 cm , the resulting fluence is approx. 2 J cm^{-2} . This corresponds to the standard configuration during all previous processes (pink square in Fig. 2.2). This was repeated for three other lens positions, namely 0 cm , 1 cm and 2 cm , resulting in lower fluences: In Fig. 2.2, the yellow circles represent the probed laser fluences. This set of samples is referred to as the 1st batch.

To investigate the influence of fluence independent of ablation area, a 2nd batch of samples was fabricated with a fixed lens position (-1 cm) but varying laser pulse energy: 300 mJ, 450 mJ, 650 mJ and 800 mJ. The pulse number was adjusted to achieve approximately same thicknesses. The achieved fluences are visualized as red triangles in Fig. 2.2.

Measurements

For all samples, $2\vartheta\text{-}\omega$ -scans as well as ω -scans were performed. The reflections probed by the latter were (00.6) , (02.4) , (30.0) and (22.0) for c -, r -, m - and a -plane, respectively. For some selected samples of different thickness and fluence from the 1st batch, transmission measurements have been performed. Two of them were investigated via Atomic Force Microscopy (AFM) to obtain information about the surface morphology. The thickness of all samples was determined by spectroscopic ellipsometry measurements. To obtain more information about the relation between in-plane and out-of-plane lattice constants, RSMs were performed on selected samples:

c-plane For c -plane samples, the thickness series of the 1st batch that was fabricated with the largest laser spot size (lowest fluence) was investigated. The asymmetric reflection that was used for probing the relaxation process is (02.10) , which has an inclination angle of approx. 32° with respect to the sample surface.

r-plane All r -plane samples fabricated in the 2nd batch with different laser pulse energies were investigated with RSMs. For each sample, the x -axis of the sample – containing the projection of the c -axis – is found by performing a φ -scan on the (03.0) reflection: This set of lattice planes has an inclination with respect to the surface, so the position of the peak in the diffraction pattern of the φ -scan reveals the x -axis. In this azimuth, an RSM is recorded around the asymmetric (03.0) reflection and the symmetric (02.4) reflection. By rotating $\Delta\phi = 90^\circ$, the y -axis lays in the scattering plane and another RSM is performed around the symmetric (02.4) reflection. The twofold measurement of the symmetric reflection is necessary to calculate a possible lattice plane tilt for both x - and y -direction. Note that no shear is calculated due to the asymmetric nature of the (03.0) reflection with respect to the r -orientation⁽¹⁰⁾. After performing the various corrections described in 2.2.4, the tilt angles can be calculated

⁽⁹⁾ Note that the values for the lens position have an arbitrary offset; a value of 0 cm does not correspond to the position where the target surface is in focus.

⁽¹⁰⁾ For m - and a -plane rhombohedral structures, the crystal is symmetric under the transformation $\phi \rightarrow \phi + 180^\circ$, which is not the case for r -plane.

for both azimuths by

$$\theta = \arccos \left(\frac{q_{\perp}}{|\mathbf{q}|} \right) \cdot \text{sgn}(q_{\parallel}) , \quad (3.4)$$

with q_{\perp} and q_{\parallel} being the o.o.p. and i.p. components of the scattering vector \mathbf{q} , respectively. The i.p. and o.o.p. strains are determined by comparing the observed scattering vector to the expected scattering vector for the (03.0) reflection:

$$\mathbf{q}_{(03.0)} = |\mathbf{q}_{(03.0)}| \cdot \begin{pmatrix} \cos \alpha_{(03.0)|r} \\ \sin \alpha_{(03.0)|r} \end{pmatrix} , \quad (3.5)$$

with $|\mathbf{q}_{(03.0)}|$ calculated from Equ. (2.6) and Equ. (2.7). $\alpha_{(03.0)|r}$ denotes the angle between the (03.0) reflection and the normal of the r -planes; it can be calculated from Equ. (2.8):

$$\alpha_{(03.0)|r} = 90^\circ - (\alpha_{(03.0)|c} - \alpha_{(01.2)|c}) = \alpha_{(01.2)|c} = 57.62^\circ . \quad (3.6)$$

***m*-plane** Similar to above, all *m*-plane samples from the 2nd batch were investigated. The samples were aligned to the x -axis by performing a φ -scan on the asymmetric (30.6) reflection, and an RSM was recorded afterwards. By rotating $\Delta\phi = 180^\circ$ while maintaining 2θ and ω , the scattering condition for (30.6̄) is probed and an RSM was recorded. The symmetric reflection (30.0) was also measured in this azimuth. The tilt angle and shear angle can be calculated according to Equ. (3.4) and Equ. (2.13), respectively. The lattice constants can be calculated from the components of the scattering vectors:

$$a_{\perp} = \frac{\sqrt{12}}{q_{\perp}^{(30.\pm 6)}} , \quad (3.7)$$

$$a_{\perp} = \frac{\sqrt{12}}{q_{\perp}^{(03.0)}} , \quad (3.8)$$

$$c = \frac{6}{q_{\parallel}^{(30.\pm 6)}} . \quad (3.9)$$

a_{\perp} denotes the a lattice constant in direction of the normal to the sample surface. By rotating $\Delta\phi = 90^\circ$, the y -axis can be probed via asymmetric reflections (4̄2.0) and (22.0), which differ in the azimuth by $\Delta\phi = 180^\circ$. A second symmetric reflection (30.0) is recorded in this azimuth. Similar to the x -axis, the tilt and shear angles, as well as the lattice constants can be calculated:

$$(4\bar{2}.0) : a_{\perp} = \frac{\sqrt{12}}{q_{\perp}^{(4\bar{2}.0)}} , \quad a_{\parallel} = \frac{2}{q_{\parallel}^{(4\bar{2}.0)}} , \quad (3.10)$$

$$(22.0) : a_{\perp} = \frac{\sqrt{12}}{q_{\perp}^{(22.0)}} , \quad a_{\parallel} = \frac{2}{q_{\parallel}^{(22.0)}} , \quad (3.11)$$

$$(30.0) : a_{\perp} = \frac{\sqrt{12}}{q_{\perp}^{(03.0)}} . \quad (3.12)$$

a_{\parallel} denotes the a lattice constant parallel to the y -axis. For detailed calculations of the former equations, see A.1. Note that all 6 measured reflections yield a value for a_{\perp} ,

and 2 measured reflections each yield 2 values for c and a_{\parallel} , respectively. Therefore, for each lattice constant, the mean value is evaluated and the error is estimated by the standard deviation (cf. Fig. 3.30a).

a -plane All a -plane samples from the 2nd batch were investigated and the method is similar to the one applied to the m -plane samples. The azimuth of the x -axis is found by performing a φ -scan on the (22.6) reflection, which also served for an RSM. Rotating by $\Delta\phi = 180^\circ$ yields the (22.6̄) reflection and (22.0) is also measured. Similar to above, the sample is rotated by 90° to align to the y -axis and two more asymmetric reflections are recorded: (30.0) and (03.0). A second RSM of (22.0) is also performed. This yields the following lattice constants for the x -axis:

$$a_{\perp} = \frac{4}{q_{\perp}^{(22.\pm 6)}}, \quad (3.13)$$

$$a_{\perp} = \frac{4}{q_{\perp}^{(22.0)}}, \quad (3.14)$$

$$c = \frac{6}{q_{\parallel}^{(22.\pm 6)}}, \quad (3.15)$$

and for the y -axis:

$$(30.0) : a_{\perp} = \frac{2}{q_{\perp}^{(30.0)}} \cdot \frac{3}{2}, \quad a_{\parallel} = \frac{2}{\sqrt{3}q_{\parallel}^{(30.0)}} \cdot \frac{3}{2}, \quad (3.16)$$

$$(03.0) : a_{\perp} = \frac{2}{q_{\perp}^{(03.0)}} \cdot \frac{3}{2}, \quad a_{\parallel} = \frac{2}{\sqrt{3}q_{\parallel}^{(03.0)}} \cdot \frac{3}{2}, \quad (3.17)$$

$$(22.0) : a_{\perp} = \frac{4}{q_{\perp}^{(22.0)}}. \quad (3.18)$$

For detailed calculations and the origin of the factor $\frac{3}{2}$, see A.2. Again, lattice constants obtained from several reflections, the mean and standard deviation are calculated (cf. Fig. 3.30b).

3.3.2 Results

The analysis of the data will not be structured into the 1st and 2nd batch, but into the analysis of (i) c -plane, (ii) r -plane and (iii) m - and a -plane samples. In the following, some general remarks on the fabricated samples will be made.

In Fig. 3.20, a detailed view into the growth rates of the samples of the 1st batch is given. First of all, for a fixed fluence (false color), increasing the pulse number decreases the growth rate. This is expected, because the coating of the laser entrance window increases during the process. By fixing a pulse number to approx. 20 000 pulses, an increase in growth rate is observed for a regime of decreasing fluence from 2 to 1 J cm⁻² (Fig 3.20 bottom). This can be explained by the fact that the reduction of fluence is due to increasing laser spot size. When the fluence is still above the ablation threshold for the target material, an increasing ablation area results in an increasing growth rate. But at some point the fluence is too low to ablate the material and then the growth rate

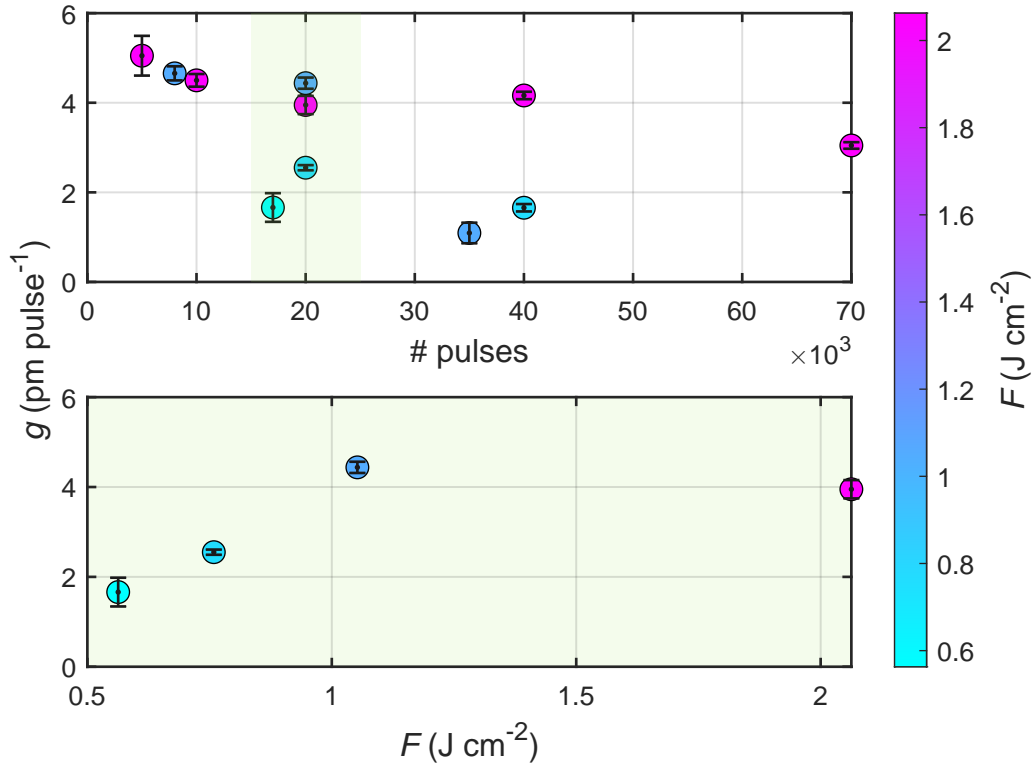


Figure 3.20: Growth rates of the samples from the 1st batch, depending on the pulse number (top) and depending on the laser fluence on the target for an approx. fixed pulse number (bottom). The data points are the mean of the four samples with another orientation each, that were obtained from every process. The errorbar displays the standard deviation.

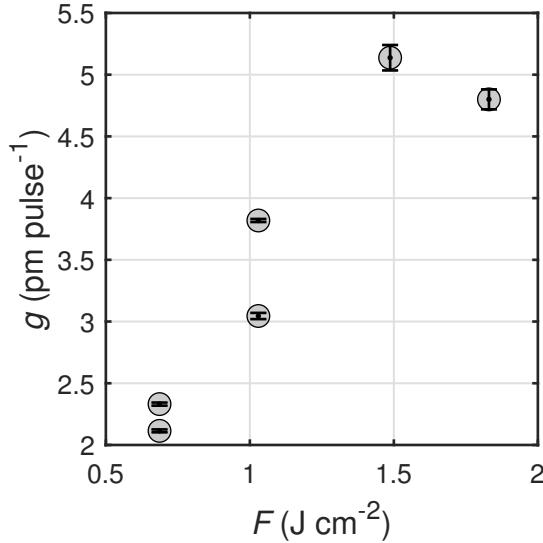


Figure 3.21: Growth rates of samples from the 2nd batch, depending on laser fluence on the target surface. The data points are the mean of thicknesses of the four orientations, similar to Fig. 3.20.

decreases, even though the ablation area increases. This can be observed at around 1.2 J cm^{-2} in Fig. 3.20, which is therefore an estimate for the ablation threshold. For the growth rates of the samples of the 2nd batch (Fig. 3.21), a similar conclusion can be drawn. Reducing the fluence via decreasing laser pulse energy below approx. 1.5 J cm^{-2} results in a decrease of growthrate from 5 to 2 pm pulse^{-1} . The ablation threshold can be localized between 1 J cm^{-2} and 1.5 J cm^{-2} , which is in accordance to the value obtained for the 1st batch.

c-plane: Laser Spot Size Variation

The o.o.p. strain calculated via Equ. (3.1) for all samples of the 1st batch is displayed in Fig. 3.22. Consider the *c*-plane oriented samples of the 1st batch, that had a fixed lens position yielding a fluence of approx. 2 J cm^{-2} , but varying thickness (brown squares in Fig. 3.22). A clear dependence of the o.o.p. strain can be observed: thinner samples yield higher strain. The layers become relaxed for thicknesses above approx. 170 nm . For low thicknesses, the strain approaches the predicted value for pseudomorphic growth of Cr_2O_3 on Al_2O_3 , which is 3.90% (cf. Tab. 1.3). The recorded RSMs of the (02.10) reflection can confirm whether this observation of o.o.p. strain is due to pseudomorphic growth. In Fig. 3.23, one can observe a shift of $q_{\parallel}^{(02.10)}$ to higher values for lower thicknesses. This corresponds to a decrease of the i.p. lattice constant, which is the expected behavior for pseudomorphic growth, because the i.p. a lattice constant of *c*-oriented Al_2O_3 is 0.2 \AA smaller than for Cr_2O_3 (cf. Tab. 1.1). The tensile o.o.p. strain observed via $2\theta-\omega$ -scans can also be confirmed by the fact that the o.o.p. component $q_{\perp}^{(02.10)}$ is decreasing for thinner samples. The reduction of signal intensity is attributed to the thickness, but could also be a result of decreasing crystal quality (cf. Fig. 3.24). When looking into the remaining samples that were fabricated with larger laser spot sizes but similar thickness (bluish squares in Fig. 3.22), it becomes clear that the o.o.p. strain is also slightly reduced for lower fluences. But note that this effect is less domi-

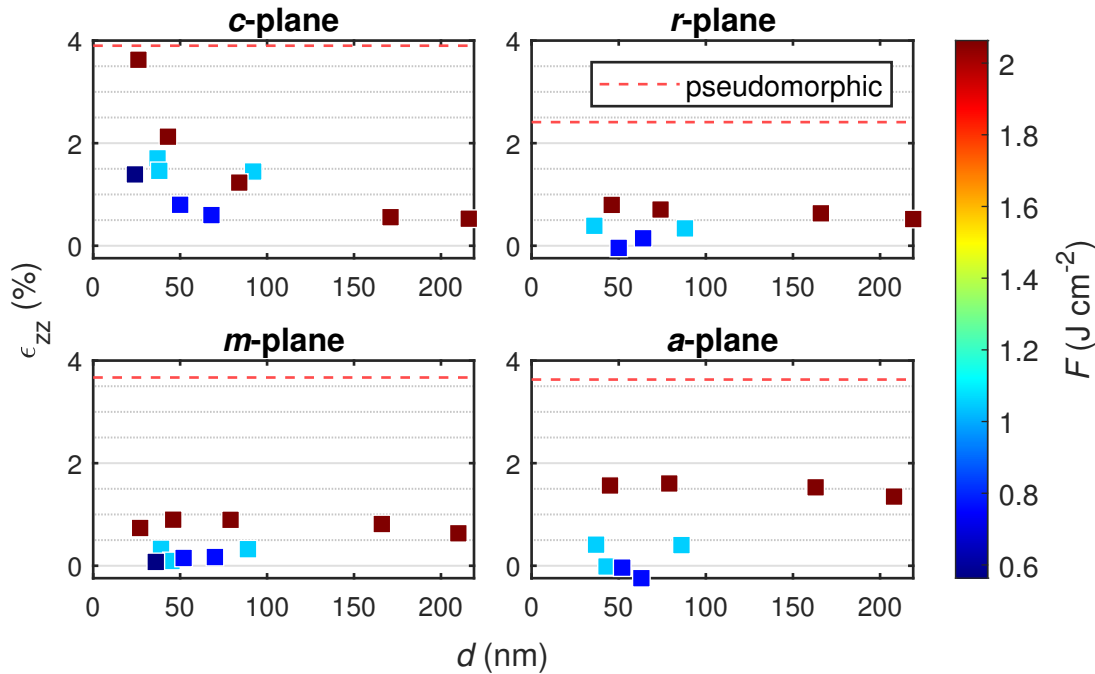


Figure 3.22: Out-of-plane strain calculated from $2\theta-\omega$ -patterns for all samples from the 1st batch, depending on thickness and laser fluence (false color).

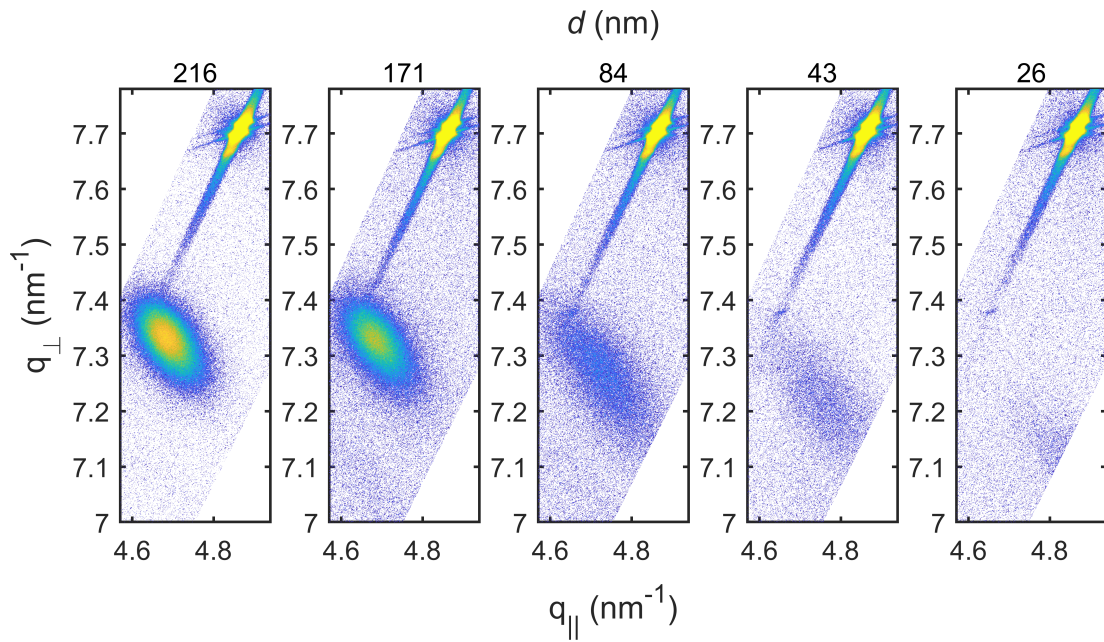


Figure 3.23: RSMs of the (02.10) reflection for several *c*-plane oriented samples of the 1st batch with varying thickness. The reflection in the upper right corner represents the (02.10) reflection of the sapphire substrate.

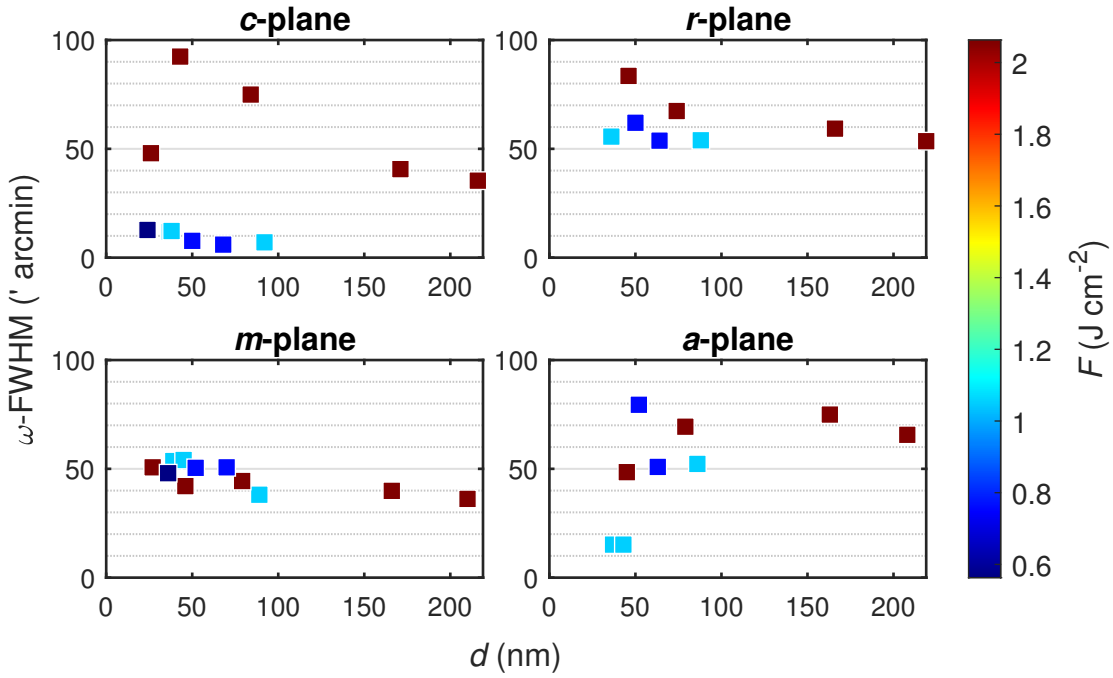


Figure 3.24: ω -FWHM for all samples from the 1st batch, depending on thickness and laser fluence (false color). The corresponding diffractograms are depicted in Fig. B.3.

nant when compared to the influence of thickness.

In Fig. 3.24, the ω -FWHM is depicted depending on the film thickness and laser fluence for the 1st batch. As before, consider the samples with smallest laser spot size (largest fluence) first: increasing the thickness is clearly correlated to a decreasing ω -FWHM. Therefore, thicker samples yield both less strained and more crystalline films. Note that there is an outlier to this behavior for the sample with a thickness of approx. 30 nm. When considering the ω -pattern of this sample (Fig. B.1a), it becomes clear that the non-VOIGT shape makes the determination of FWHM difficult. Therefore, not too much attention should be paid to this data point. When considering the samples fabricated with lower fluences (bluish squares in Fig. 3.24), a much more dominant influence of laser spot size on the crystallinity can be observed. This can be summarized by stating that the thickness of samples is the dominant influence on the o.o.p. strain, because the thickest samples yielded less strain than the thinner samples with lowest fluence (Fig. 3.22). However, for the ω -FWHM, it is the other way around, namely that even the thinnest samples (which exhibit better quality than thinner samples of same lens position) have a much higher ω -FWHM when compared to thinner samples fabricated with less fluence. This can be seen in Fig. 3.25, where the ω -FWHM is visualized depending on the o.o.p. strain of the corresponding sample: A linear behavior (correlation) is observed for each set fluence; but there are two different regimes in total, with the high-fluence regime generally showing higher ω -FWHM.

c-plane: Pulse Energy Variation

The o.o.p. strain for the *c*-plane oriented samples fabricated with various laser pulse energies, but constant laser spot size, are depicted in Fig. 3.26. Note that there is still a distribution of thickness from 100 to 200 nm, even though the pulse number was adapted

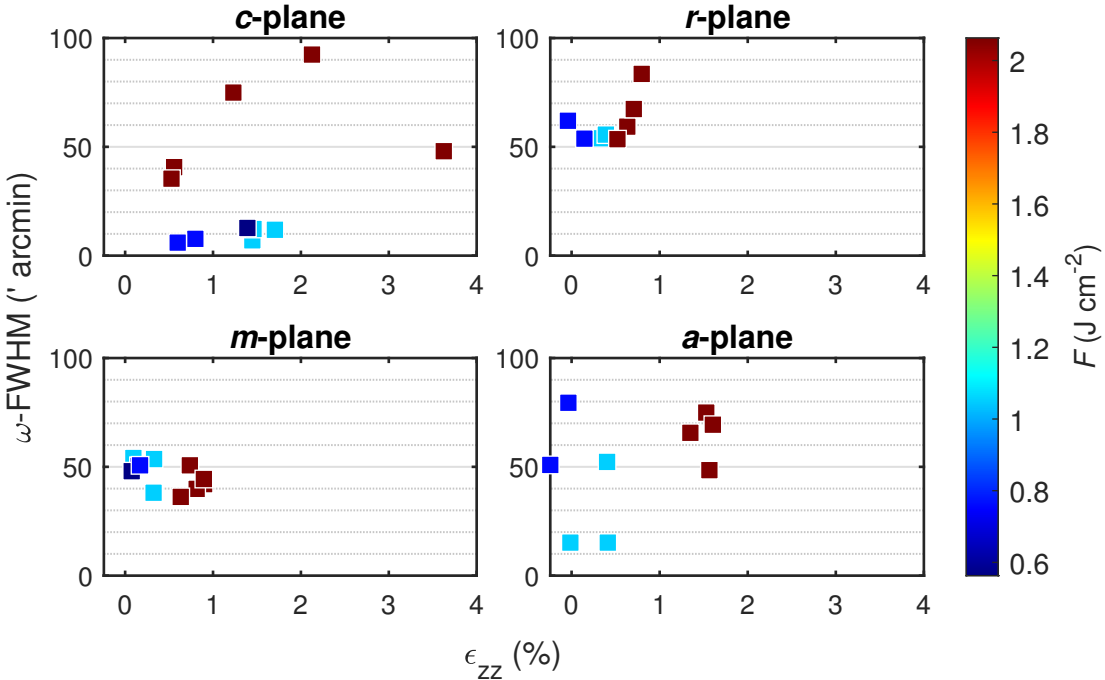


Figure 3.25: Correlation between strain and ω -FWHM for all samples from the 1st batch, depending on thickness and laser fluence (false color).

to the corresponding laser pulse energy. The strain is overall smaller ($< 2\%$) than for the 1st batch, because the 2nd batch contained samples with thickness $t > 100 \text{ nm}$ which yields smaller strains as seen before. No systematic dependence on the laser fluence is observed, which may be explained by the still remaining thickness distribution which overlaps the fluence variation. This effect could be strong enough to overshadow the impact of laser pulse energy, as it was shown in the previous experiment that the thickness is the dominant factor for the o.o.p. strain. For example, note the sample fabricated with $F = 1.5 \text{ J cm}^{-2}$ (dark green square in Fig. 3.26), which exhibits the lowest strain, even though having higher fluence value than other samples. This can be explained by the fact that with $t = 200 \text{ nm}$, it is the thickest sample of the batch.

In Fig. 3.27, the ω -FWHM is depicted depending on the laser fluence and film thickness for the 2nd batch. The previously observed relation is confirmed: increasing fluences result in higher ω -FWHMs. Namely, reducing the fluence by a factor of 2 results in a crystal quality improvement by one order of magnitude. Note that for a fluence of approx. 1 J cm^{-2} , two samples A and B with same thickness of 150 nm exhibit very different ω -FWHM of $\Delta\omega_A = 8'$ and $\Delta\omega_B = 49'$. The ω -patterns are depicted in Fig. B.1b. Note that both diffractograms have VOIGT shape, so the discrepancy may not be attributed to the determination of the FWHM. On the contrary, note that for the whole process B, a determination of FWHM was possible only for the *c*-plane samples⁽¹¹⁾. In Fig. B.2, the ω -patterns of samples of all orientations from this process are depicted. The non-VOIGT shape for the orientations other than *c*-plane as well as the unexpectedly high ω -FWHM for *c*-plane sample indicate that the process yielded samples with poor crystal quality. The origin of this observation is not entirely clear, but for some samples of this batch, the stepper motor causing the substrate rotation

⁽¹¹⁾ This is why in Fig. 3.27, only the upper left *c*-plane tile has two data points at $F \approx 1 \text{ J cm}^{-2}$.

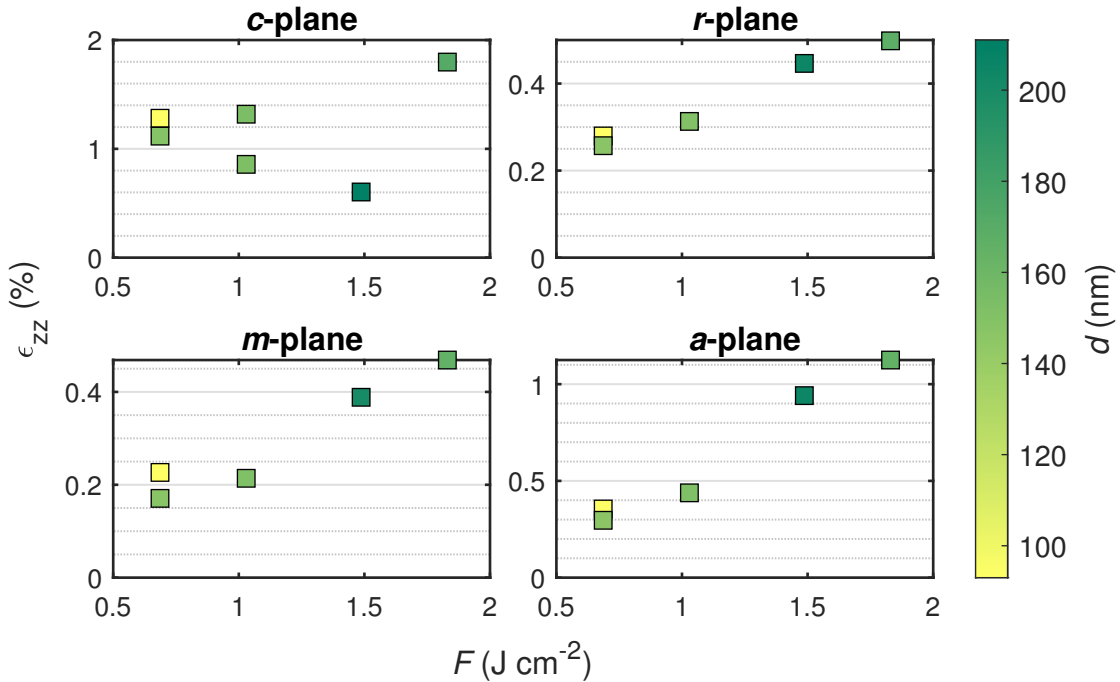


Figure 3.26: Out-of-plane strain calculated from $2\theta\text{-}\omega$ -patterns for all samples from the 2nd batch, depending on laser fluence and thickness (false color).

stopped during deposition, resulting in non-uniform deposition. Whether this was the case for process B is not sure, but since both A and B were conducted with the same process parameters⁽¹²⁾, something irregular must have been occurred.

r-plane: Laser Spot Size Variation

In Fig. 3.22, the o.o.p. strain for the *r*-plane samples fabricated with varying laser spot size is shown. The overall strain is with less than 1% lower when compared to the *c*-plane samples, exhibiting values up to 4% for thin samples. In particular, the predicted value for o.o.p. strain during pseudomorphic growth of Cr_2O_3 on Al_2O_3 of 2.41 % is not reached (cf. Tab. 1.3). As can be seen in a detailed view (Fig. B.5), the strain depends on the thickness: it decreases from 0.8 % to 0.5 % for an increment of thickness from 50 nm to 200 nm. This is in accordance to the behavior observed for the *c*-plane samples, albeit less pronounced. Furthermore, for a fixed thickness, decreasing the fluence also results in less strained thin films, which is similar to the behavior of the *c*-plane samples. The ω -FWHM obtained from the (02.4) reflection is depicted in Fig. 3.24. Similar to the *c*-plane samples – but less pronounced–, increasing the thickness results in less mosaicity, which is also achieved by reducing the fluence. Note that the overall ω -FWHM is between 50' and 90' which differs for the *c*-plane samples, where a lower fluence yielded samples with $\Delta\omega < 10'$ (cf. Fig. 3.24). Therefore, increasing the thickness and reducing the fluence by varying laser spot position may increase the crystal quality, but not to an amount comparable to *c*-plane oriented thin films.

⁽¹²⁾ The pulse number was varying, however, the growth rates $g_A = 3 \text{ pm pulse}^{-1}$ and $g_B = 3.75 \text{ pm pulse}^{-1}$ were quite similar.

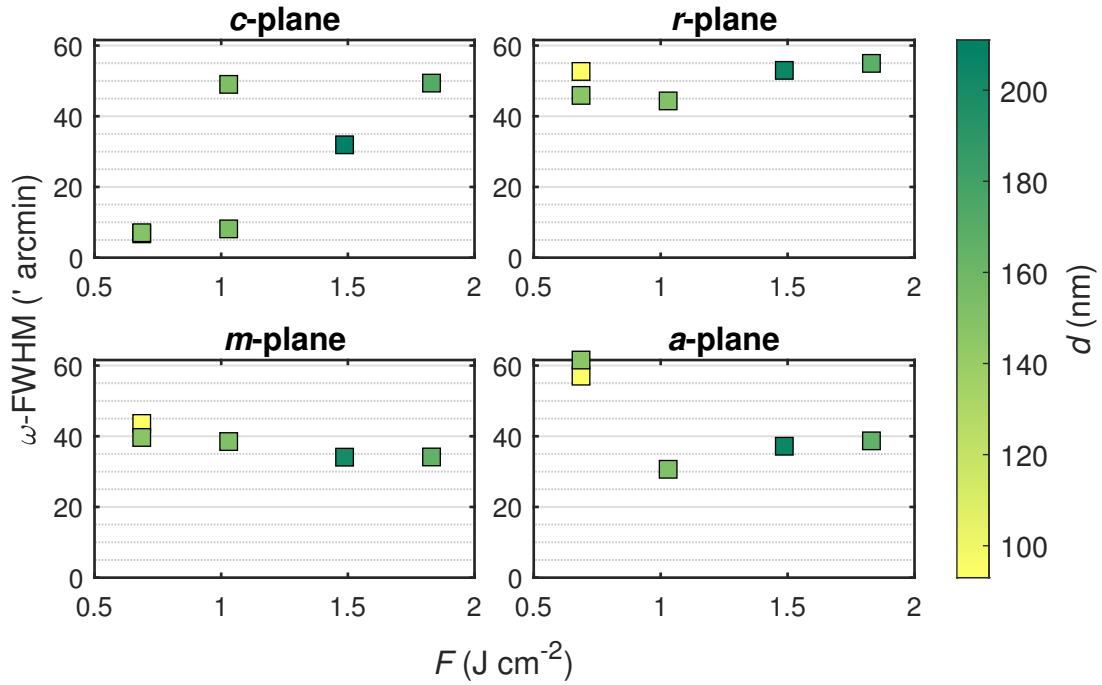


Figure 3.27: ω -FWHM for all samples from the 2nd batch, depending on laser fluence and thickness (false color). The corresponding diffractograms are depicted in Fig. B.4.

r-plane: Pulse Energy Variation

In Fig. 3.26, the o.o.p. strain is depicted for varying laser pulse energies (2nd batch). Independent of thickness, the fluence determines the strain of the thin films. The overall strain is below 0.4 %, and thereby comparable to the samples obtained from processes in the 1st batch with larger laser spot sizes. A detailed view on the strain for those samples is given in Fig. 3.28 which is based on the evaluation of RSMs that were performed as described in 3.3.1. The o.o.p. strain was calculated from both asymmetric (green triangle) and symmetric (yellow squares) reflections. The latter is equivalent to the calculation from the peak position in 2θ - ω diffraction patterns. It can be observed that the increasing tensile o.o.p. strain comes along with an increasing i.p. compressive strain, ranging from -0.2% to -0.8% . Therefore, the o.o.p. strain may be attributed to a partial pseudomorphic growth mode, because the Al_2O_3 lattice constants are smaller than the ones for Cr_2O_3 . The compressive strain is then due to an aligning of in-plane lattice constants. Note that the values for o.o.p. strain obtained from 2θ - ω -scans (cf. Fig. 3.26) are only partially confirmed: the strain measured from the symmetric RSM is approx. 0.2 percentage points below the value obtained from 2θ - ω -scans. The origin of this discrepancy may lay in the correction that was applied to the RSMs. However, the correction of the substrate peak position in 2D reciprocal space corresponds to a shift of the whole 1D 2θ - ω pattern to match the substrate peak. The latter was done for the evaluation of 2θ - ω -scans on which Fig. 3.26 is based. But the correction of thin film tilt which is done for RSMs was not done for the 2θ - ω -scans: The ω -optimization prior to a 2θ - ω -scan is for correcting a tilt of the whole sample, because 2θ is fixed to the value expected for the (02.4) reflection of Al_2O_3 . This does not account for a possible thin film tilt with respect to the substrate. Note that a correction of thin film tilt is not possible for 2θ - ω -scans, because the information on thin film tilt is not provided by

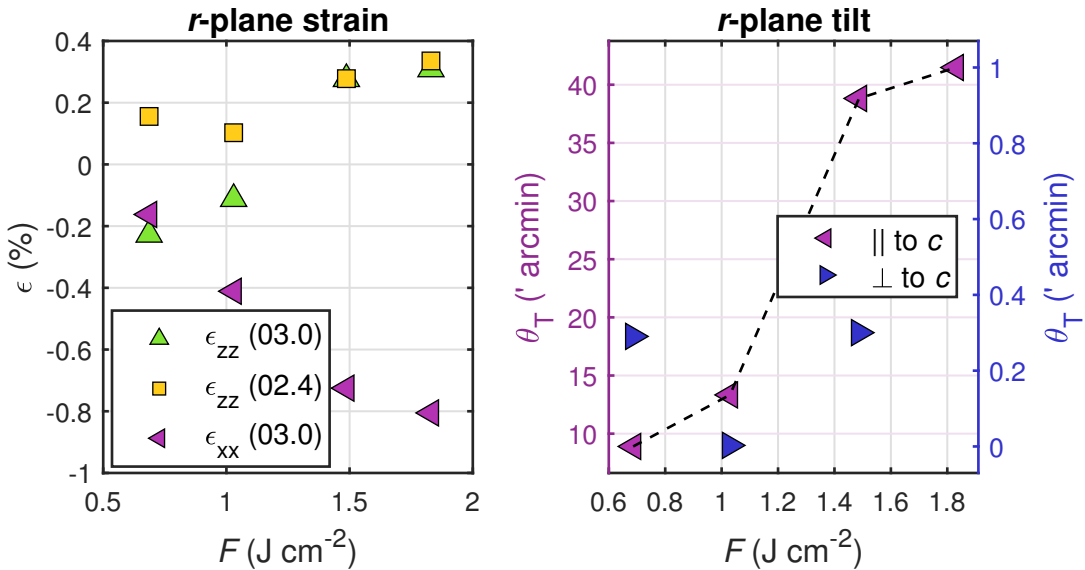


Figure 3.28: In-plane and out-of-plane strain for the r -plane samples from the 2nd batch, calculated from the peak positions of the RSMs described in 3.3.1 (left). Tilt along the x -axis (purple ordinate) and y -axis (blue ordinate), determined from symmetric reflections (right). Note the different scaling of the ordinates, indicating less tilt along the y -axis.

a 2ϑ - ω -pattern. But even though this is a significant difference in evaluation between 2ϑ - ω -patterns and RSMs, the discrepancy between both methods is still present even for small thin film tilts below $10'$. So further analysis has to be done for the applied evaluation methods. But in general it has to be noted that the precision of the o.o.p. strain obtained from RSMs depends on (i) the peak position of the reflection, (ii) the peak position of the corresponding substrate peak (for substrate correction) and (iii) the peak position of the asymmetric peaks (for shear correction, not done for r -plane). Those positions were not obtained by fitting a 2D VOIGT profile to the RSMs, but by reading the peak position “by hand”. This may result in an undefined error.

Another observation is that the o.o.p. strain obtained from symmetric (yellow squares) and asymmetric reflections (green triangles) aligns for the two samples fabricated with higher fluences only (cf. Fig. 3.28). The discrepancy observed for the lower fluences is physically implausible and is probably due to an error in evaluation. This is supported by the fact that for those two data points, the strain obtained from asymmetric reflections is almost exactly mirroring the value obtained from the symmetric reflections. This also confirms the previously stated hypothesis that the evaluation of either RSM or 2ϑ - ω -pattern exhibits a systematic error.

As predicted by Grundmann and Lorenz (2020) [67], partially relaxed r -plane thin films with certain values for the elastic tensor should exhibit a tilt of the thin film with respect to the substrate. This tilt is indeed observed along the x -axis for all values of fluence, ranging from approx. $10'$ to $40'$ (purple triangles in Fig. 3.28). A corresponding tilt along the y -axis is not observed: there, the tilt angles are two orders of magnitude lower and below $0.4'$. This is in agreement with elasticity theory which predicts a tilt only along the x -axis, because the prismatic slip systems responsible for relaxation along the y -axis yield tilt components of the BURGER's vector that cancel out on average (cf. 1.3.2). But note that the thin film tilt increases for higher fluences, which also results

in a higher o.o.p. strain. This observation is somehow curious, because the thin film tilt is a result of *relaxation*, whereas strain is a result of partial *pseudomorphic* growth. So according to strain, higher fluences result in less relaxed layers – according to tilt, higher fluences result in more relaxed layers. This result indicates that an interplay of both processes is present and that for growth modes that exhibit no complete pseudomorphic behavior, more sophisticated models for the relaxation mechanism must be applied.

The ω -FWHM of the *r*-plane samples of the 2nd batch is approx. $50'$ and has no significant dependence on both fluence or thickness (Fig. 3.27). This confirms the previously obtained result for the samples fabricated with varying laser spot sizes.

***m*- and *a*-plane: Laser Spot Size Variation**

In Fig. 3.22, the o.o.p. strain for the *m*- and *a*-plane oriented samples of the 1st batch (laser spot size variation) is depicted. The maximum strain which is reached for high fluences is approx. 0.8% and 1.5% for *m*- and *a*-plane, respectively. Those values are far below the predicted values for pseudomorphic growth, which are 3.67% (*m*-plane) and 3.63% (*a*-plane). This indicates relaxed growth. In Fig. B.5 it can be seen that for higher thicknesses, the strain reduces only very slightly. The *m*-plane outlier to this behavior can be explained by the very low peak intensity of the (30.0) reflection in the 2θ - ω pattern, which causes a larger uncertainty for this value. Overall, the fluence is the determining parameter for the strain, allowing strain values of down to 0% for *a*-plane samples.

In Fig. 3.24, the ω -FWHM for both *m*- and *a*-plane samples is depicted. For *m*-plane, the ω -FWHM is approx. $50'$ for all fluences and thicknesses – only a small decrease for higher thicknesses is observed⁽¹³⁾. However, for *a*-plane no significant dependence on fluence can be observed. On the contrary, there seems to be an increase in ω -FWHM for increasing thicknesses up to approx. 100 nm. This behavior differs from all other orientations observed and could be attributed to an unusual shape of the ω -patterns. In Fig. 3.29, such a pattern is depicted and has clearly no VOIGT-shape. Rather, the pattern consists of an exponential slope (linear in logarithmic intensity axis) for about 1.5° and a very sharp 2nd peak with a small FWHM on top of it. This shape is observed for almost every *a*-plane sample, as can be seen by the various diffractograms shown in Fig. B.3. The 2nd peak is located at the maximum of the underlying broader peak and can therefore not be attributed to Al_2O_3 or another phase of Cr_2O_3 , because then it would not shift together with the (22.0) peak of the α -phase of Cr_2O_3 . This is also supported by the fact that no anomaly is observed in the 2θ - ω -patterns (not shown). A physical interpretation of the shape is a distinct Cr_2O_3 layer of increased crystallinity at the interface between Al_2O_3 and Cr_2O_3 . In Fig. 3.29b, several ω -patterns are depicted for thin films of different thickness, where the counts are visualized linearly on the ordinate. For very thin films, only the sharp peak is observable, indicating the formation of a crystalline layer of $t \approx 30$ nm. For increasing film thicknesses, the 2nd peak remains at a rather low intensity, while the broader peak increases in intensity. This may indicate that on top of the already grown

⁽¹³⁾ As a result, in Fig. 3.25, two regimes of high and low fluence can be distinguished, where each regime itself comes with a correlation indicating better crystallinity with less strain. However, altogether, a slight negative correlation can be observed, i.e. better crystallinity comes at the cost of higher strain.

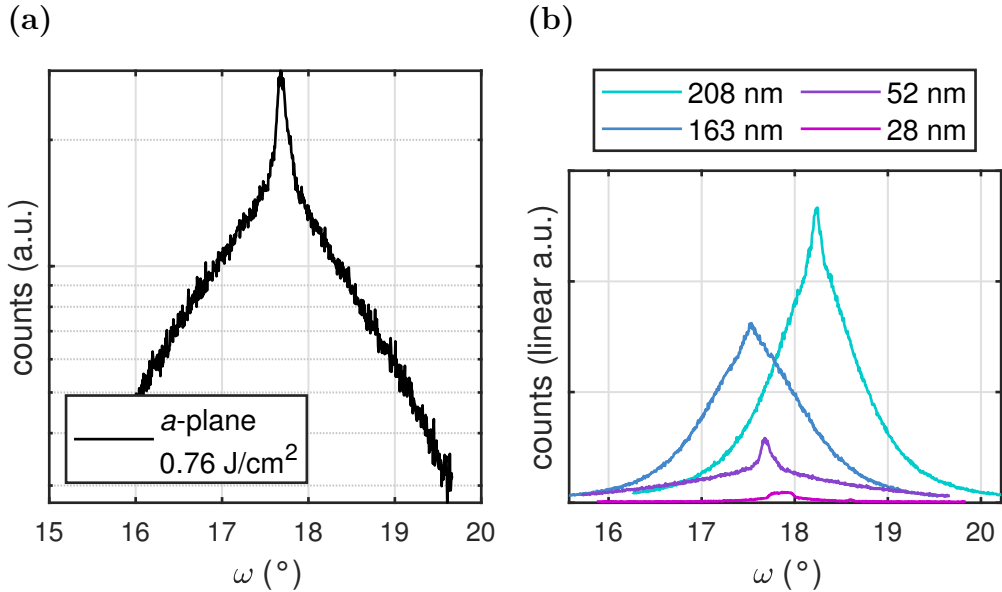


Figure 3.29: ω -pattern of *a*-plane samples from the 1st batch: (a) a sample with logarithmic representation and (a) samples with varying thickness in linear representation.

highly crystalline layer, another layer with higher mosaicity is growing. Note that the diffractograms stem from different samples, which were also fabricated with different laser fluences, which makes the comparison difficult and the origin of the 2nd peak not entirely clear. However, this may explain the broad spread of ω -FWHM (15' to 80') for *a*-plane samples as well as that the ω -FWHM follows a different relation to fluence and thickness when compared to the other orientations.

m- and *a*-plane: Pulse Energy Variation

In Fig. 3.26, the o.o.p. strain for the *m*- and *a*-plane oriented samples of the 1st batch is depicted. The strain ranges from 0.15 % (0.3 %) to 0.45 % (1.1 %) for *m*-plane (*a*-plane) samples. A clear dependence on fluence can be observed, whereby the thickness has no influence at all. The complete in- and out-of-plane strains for *m*-plane samples are depicted in Fig. 3.30a. With increasing o.o.p. strain, the i.p. strain also increases, which indicates a pseudomorphic growth mode. Note that the i.p. strain is, in the range of uncertainty, the same along both *x*- and *y*-direction, even though both axes are not equivalent. As for *r*-plane samples (cf. Fig. 3.28), the o.o.p. strain is systematically smaller by 0.15 percentage points, compared to the values obtained from peak positions in 2θ - ω -patterns (Fig. 3.26). 2θ - ω -scans probe for symmetric reflections only, which is why shear stresses cannot be corrected by this method. However, those strain angles are rather small (cf. Fig. 3.30a), which is why it is unplausible that this is the origin of the discrepancy. Moreover, as discussed for the *r*-plane samples, the thin film tilt is suspected to be too small to yield this effect.

As predicted by Kneiß *et al.* (2021) [64], a significant tilt of the thin film is observed along the *x*-direction (purple triangles in Fig. 3.30a), which ranges from 20' to 40' and increases with higher fluences. Furthermore, a small shear of up to 2' is observed along this axis. On the contrary, a thin film tilt (blue triangles) below 1' and a small shear tilt are observed in *y*-direction. This is also in accordance with the predicted slip systems

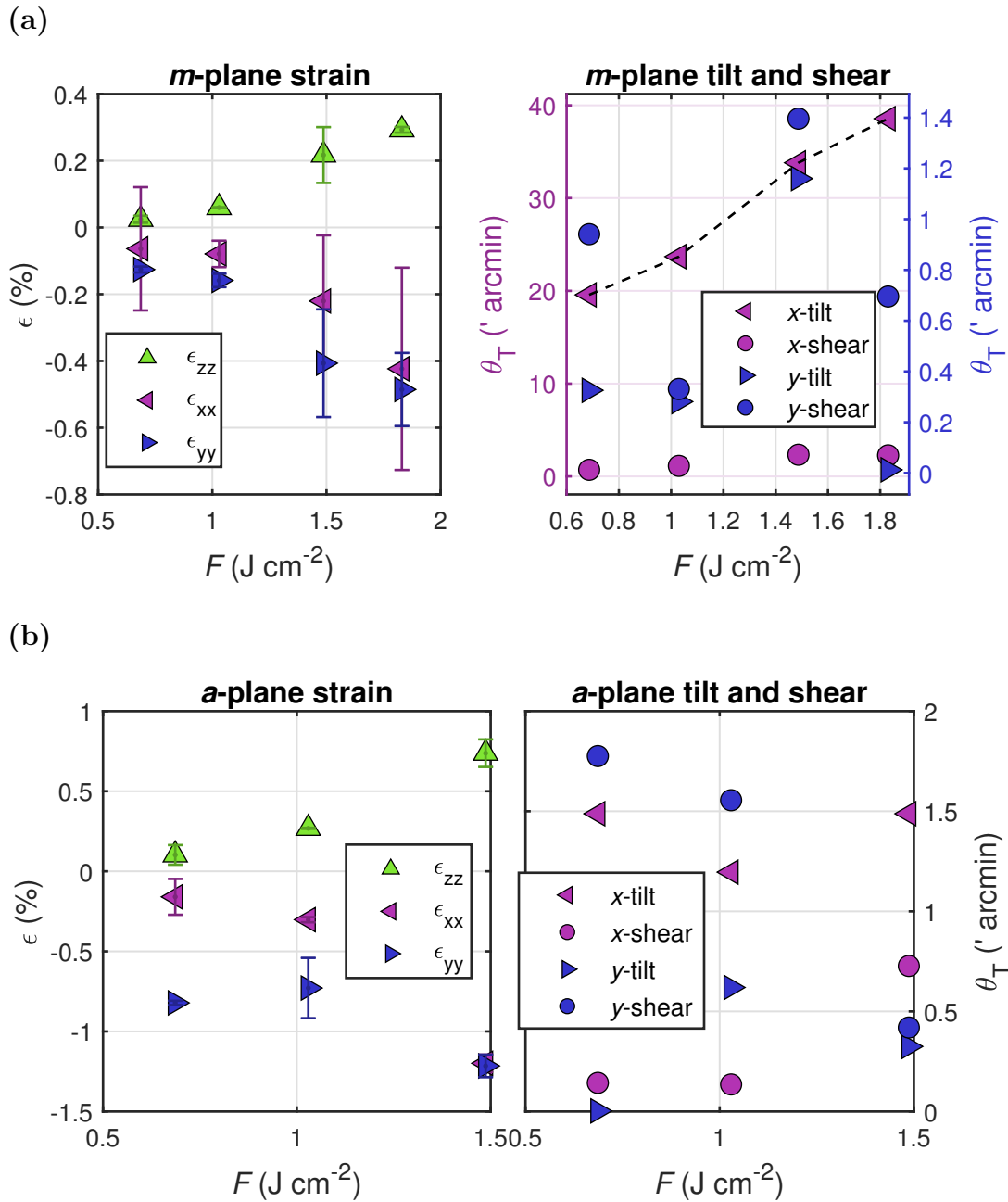


Figure 3.30: Left: In-plane (along x - and y -axis) and out-of-plane strain for the (a) m -oriented and (b) a -oriented samples from the 2nd batch, calculated from the peak positions of the RSMs described in 3.3.1. Right: Shear (circles) and tilt (triangles) of thin films determined by asymmetric and symmetric reflections, respectively. The values were determined along x -axis and y -axis. This is represented by the purple and blue ordinates in (a), respectively. Note the different scaling of the ordinates, indicating less tilt along the y -axis. Due to the same scale of tilt along x - and y -axis for (b), only one ordinate is used to represent the data.

Table 3.3: measurement results for two selected *m*-plane oriented Cr₂O₃ thin films that were investigated via AFM.

Id	thickness <i>t</i>	fluence <i>F</i>	strain ϵ_{zz}	ω -FWHM	RMS roughness
L.02	89 nm	1.05 J cm ⁻²	0.32 %	38.1'	2.5 nm
L.05	79 nm	2.06 J cm ⁻²	0.9 %	44.4'	1.9 nm

(cf. 1.3.2), which should result in no net tilt along the *y*-axis. However, as it is the case for the *r*-oriented samples, this thin film tilt – acting as an indicator for relaxation – increases with higher fluences. But this objects to the observation of decreasing relaxation with higher fluences due to increasing i.p. and o.o.p. strain. Again, this draws to the conclusion that a more sophisticated description of partially relaxed layers is in need.

In a qualitative sense, a similar behavior for *a*-plane samples is observed when investigating both in- and out-of-plane strain (Fig. 3.30b). However, the i.p. strain is significantly larger along the *y*-direction for layers with less strain: for *F* = 0.7 J cm⁻², the thin film is 0.66 percentage points more strained along the *y*-axis. This discrepancy reduces for thin films that are more stressed in total. Furthermore, as for the other orientations, the o.o.p. strain is systematically lower when compared to the values obtained from 2θ- ω -patterns, namely by 0.15 percentage points. The reasons for this effect are presumably the same as for the *m*-plane oriented samples. The shear and tilt angles for *a*-plane samples are depicted in Fig. 3.30b. As predicted by Kneiß *et al.* (2021) [64], no tilt is observed along both the *x*-axis (< 1.5') and *y*-axis (< 0.7'). A small shear angle of around 1.5' is observed along the *y*-axis.

Finally, the mosaicity for both *m*- and *a*-plane samples is depicted in Fig. 3.27. For *m*-plane oriented samples, the ω -FWHM is approx. 40' and decreases slightly with higher fluences, which is in contrast to the increasing strain. For *a*-plane samples, a large spread similar to the samples of the 1st batch (cf. Fig. 3.24) is observed. But, again, this observation is probably due to the specific shape of ω -patterns for the *a*-plane samples. In Fig. B.4, the diffractograms are depicted and a severe deviation from the VOIGT shape can be identified. Therefore, determination of the FWHM is hindered and the large spread of values explained.

For two selected samples, AFM measurements were performed and the height profiles are displayed as false color images in Fig. 3.31. The sample L.02 (Fig. 3.31a,b) was fabricated with a larger laser spot size compared to the sample L.05 (Fig. 3.31c,d). The Root Mean Square (RMS) roughness for each sample was determined from the height profiles of a 2 × 2 μm² and 5 × 5 μm² probed area. These values as well as other details are listed in Tab. 3.3. In general, the surface morphology is comparable to the results obtained before for α-Ga₂O₃ thin films fabricated by PLD, where RMS roughnesses of 0.6 to 3.5 nm were achieved for different growth temperatures [45]. In contrary to the previous results – where smaller laser spot sizes lowered crystal quality –, the sample fabricated with higher fluence L.05 exhibits a better thin film quality regarding RMS roughness. However, this sample exhibits several stripes on the surface (cf. Fig. 3.31d). They are presumably not a measurement artifact, because they remained during repeated scans of the surface (not shown). Therefore, although having slightly larger RMS roughness, the fabrication with larger laser spot size (L.02) yields more

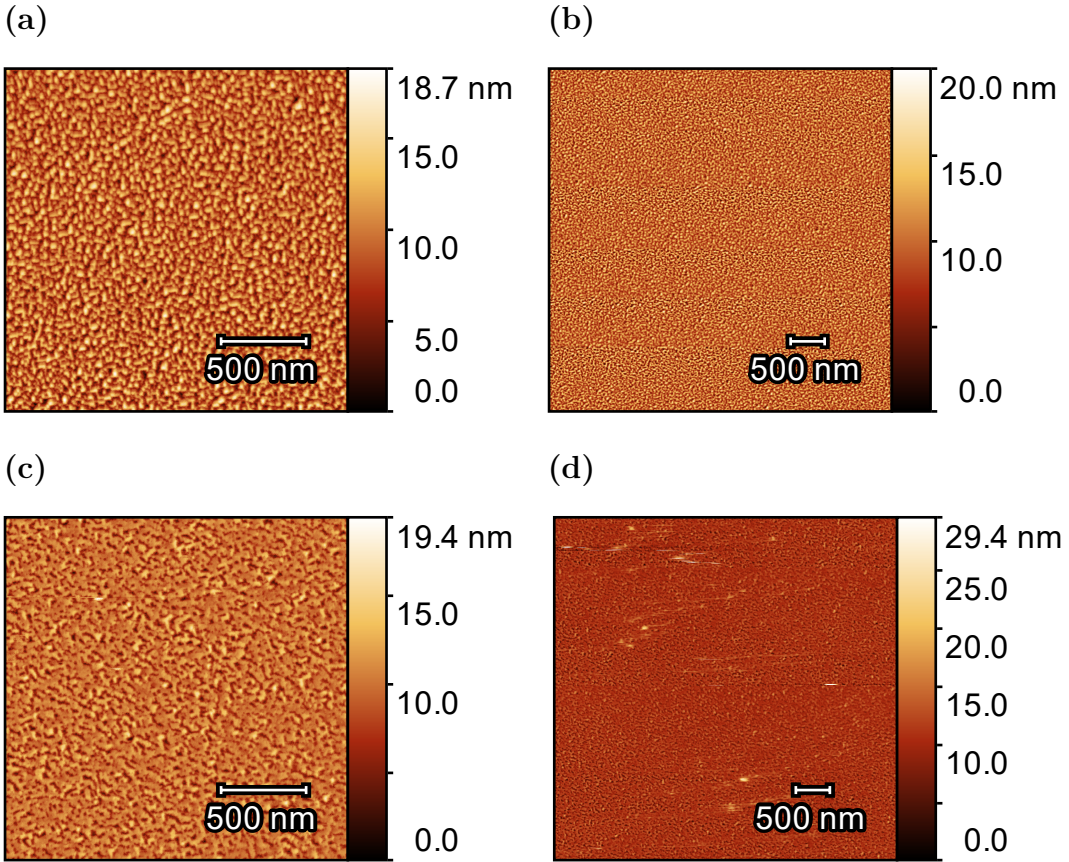


Figure 3.31: AFM false color images of (a, b) sample L.02 and (c, d) sample L.05. The probed areas are $2 \times 2 \mu\text{m}^2$ and $5 \times 5 \mu\text{m}^2$ for the left and right panels, respectively.

homogeneous surfaces.

In Fig. 3.32, the transmission spectra of selected *m*-plane oriented samples from the 1st batch are depicted. The fluence does not seem to have a significant influence, however, the thickness is decisive for the shape of the absorption edge. The onset of absorption E_{opt} is approx. 3.5 eV for all samples of different thickness and fluence. This is in accordance with the value obtained for the samples of the initial Cr_2O_3 batch (cf. 3.1 and Fig. 3.5b).

3.3.3 Conclusion

The out-of-plane strain and in-plane strain of Cr_2O_3 thin films of different crystal orientation were investigated depending on the laser fluence on the target during deposition via PLD. Samples with *c*-orientation grow fully pseudomorphic for low film thicknesses, whereas the samples of different orientation only show partial pseudomorphic growth. The thickness is for *c*- and *r*-plane samples a crucial parameter, whereas the laser fluence on the target strongly influences the crystal structure of *m*- and *a*-plane samples. This indicates that the thickness of the thin films is more relevant for orientations that have more out-of-plane *c*-axis component, because for the prismatic orientations, the *c*-axis is completely in-plane. Overall, less laser fluences – no matter whether via larger laser spot sizes or reduced laser pulse energy – result in less FWHM in ω -patterns. For

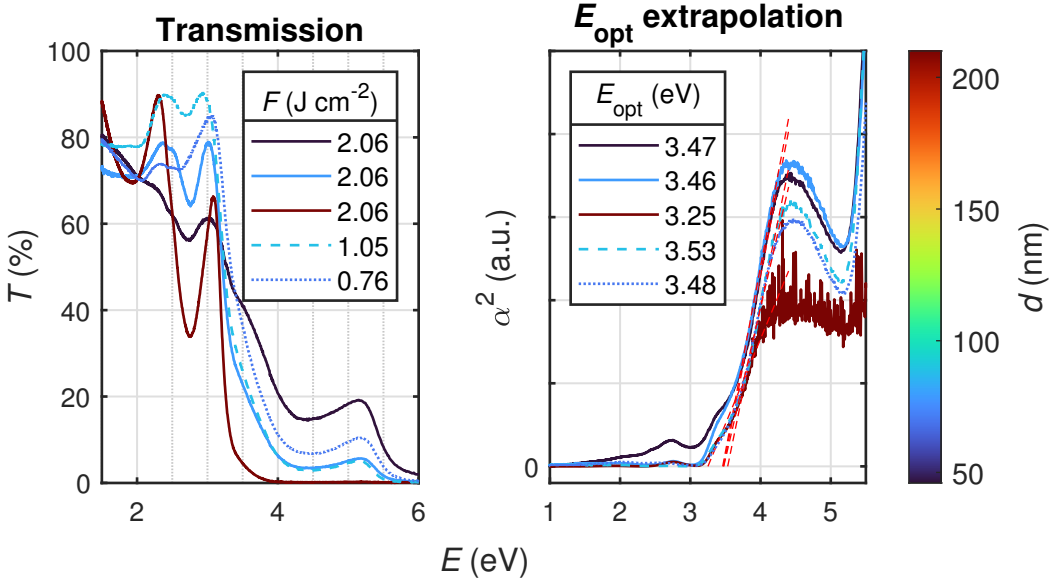


Figure 3.32: Transmission spectra (left) of selected m -plane oriented samples from the 1st batch. The samples differed in thickness and laser fluence on the target surface, achieved by varying lens positions. The α^2 vs. E plot (right) of the mentioned samples, determined by assuming a direct band gap of Cr_2O_3 (cf. 2.3.4 and 3.1).

r -, m - and a -plane oriented samples, thin film tilts has been observed in the directions that were predicted by theoretical calculations [64, 67] (cf. Tab. 1.3b).

In Kneiß *et al.* (2021) [64], a relaxation parameter ρ_x was successfully introduced to quantify the amount of partial relaxation along the x -axis for m - and a -plane oriented α -(Al _{x} Ga_{1- x})₂O₃ thin films. Higher values of ρ_x correspond to more pseudomorphic growth and were correlated to smaller tilt angles. However, the results for Cr₂O₃ object to this observation: an increasing thin film tilt is correlated to an *increasing* in- and out-of-plane strain (cf. Fig. 3.30), i.e. to more pseudomorphic growth. The explanation of the thin film tilt by the relaxation model does not seem to be the origin of this false prediction: The axis of thin film tilt was correctly predicted to be only along x -direction for m - and r -plane thin films and along no direction at all for a -plane samples! Nevertheless, the result of this observation is that no trade-off has to be made between strain and thin film tilt – a lens position of -1 cm and laser pulse energy of 450 mJ yields almost no strain and low thin film tilt while still resulting in a growth rate of up to 4 pm pulse⁻¹.

3.4 Cr₂O₃ Buffer Layers for α -Ga₂O₃

A major motivation for investigating Cr₂O₃ thin films is due to a possible usage as buffer layer for α -Ga₂O₃, which has similar lattice parameters. This could improve the crystal quality of the latter due to reduced lattice mismatch when compared to Al₂O₃ [9]. From Fig. 3.33 it becomes clear that Cr₂O₃ has a larger *c* lattice constant, but a smaller *a* lattice constant than α -Ga₂O₃. Therefore, e.g., the in-plane compressive strain observed for *c*-plane Cr₂O₃ thin films actually further decreases the mismatch between Cr₂O₃ and α -Ga₂O₃. For *m*-plane samples, however, the in-plane compressive strain yields a larger discrepancy between the *a* lattice constant of both sesquioxides. In the following, a proof of concept will be given that α -Ga₂O₃ can successfully be deposited on Cr₂O₃ buffer layers.

3.4.1 Experiment

For the Cr₂O₃ thin films, deposition parameters were chosen that yielded the lowest strain and ω -FWHM. Therefore, a lens position of -1 cm and a laser pulse energy of 450 mJ were applied. Note that 350 mJ would result in even better crystallinity, but only at the cost of very low growth rates. The Ga₂O₃ layer was deposited with a lens position of -1 cm and a laser pulse energy of 650 mJ . This is the configuration that was used for depositing Cr₂O₃ in 3.1 and 3.2. By assuming a growth rate of 10 pm pulse^{-1} – which is achieved for deposition with similar parameters at a different PLD chamber –, $15\,000$ pulses were applied to achieve a layer thickness of 150 nm . The oxygen partial pressure was $3 \times 10^{-4}\text{ mbar}$ and the temperature was chosen to be approx. ??. Two approaches were chosen to deposit α -Ga₂O₃ of four different orientations *c*, *r*, *m* and *a*:

1. Deposition of Cr₂O₃ with subsequent *ex situ* analysis of the Cr₂O₃ layer under atmospheric conditions. Afterwards the Ga₂O₃ layer was deposited in a distinct PLD process.
2. *In situ* deposition of Cr₂O₃ and Ga₂O₃ without returning to atmospheric conditions inbetween. Between both processes, the oxygen pressure was reduced and it was waited for 20 min to achieve thermodynamic equilibrium.

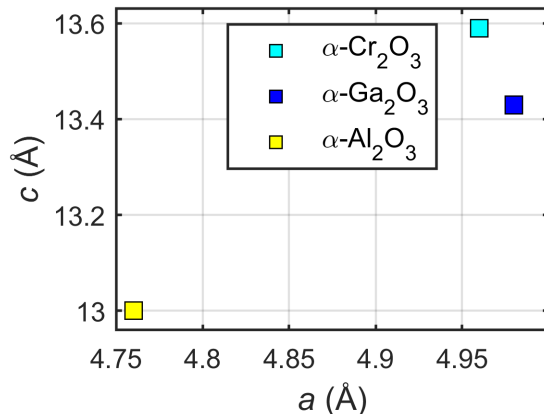


Figure 3.33: Lattice constants *a* and *c* for the three sesquioxides relevant in this work.

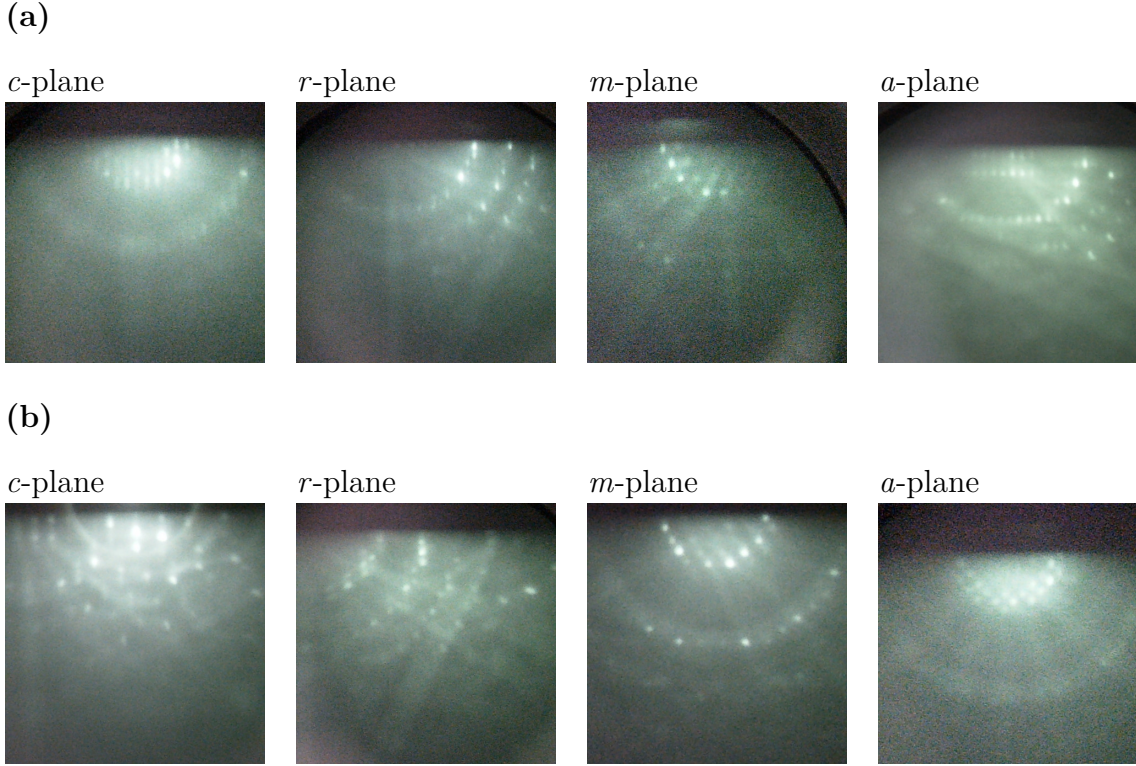


Figure 3.34: RHEED patterns of the $\alpha\text{-Ga}_2\text{O}_3$ surface deposited (a) *ex situ* on Cr_2O_3 and (b) *in situ* on Cr_2O_3 . Note that the patterns were recorded in arbitrary azimuth which is why they may differ between *ex situ* and *in situ* deposition. This is not necessarily a result of different crystal structure.

For the *ex situ* samples, RSMs were recorded before and after the deposition of the Ga_2O_3 layer. For all samples, 2θ - ω -scans were performed in the range of 10 to 130° after deposition of the Ga_2O_3 layer. Furthermore, Reflection High-Energy Electron Diffraction (RHEED) patterns were recorded for the surfaces of all samples after deposition of the Ga_2O_3 layer. RHEED is a method to probe the crystal structure of only a few monolayers below the surface of a thin film. High-energy electrons are pointed in grazing incidence geometry on the sample surface and the diffracted electrons are detected with a fluorescent screen. The image of the screen is called the RHEED pattern and it can yield information about the symmetry and crystallinity of the sample surface [78].

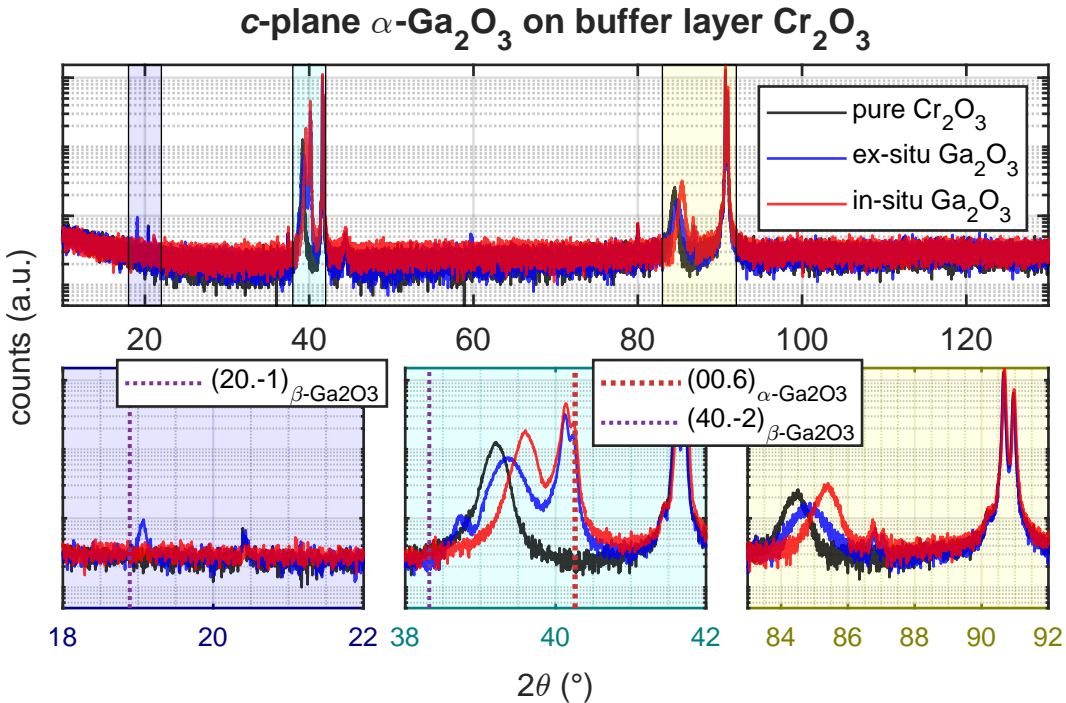
The 2θ - ω patterns are compared to a reference Cr_2O_3 sample, namely sample A from 3.3, which was also fabricated with a pulse energy of 450 mJ. The theoretical predictions of the 2θ values for reflections of $\beta\text{-Ga}_2\text{O}_3$ were taken from the *Materials Project* [79, mp-886].

3.4.2 Results

The RHEED patterns of all samples from the *ex situ* and *in situ* batch are depicted in Fig. 3.34a and Fig. 3.34b, respectively. From the periodic patterns it can be concluded that every surface is crystalline. Note that the mere observation of crystallinity does not indicate which phase of Ga_2O_3 is present on the samples.

In Fig. 3.35a, 2θ - ω patterns are depicted of the Cr_2O_3 reference sample A (black), as

(a)



(b)

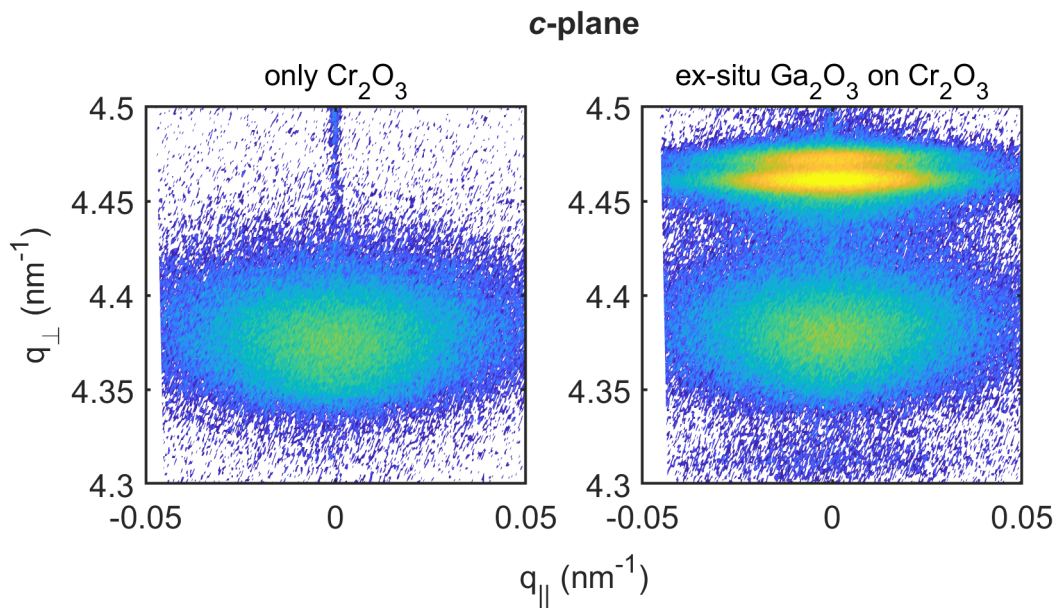


Figure 3.35: (a) $2\theta\text{-}\omega$ -patterns of the *c*-plane Cr_2O_3 reference sample A (black), as well as the *ex situ* (blue) and *in situ* (red) buffer layer structures. (b) RSM around the (00.6) reflection recorded before (left) and after (right) *ex situ* deposition of Ga_2O_3 .

Table 3.4: Selected reflections of $\beta\text{-}\text{Ga}_2\text{O}_3$ and their predicted positions in $2\theta\text{-}\omega$ patterns as well as their relative intensities. Data taken from Ref. [79, mp-886]

2θ	reflection	relative intensity
18.89°	(20̄1)	8.7
38.3°	(31̄1)	57.0
38.32°	(40̄2)	3.6
38.36°	(202)	2.5

well as of the *ex situ* (blue) and *in situ* (red) samples. The peak at around 39.2° of the reference sample is the (00.6) reflection of Cr_2O_3 . This reflection is also attributed to the peaks at approx. 39.4° and 39.6° of the *ex situ* and *in situ* samples, respectively. The variation of peak position for the Cr_2O_3 layer may originate in the fact that for each process, the thickness may have varied which was determined to be a crucial factor for the out-of-plane strain. Despite this peak, two overlaying peaks occur at 40.14° for both buffer layer processes. This is attributed to the (00.6) reflection of $\alpha\text{-}\text{Ga}_2\text{O}_3$, because the predicted peak position is at 40.26° with a relative intensity⁽¹⁴⁾ of 3.37, and is therefore allowed. The presence of two peaks is attributed to the splitting between Cu-K α_1 and Cu-K α_2 radiation (*K α splitting*). Note that at approx. 86°, the higher order (00.12) reflection of Cr_2O_3 can be observed more dominantly than the (00.12) reflection of $\alpha\text{-}\text{Ga}_2\text{O}_3$. This is due to the fact the the ratio of relative intensities of (00.12) to (00.6) is 29.6 % for Cr_2O_3 and only 1.4 % for $\alpha\text{-}\text{Ga}_2\text{O}_3$.

For the *in situ* sample, no additional peaks are observed, indicating phase-pure deposition of *c*-plane Ga_2O_3 in the α -phase on *c*-plane Al_2O_3 . For the *ex situ* sample, however, a peak occurs at 38.71° and the β -phase of Ga_2O_3 has three different predicted peaks at this position, listed in Tab. 3.4. The observed peak is attributed to the (40̄2) reflection, because at 19.06°, another peak is observed that can only correspond to the (20̄1) reflection of $\beta\text{-}\text{Ga}_2\text{O}_3$ (Tab. 3.4), which favors the identification of (40̄2) as a higher order reflection. Note that the peak observed at 20.4° is also observed for the Cr_2O_3 reference sample and can therefore not correspond to any Ga_2O_3 phase.

In Fig. 3.35b, the RSMs of the *ex situ* sample are displayed. Note that the image is cropped such that no substrate peak is visible. The previous result is confirmed that another phase has formed on top of the Cr_2O_3 layer. No ω -scans were done, but the crystallinity can be estimated by the broadening in q_{\parallel} direction, which is less dominant in comparison to the Cr_2O_3 layer. Furthermore, the $\text{K}\alpha$ splitting indicates a highly crystalline thin film.

The $2\theta\text{-}\omega$ patterns of the *r*-plane reference and buffer layer samples are depicted in Fig. 3.36a. Due to very close peak positions of the (02.4) reflection for both Cr_2O_3 and $\alpha\text{-}\text{Ga}_2\text{O}_3$, a comparison with the reference sample is not as straightforward as for the other orientations. No additional peak can be identified for the buffer layer samples. However, the RHEED patterns indicated a crystalline surface, which is why the only possible phase of the Ga_2O_3 layer is the α -phase. This is verified by RSMs of the *ex situ* sample in Fig. 3.36b: a significant increment in intensity can be observed at the

⁽¹⁴⁾ This value indicates the peak intensity of a reflection in powder diffraction patterns and gives a hint to identify peaks.

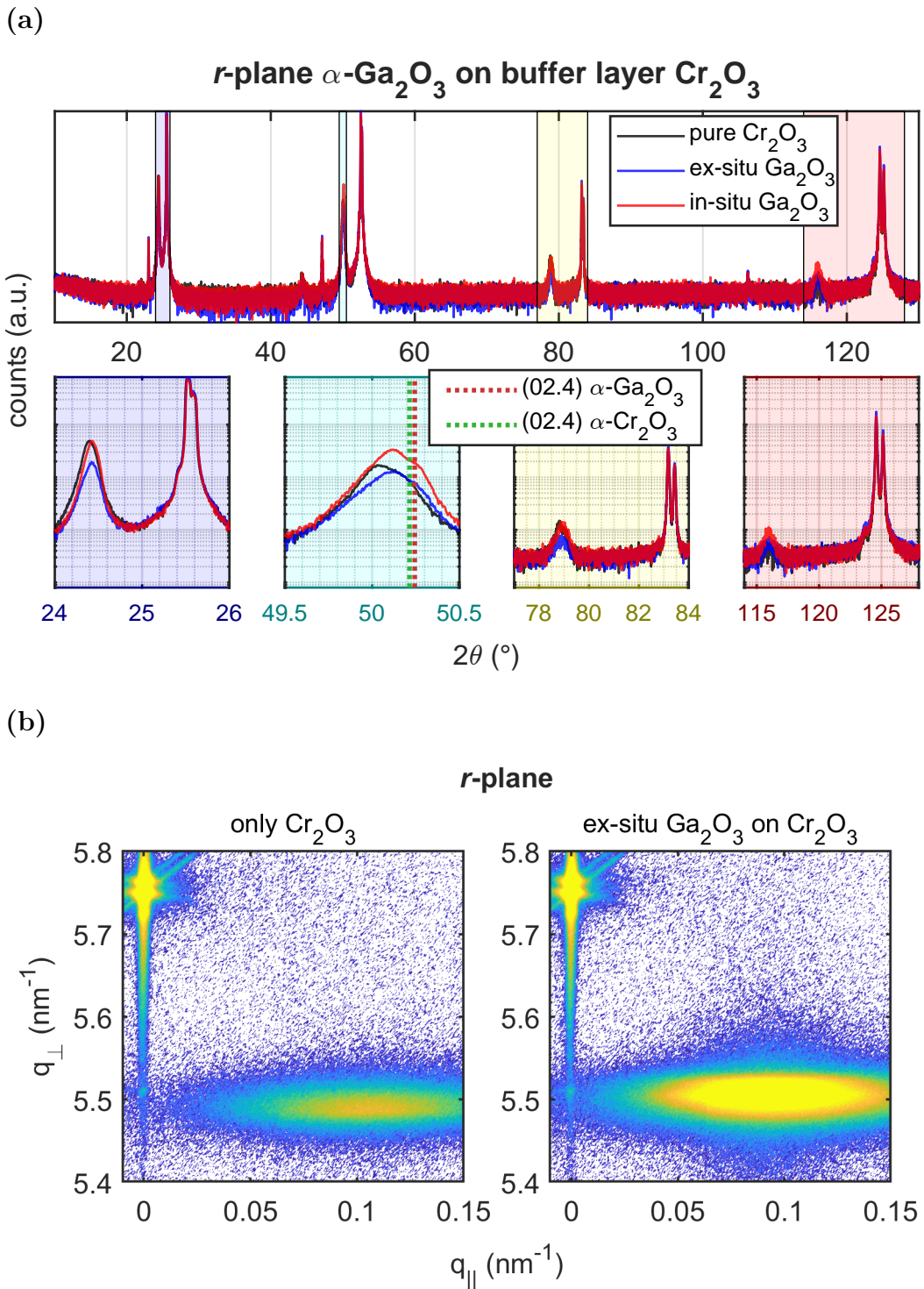


Figure 3.36: (a) 2θ - ω -patterns of the *r*-plane Cr_2O_3 reference sample A (black), as well as the *ex situ* (blue) and *in situ* (red) buffer layer structures. (b) RSM around the (02.4) reflection recorded before (left) and after (right) *ex situ* deposition of Ga_2O_3 .

expected peak position of (02.4) $\alpha\text{-Ga}_2\text{O}_3$, which is due to the formation of α -phase Ga_2O_3 on r -plane Cr_2O_3 .

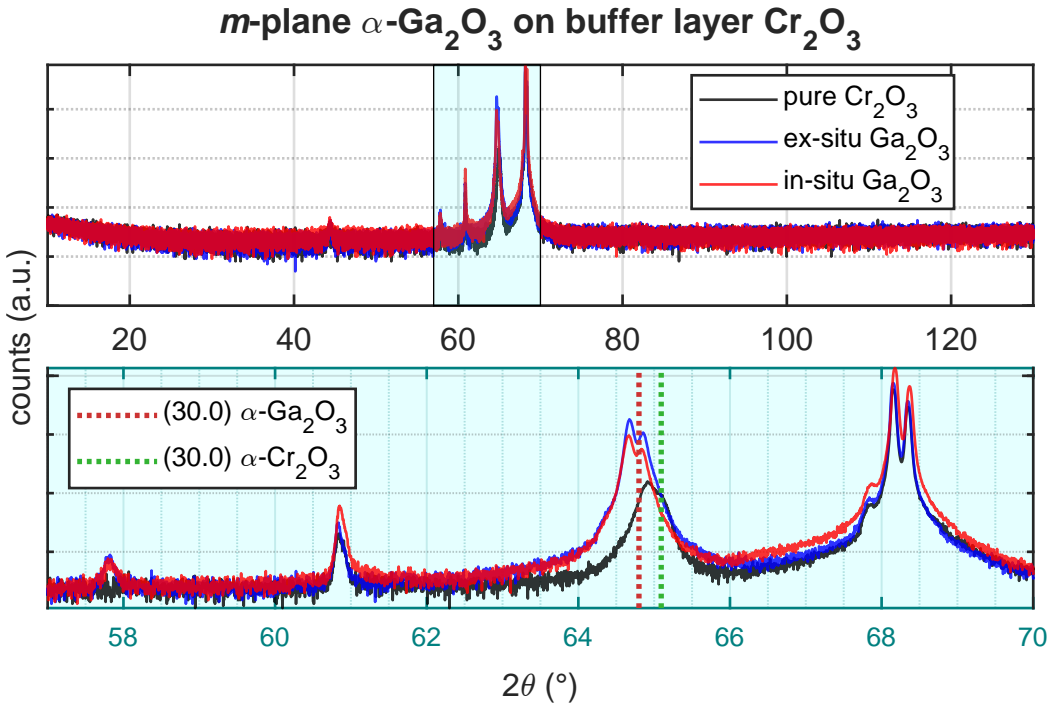
When comparing the peaks of m -plane buffer layer samples to the Cr_2O_3 reference sample, note that the (30.0) peak is shifted to lower angles (Fig. 3.37a). Furthermore, two peaks can be observed for the buffer layer samples, which may originate in (i) either two peaks for Cr_2O_3 and $\alpha\text{-Ga}_2\text{O}_3$ each; or (ii) $\text{K}\alpha$ splitting of a (30.0) $\alpha\text{-Ga}_2\text{O}_3$ reflection on top of the Cr_2O_3 layer. Both explanations are favored by the fact that the expected peak position (red dotted line) lays inbetween both peaks. The theoretical predictions of the 2θ positions also have similar distance as the two peaks observed (red and green dotted lines), favoring the first explanation. However, when considering Fig. 3.37b, it becomes clear that the origin is a $\text{K}\alpha$ splitting, because prior to the deposition of Ga_2O_3 , none of the peaks was present with the observed intensity. Therefore, the observed peaks must both stem from the α -phase of Ga_2O_3 . No other peaks are observed in the $2\theta\text{-}\omega$ pattern, therefore a phase pure α -phase is present.

A similar behavior as for the m -plane samples can be observed in the $2\theta\text{-}\omega$ patterns of a -plane samples (Fig. 3.38)a. The splitted peak is attributed to the (22.0) reflection of an $\alpha\text{-Ga}_2\text{O}_3$ layer and the peak on the left shoulder to the (22.0) reflection of Cr_2O_3 , which is shifted to lower angles in comparison to the reference sample. This behavior is also observed for the (11.0) reflections of both $\alpha\text{-Ga}_2\text{O}_3$ and Cr_2O_3 . This result is confirmed by the RSMs (Fig. 3.38b), where two peaks appear due to $\text{K}\alpha$ splitting after Ga_2O_3 deposition. The low broadening in q_{\parallel} direction as well as the $\text{K}\alpha$ splitting indicate good crystal quality.

3.4.3 Conclusion

Phase-pure depositon of $\alpha\text{-Ga}_2\text{O}_3$ on Cr_2O_3 thin films was achieved for c -, r -, m - and a -plane oriented Al_2O_3 substrates. The orientation of both Cr_2O_3 and $\alpha\text{-Ga}_2\text{O}_3$ thin film was the same as the respective substrate. For *ex situ* deposition of Ga_2O_3 , XRD measurements indicate the presence of the β -phase of Ga_2O_3 , which is less dominant as the still remaining α -phase. No optimization was performed for the deposition process, but the results serve as a proof of concept that the deposition of phase-pure $\alpha\text{-Ga}_2\text{O}_3$ – especially in the c - and r -orientation – is possible on Cr_2O_3 buffer layers.

(a)



(b)

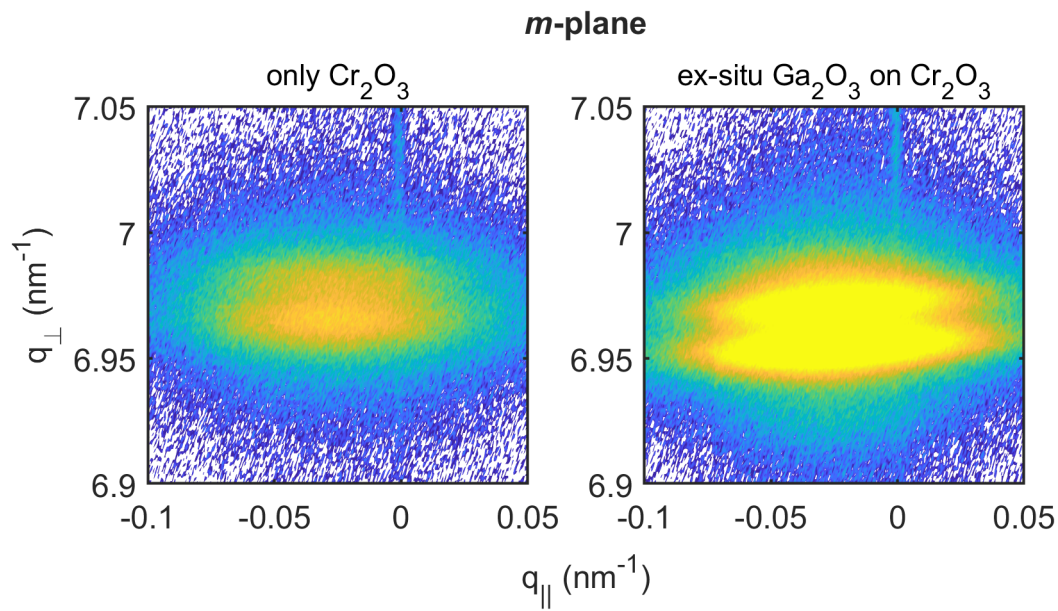


Figure 3.37: (a) $2\theta\text{-}\omega$ -patterns of the *m*-plane Cr_2O_3 reference sample A (black), as well as the *ex situ* (blue) and *in situ* (red) buffer layer structures. (b) RSM around the (30.0) reflection recorded before (left) and after (right) *ex situ* deposition of Ga_2O_3 on Cr_2O_3 .

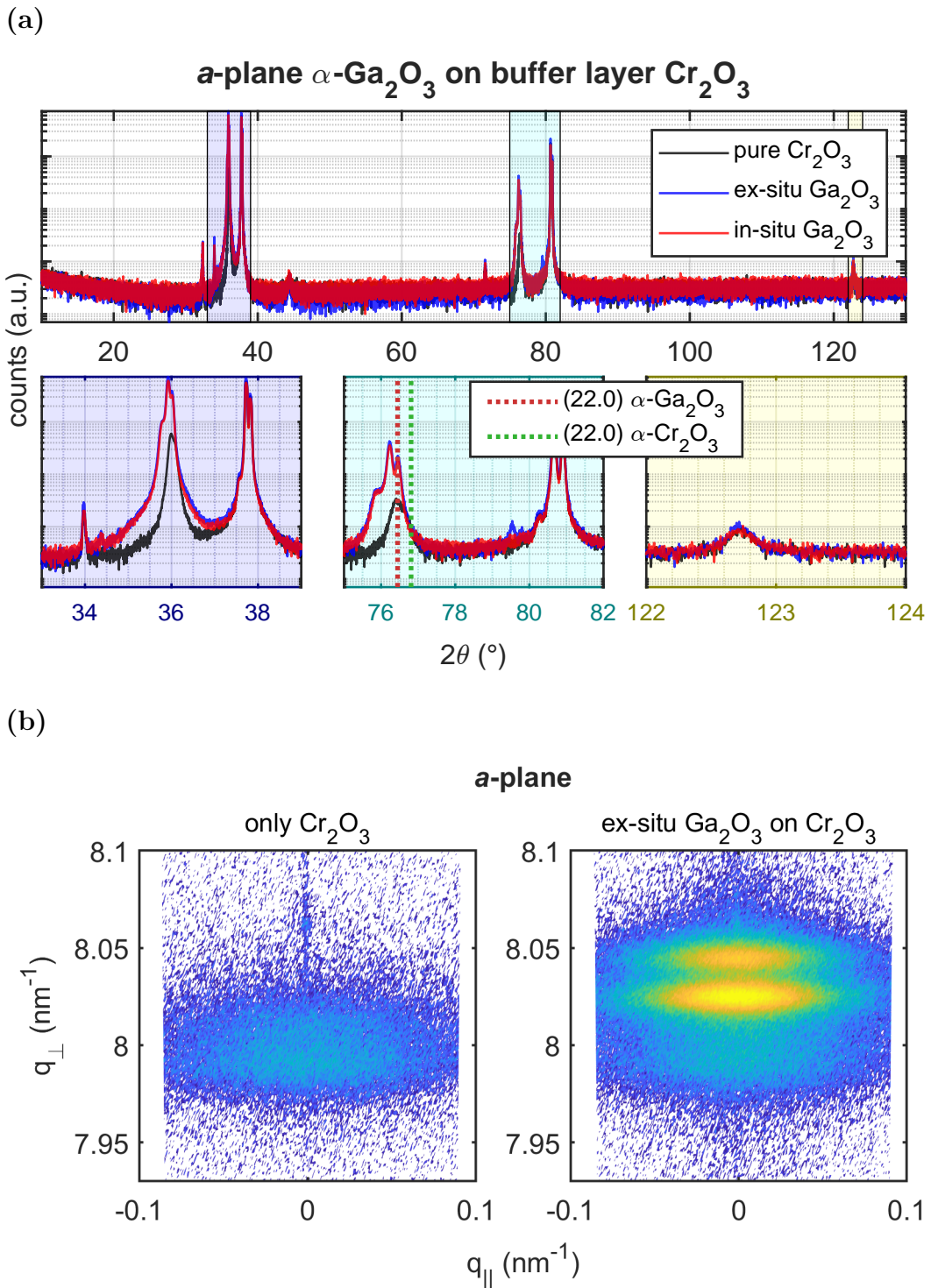


Figure 3.38: (a) $2\theta\text{-}\omega$ -patterns of the *a*-plane Cr_2O_3 reference sample A (black), as well as the *ex situ* (blue) and *in situ* (red) buffer layer structures. (b) RSM around the (22.0) reflection recorded before (left) and after (right) *ex situ* deposition of Ga_2O_3 on Cr_2O_3 .

Appendices

Appendix A

Calculations

In the following, Equ. 2.7 is applied:

$$d_{hkl} = \left(\frac{4}{3} \frac{h^2 + k^2 + hk}{a^2} + \frac{l^2}{c^2} \right)^{-1/2}.$$

A.1 *m*-plane lattice constants

The reflection $(30.\pm 6)$ is a superposition of out-of-plane (30.0) and in-plane $(00.\pm 6)$. The inverse lattice plane distances are

$$q_{\perp}^{(30.\pm 6)} = d_{(30.0)}^{-1} = \sqrt{\frac{4}{3} \frac{3^2}{a^2}} = \sqrt{12}/a, \quad (\text{A.1})$$

$$q_{\parallel}^{(30.\pm 6)} = d_{(00.\pm 6)}^{-1} = \sqrt{\frac{(\pm 6)^2}{c^2}} = 6/c. \quad (\text{A.2})$$

In the y -axis azimuth, $(4\bar{2}.0)$ is a superposition of out-of-plane (30.0) and in-plane $(1\bar{2}.0)$. Note that $(1\bar{2}.0)$ has a -plane character. The inverse lattice plane distances are

$$q_{\perp}^{(4\bar{2}.0)} = d_{(30.0)}^{-1} = \sqrt{12}/a, \quad (\text{A.3})$$

$$q_{\parallel}^{(4\bar{2}.0)} = d_{(1\bar{2}.0)}^{-1} = \sqrt{\frac{4}{3} \frac{1^2 + 2^2 - 2}{a^2}} = 2/a. \quad (\text{A.4})$$

Also in this azimuth, (22.0) is a superposition of out-of-plane (30.0) and in-plane $(\bar{1}2.0)$. The inverse lattice plane distances are

$$q_{\perp}^{(22.0)} = d_{(30.0)}^{-1} = \sqrt{12}/a, \quad (\text{A.5})$$

$$q_{\parallel}^{(22.0)} = d_{(\bar{1}2.0)}^{-1} = \sqrt{\frac{4}{3} \frac{1^2 + 2^2 - 2}{a^2}} = 2/a. \quad (\text{A.6})$$

A.2 *a*-plane lattice constants

The reflection $(22.\pm 6)$ is a superposition of out-of-plane (22.0) and in-plane $(00.\pm 6)$. The inverse lattice plane distances are

$$q_{\perp}^{(22.\pm 6)} = d_{(22.0)}^{-1} = \sqrt{\frac{4}{3} \frac{2^2 + 2^2 + 4}{a^2}} = 4/a, \quad (\text{A.7})$$

$$q_{\parallel}^{(22.\pm 6)} = d_{(00.\pm 6)}^{-1} = 6/c. \quad (\text{A.8})$$

In the y -axis azimuth, (30.0) cannot be represented as a superposition of in-plane and out-of-plane scattering vectors. This is due to the symmetry of the hexagonal lattice. But it is possible to represent it as a superposition of out-of-plane (11.0) and in-plane $(1\bar{1}.0)$, multiplied with a factor of 1.5 each. This leads to the calculation of inverse lattice planes via

$$q_{\perp}^{(30.0)} = \frac{3}{2} \cdot d_{1\bar{1}.0}^{-1} = \frac{3}{2} \sqrt{\frac{4}{3} \frac{1^2 + 1^2 - 1}{a^2}} = \frac{3}{2} \cdot \frac{2}{\sqrt{3}}/a = \sqrt{3}/a, \quad (\text{A.9})$$

$$q_{\parallel}^{(30.0)} = \frac{3}{2} \cdot d_{11.0}^{-1} = \frac{3}{2} \sqrt{\frac{4}{3} \frac{1^2 + 1^2 + 1}{a^2}} = \frac{3}{2} \cdot 2/a = 3/a. \quad (\text{A.10})$$

The same holds for the (03.0) reflection: it is a superposition of $(\bar{1}1.0)$ and (11.0) , multiplied by a factor of 1.5 and one obtains:

$$q_{\perp}^{(03.0)} = \frac{3}{2} \cdot d_{\bar{1}1.0}^{-1} = \sqrt{3}/a, \quad (\text{A.11})$$

$$q_{\parallel}^{(03.0)} = \frac{3}{2} \cdot d_{11.0}^{-1} = 3/a. \quad (\text{A.12})$$

Appendix B

Figures

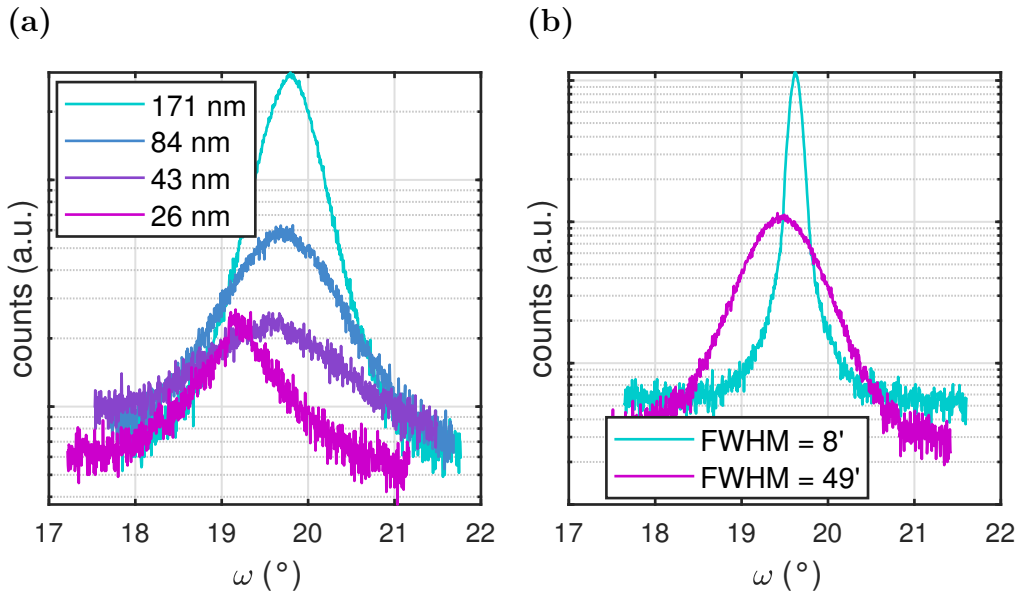


Figure B.1: (a) ω -patterns for c -plane oriented samples of the 1st batch in 3.3, fabricated with smallest laser spot size. (b) ω -patterns for two c -plane oriented samples from the 2nd batch in 3.3, that were fabricated with same fluence and had the same thickness of approx. 150 nm, but very different ω -FWHM.

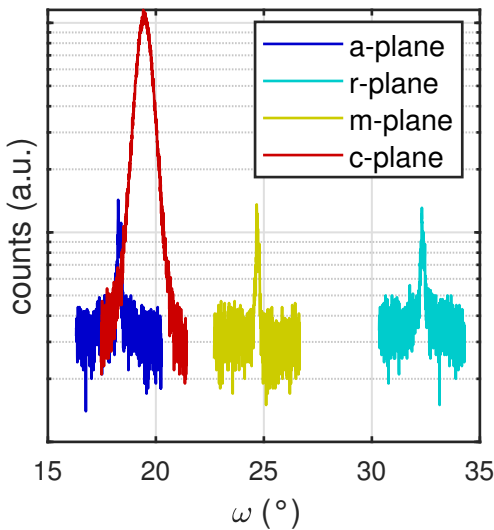


Figure B.2: ω -patterns for the samples of the process that yielded the c -plane sample with higher FWHM in Fig. B.1b. The patterns correspond to c - (red), r (cyan), m (yellow) and a -plane (blue).

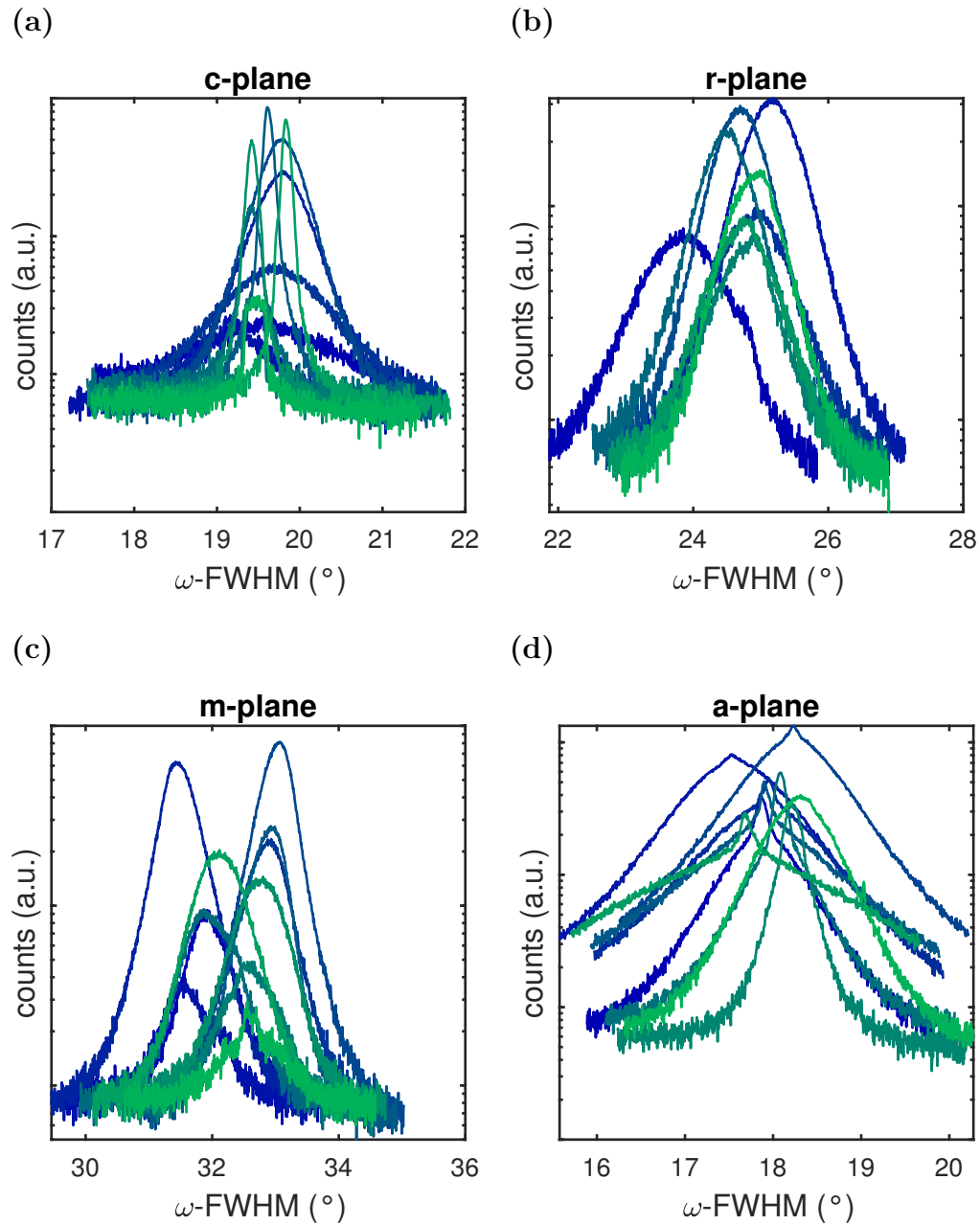


Figure B.3: Diffractogramms from ω -patterns for varying laser focus in 3.3.

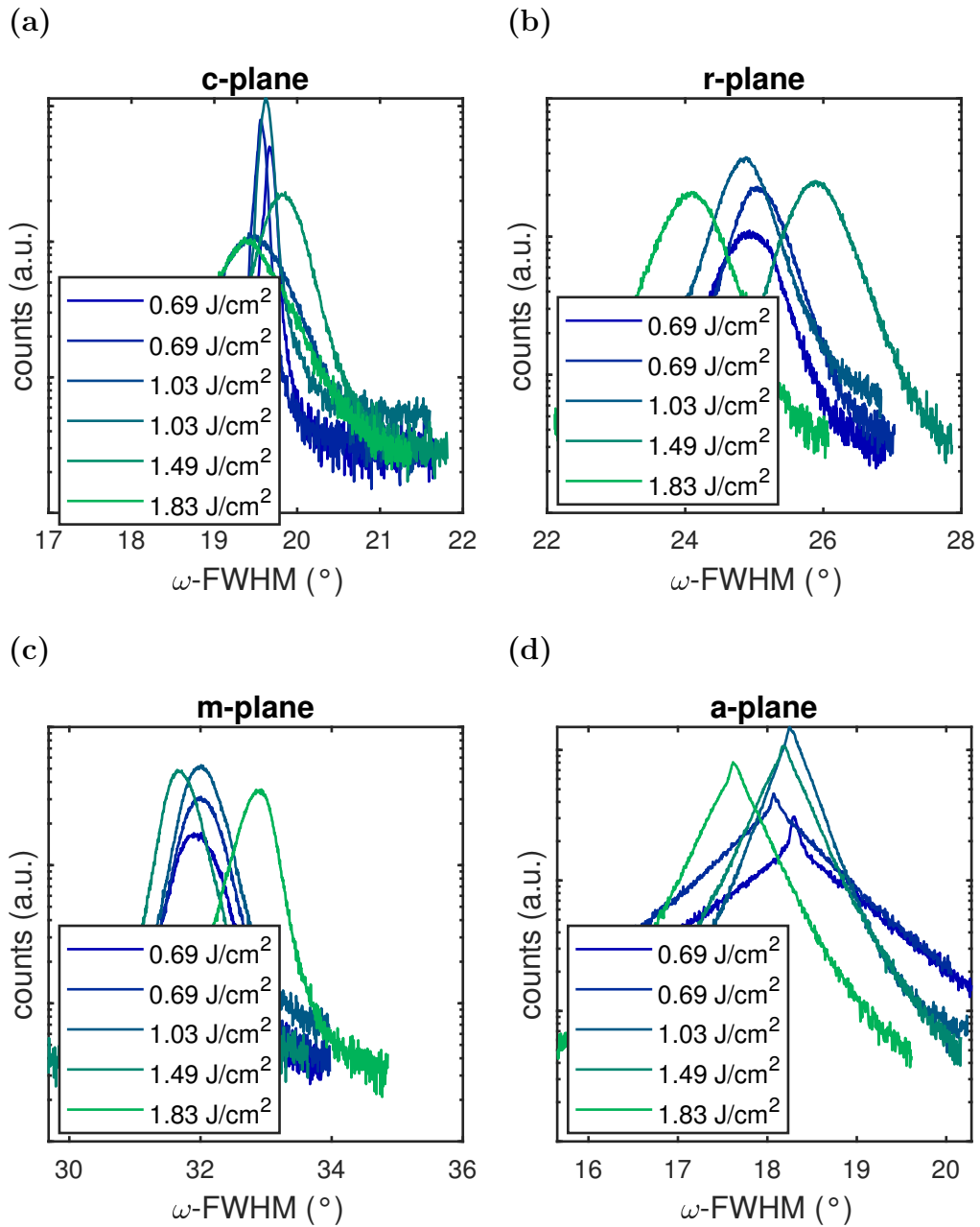


Figure B.4: Diffractogramms from ω -patterns for varying laser pulse energy in 3.3.

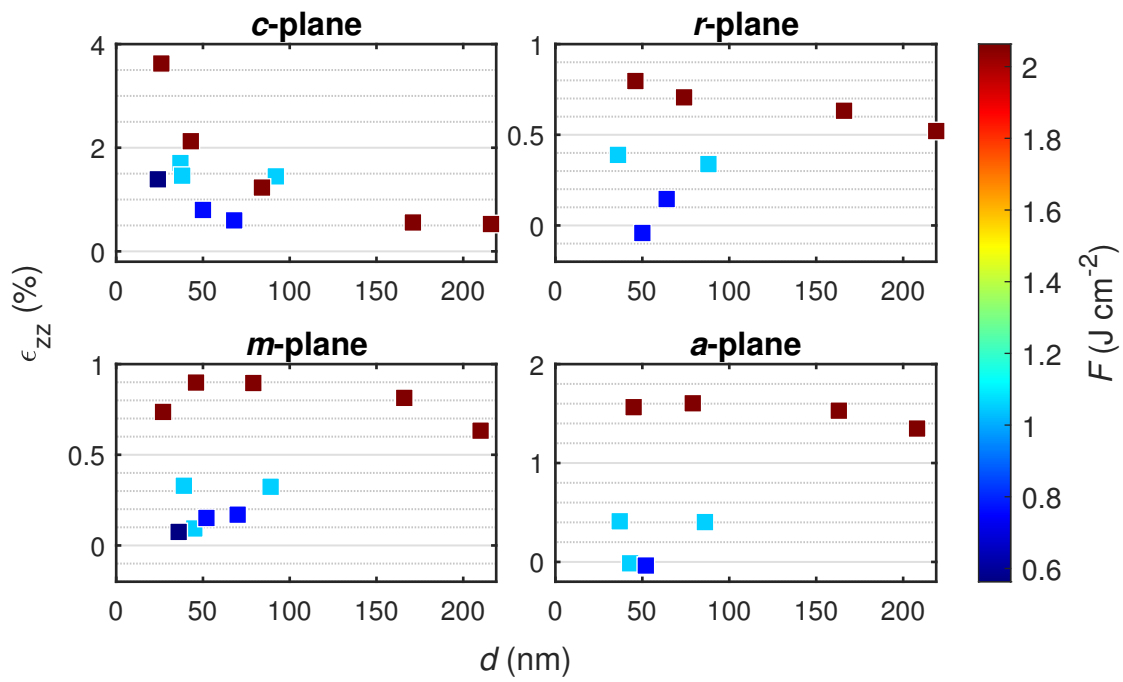


Figure B.5: Detailed view (cf. Fig. 3.22) of the o.o.p. strain for the samples of the 1st batch in 3.3.

Bibliography

- [1] David S. Ginley, ed. *Handbook of Transparent Conductors*. Boston, MA: Springer US, 2011. ISBN: 978-1-4419-1637-2 978-1-4419-1638-9. DOI: [10.1007/978-1-4419-1638-9](https://doi.org/10.1007/978-1-4419-1638-9).
- [2] C. Guillén and J. Herrero. “TCO/metal/TCO structures for energy and flexible electronics”. In: *Thin Solid Films* 520.1 (2011), pp. 1–17. ISSN: 00406090. DOI: [10.1016/j.tsf.2011.06.091](https://doi.org/10.1016/j.tsf.2011.06.091).
- [3] Harpreet Singh and Bharpur Singh. “A brief study of novel transparent conducting oxide (TCO) material”. In: 14th international conference on materials processing and characterization 2023. Hyderabad, India, 2024, p. 030164. DOI: [10.1063/5.0197252](https://doi.org/10.1063/5.0197252).
- [4] Ganesh T. Chavan *et al.* “A Brief Review of Transparent Conducting Oxides (TCO): The Influence of Different Deposition Techniques on the Efficiency of Solar Cells”. In: *Nanomaterials* 13.7 (2023), p. 1226. ISSN: 2079-4991. DOI: [10.3390/nano13071226](https://doi.org/10.3390/nano13071226).
- [5] Chiara Candelise, Jamie F. Speirs, and Robert J.K. Gross. “Materials availability for thin film (TF) PV technologies development: A real concern?” In: *Renewable and Sustainable Energy Reviews* 15.9 (2011), pp. 4972–4981. ISSN: 13640321. DOI: [10.1016/j.rser.2011.06.012](https://doi.org/10.1016/j.rser.2011.06.012).
- [6] Oleksiy Slobodyan *et al.* “Analysis of the dependence of critical electric field on semiconductor bandgap”. In: *Journal of Materials Research* 37.4 (2022), pp. 849–865. ISSN: 0884-2914, 2044-5326. DOI: [10.1557/s43578-021-00465-2](https://doi.org/10.1557/s43578-021-00465-2).
- [7] Man Hoi Wong *et al.* “Ultrawide-bandgap semiconductors: An overview”. In: *Journal of Materials Research* 36.23 (2021), pp. 4601–4615. ISSN: 0884-2914, 2044-5326. DOI: [10.1557/s43578-021-00458-1](https://doi.org/10.1557/s43578-021-00458-1).
- [8] Anna Hassa, Marius Grundmann, and Holger Von Wenckstern. “Progression of group-III sesquioxides: epitaxy, solubility and desorption”. In: *Journal of Physics D: Applied Physics* 54.22 (2021), p. 223001. ISSN: 0022-3727, 1361-6463. DOI: [10.1088/1361-6463/abd4a4](https://doi.org/10.1088/1361-6463/abd4a4).
- [9] S.I. Stepanov *et al.* “HVPE growth of corundum-structured α -Ga₂O₃ on sapphire substrates with α -Cr₂O₃ buffer layer”. In: *Materials Physics and Mechanics* 47 (2021), pp. 577–581. DOI: [10.18149/MPM.4742021_4](https://doi.org/10.18149/MPM.4742021_4).
- [10] Kentaro Kaneko, Taichi Nomura, and Shizuo Fujita. “Corundum-structured α -phase Ga₂O₃-Cr₂O₃-Fe₂O₃ alloy system for novel functions”. In: *Phys. Status Solidi C* 7.10 (2010), pp. 2467–2470. ISSN: 1610-1642. DOI: [10.1002/pssc.200983896](https://doi.org/10.1002/pssc.200983896).

- [11] N. Uekawa and K. Kaneko. “Dopant Reduction in *p*-Type Oxide Films upon Oxygen Absorption”. In: *The Journal of Physical Chemistry* 100.10 (1996), pp. 4193–4198. ISSN: 0022-3654, 1541-5740. DOI: [10.1021/jp952784m](https://doi.org/10.1021/jp952784m).
- [12] P. S. Robbert *et al.* “Novel electronic and magnetic properties of ultrathin chromium oxide films grown on Pt(111)”. In: *Journal of Vacuum Science & Technology A: Vacuum, Surfaces, and Films* 16.3 (1998), pp. 990–995. ISSN: 0734-2101, 1520-8559. DOI: [10.1116/1.581283](https://doi.org/10.1116/1.581283).
- [13] M.F. Al-Kuhaili and S.M.A. Durrani. “Optical properties of chromium oxide thin films deposited by electron-beam evaporation”. In: *Optical Materials* 29.6 (2007), pp. 709–713. ISSN: 09253467. DOI: [10.1016/j.optmat.2005.11.020](https://doi.org/10.1016/j.optmat.2005.11.020).
- [14] François Lebreau *et al.* “Structural, Magnetic, Electronic, Defect, and Diffusion Properties of Cr₂O₃: A DFT+U Study”. In: *The Journal of Physical Chemistry C* 118.31 (2014), pp. 18133–18145. ISSN: 1932-7447. DOI: [10.1021/jp5039943](https://doi.org/10.1021/jp5039943).
- [15] Zhishan Mi *et al.* “The effects of strain and vacancy defects on the electronic structure of Cr₂O₃”. In: *Computational Materials Science* 144 (2018), pp. 64–69. ISSN: 09270256. DOI: [10.1016/j.commatsci.2017.12.012](https://doi.org/10.1016/j.commatsci.2017.12.012).
- [16] R. W. G. Wyckoff. *Crystal structures*. New York, London, Sydney: Interscience Publishers, 1963. 467 pp.
- [17] James F. Shackelford and William Alexander, eds. *Crc materials science and engineering handbook*. 0th ed. CRC Press, 2000. URL: <https://doi.org/10.1201/9781420038408>.
- [18] F. D. Lai *et al.* “Ultrathin TiO₂ amorphous films for high transmittance APSM blanks at 157 and 193 nm wavelength simultaneously”. In: *Journal of Vacuum Science & Technology B: Microelectronics and Nanometer Structures Processing, Measurement, and Phenomena* 21.6 (2003), pp. 3062–3066. ISSN: 1071-1023, 1520-8567. DOI: [10.1116/1.1624252](https://doi.org/10.1116/1.1624252).
- [19] Jun C. Nable, Steven L. Suib, and Francis S. Galasso. “Metal organic chemical vapor deposition of Al₂O₃ and Cr₂O₃ on nickel as oxidation barriers”. In: *Surface and Coatings Technology* 186.3 (2004), pp. 423–430. ISSN: 02578972. DOI: [10.1016/j.surfcoat.2003.11.022](https://doi.org/10.1016/j.surfcoat.2003.11.022).
- [20] Chun-Shen Cheng, H. Gomi, and H. Sakata. “Electrical and Optical Properties of Cr₂O₃ Films Prepared by Chemical Vapour Deposition”. In: *Physica Status Solidi (a)* 155.2 (1996), pp. 417–425. ISSN: 00318965, 1521396X. DOI: [10.1002/pssa.2211550215](https://doi.org/10.1002/pssa.2211550215).
- [21] Cecilia Guillén and José Herrero. “Structural Changes Induced by Heating in Sputtered NiO and Cr₂O₃ Thin Films as *p*-Type Transparent Conductive Electrodes”. In: *Electronic Materials* 2.2 (2021), pp. 49–59. ISSN: 2673-3978. DOI: [10.3390/electronicmat2020005](https://doi.org/10.3390/electronicmat2020005).
- [22] M. Catti *et al.* “Electronic, magnetic and crystal structure of Cr₂O₃ by theoretical methods”. In: *Journal of Physics and Chemistry of Solids* 57.11 (1996), pp. 1735–1741. ISSN: 00223697. DOI: [10.1016/0022-3697\(96\)00034-0](https://doi.org/10.1016/0022-3697(96)00034-0).

- [23] Aoife B Kehoe *et al.* “Assessing the potential of Mg-doped Cr₂O₃ as a novel *p*-type transparent conducting oxide”. In: *Journal of Physics: Condensed Matter* 28.12 (2016), p. 125501. ISSN: 0953-8984, 1361-648X. DOI: [10.1088/0953-8984/28/12/125501](https://doi.org/10.1088/0953-8984/28/12/125501).
- [24] Larry W. Finger and Robert M. Hazen. “Crystal structure and isothermal compression of Fe₂O₃, Cr₂O₃, and V₂O₃ to 50 kbars”. In: *Journal of Applied Physics* 51.10 (1980), pp. 5362–5367. ISSN: 0021-8979, 1089-7550. DOI: [10.1063/1.327451](https://doi.org/10.1063/1.327451).
- [25] Elisabetta Arca *et al.* “Effect of Chemical Precursors On the Optical and Electrical Properties of *p*-Type Transparent Conducting Cr₂O₃:(Mg,N)”. In: *The Journal of Physical Chemistry C* 117.42 (2013), pp. 21901–21907. ISSN: 1932-7447. DOI: [10.1021/jp404230k](https://doi.org/10.1021/jp404230k).
- [26] Valerian Pishchik, Leonid A. Lytvynov, and Elena R. Dobrovinskaya. *Sapphire: Material, Manufacturing, Applications*. Boston, MA: Springer US, 2009. ISBN: 978-0-387-85694-0 978-0-387-85695-7. DOI: [10.1007/978-0-387-85695-7](https://doi.org/10.1007/978-0-387-85695-7).
- [27] M. Marezio and J. P. Remeika. “Bond lengths in the α -Ga₂O₃ structure and the high-pressure phase of Ga_{2-x}Fe_xO₃”. In: *The Journal of Chemical Physics* 46.5 (1967), pp. 1862–1865. ISSN: 0021-9606, 1089-7690. DOI: [10.1063/1.1840945](https://doi.org/10.1063/1.1840945).
- [28] Ruihua Cheng, C.N. Borca, and P.A. Dowben. “Selective Area Chemical Vapor Deposition of Chromium Oxides”. In: *MRS Proceedings* 614 (2000), F10.4.1. ISSN: 0272-9172, 1946-4274. DOI: [10.1557/PROC-614-F10.4.1](https://doi.org/10.1557/PROC-614-F10.4.1).
- [29] Ruihua Cheng *et al.* “Potential phase control of chromium oxide thin films prepared by laser-initiated organometallic chemical vapor deposition”. In: *Applied Physics Letters* 78.4 (2001), pp. 521–523. ISSN: 0003-6951, 1077-3118. DOI: [10.1063/1.1343846](https://doi.org/10.1063/1.1343846).
- [30] L. Farrell *et al.* “Conducting mechanism in the epitaxial *p*-type transparent conducting oxide Cr₂O₃:Mg”. In: *Physical Review B* 91.12 (2015), p. 125202. ISSN: 1098-0121, 1550-235X. DOI: [10.1103/PhysRevB.91.125202](https://doi.org/10.1103/PhysRevB.91.125202).
- [31] E. Arca, K. Fleischer, and I. V. Shvets. “Magnesium, nitrogen codoped Cr₂O₃: A *p*-type transparent conducting oxide”. In: *Applied Physics Letters* 99.11 (2011), p. 111910. ISSN: 0003-6951. DOI: [10.1063/1.3638461](https://doi.org/10.1063/1.3638461).
- [32] Alexander Polyakov *et al.* “Electrical properties of α -Ga₂O₃ films grown by halide vapor phase epitaxy on sapphire with α -Cr₂O₃ buffers”. In: *Journal of Applied Physics* 131.21 (2022), p. 215701. ISSN: 0021-8979, 1089-7550. DOI: [10.1063/5.0090832](https://doi.org/10.1063/5.0090832).
- [33] Alexander Polyakov *et al.* “Effects of sapphire substrate orientation on Sn-doped α -Ga₂O₃ grown by halide vapor phase epitaxy using α -Cr₂O₃ buffers”. In: *Journal of Physics D: Applied Physics* 55.49 (2022), p. 495102. ISSN: 0022-3727, 1361-6463. DOI: [10.1088/1361-6463/ac962f](https://doi.org/10.1088/1361-6463/ac962f).
- [34] Anna Caricato *et al.* “Deposition of chromium oxide thin films with large thermoelectromotive force coefficient by reactive pulsed laser ablation”. In: *Journal of Optoelectronics and Advanced Materials* 12 (2010), p. 427.

- [35] Sandhyarani Punugupati, Jagdish Narayan, and Frank Hunte. “Room temperature ferromagnetism in epitaxial Cr₂O₃ thin films grown on r-sapphire”. In: *Journal of Applied Physics* 117.19 (2015), p. 193907. ISSN: 0021-8979, 1089-7550. DOI: [10.1063/1.4921435](https://doi.org/10.1063/1.4921435).
- [36] Jarnail Singh *et al.* “Structural, optical and electrical characterization of epitaxial Cr₂O₃ thin film deposited by PLD”. In: *Materials Research Express* 6.10 (2019), p. 106406. ISSN: 2053-1591. DOI: [10.1088/2053-1591/ab3543](https://doi.org/10.1088/2053-1591/ab3543).
- [37] Elisabetta Arca *et al.* “Valence band modification of Cr₂O₃ by Ni-doping: creating a high figure of merit *p*-type TCO”. In: *Journal of Materials Chemistry C* 5.47 (2017), pp. 12610–12618. ISSN: 2050-7534. DOI: [10.1039/C7TC03545D](https://doi.org/10.1039/C7TC03545D).
- [38] M. Tabbal *et al.* “Pulsed laser deposition of nanostructured dichromium trioxide thin films”. In: *Thin Solid Films* 515.4 (2006), pp. 1976–1984. ISSN: 00406090. DOI: [10.1016/j.tsf.2006.08.010](https://doi.org/10.1016/j.tsf.2006.08.010).
- [39] Ruihua Cheng *et al.* “Characterization of the native Cr₂O₃ oxide surface of CrO₂”. In: *Applied Physics Letters* 79.19 (2001), pp. 3122–3124. ISSN: 0003-6951, 1077-3118. DOI: [10.1063/1.1416474](https://doi.org/10.1063/1.1416474).
- [40] P. Kofstad and K. P. Lillerud. “On High Temperature Oxidation of Chromium: II . Properties of and the Oxidation Mechanism of Chromium”. In: *Journal of The Electrochemical Society* 127.11 (1980), pp. 2410–2419. ISSN: 0013-4651, 1945-7111. DOI: [10.1149/1.2129481](https://doi.org/10.1149/1.2129481).
- [41] W. C. Hagel. “Electrical Conductivity of Li-Substituted Cr₂O₃”. In: *Journal of Applied Physics* 36.8 (1965), pp. 2586–2587. ISSN: 0021-8979, 1089-7550. DOI: [10.1063/1.1714536](https://doi.org/10.1063/1.1714536).
- [42] G. M. Crosbie *et al.* “Electronically Conducting Doped Chromium Oxides”. In: *Journal of the American Ceramic Society* 67.7 (1984), pp. 498–503. ISSN: 0002-7820, 1551-2916. DOI: [10.1111/j.1151-2916.1984.tb19642.x](https://doi.org/10.1111/j.1151-2916.1984.tb19642.x).
- [43] A Holt and P Kofstad. “Electrical conductivity and defect structure of Cr₂O₃. II. Reduced temperatures (<~1000 °C)”. In: *Solid State Ionics* 69.2 (1994), pp. 137–143. ISSN: 01672738. DOI: [10.1016/0167-2738\(94\)90402-2](https://doi.org/10.1016/0167-2738(94)90402-2).
- [44] Robert Schewski *et al.* “Epitaxial stabilization of pseudomorphic α-Ga₂O₃ on sapphire (0001)”. In: *Applied Physics Express* 8.1 (2015), p. 011101. ISSN: 1882-0778, 1882-0786. DOI: [10.7567/APEX.8.011101](https://doi.org/10.7567/APEX.8.011101).
- [45] Clemens Petersen *et al.* “PLD of α-Ga₂O₃ on m-plane Al₂O₃: Growth regime, growth process, and structural properties”. In: *APL Materials* 11.6 (2023), p. 061122. ISSN: 2166-532X. DOI: [10.1063/5.0149797](https://doi.org/10.1063/5.0149797).
- [46] Kentaro Kaneko *et al.* “Progress in α-Ga₂O₃ for practical device applications”. In: *Japanese Journal of Applied Physics* 62 (SF 2023), SF0803. ISSN: 0021-4922, 1347-4065. DOI: [10.35848/1347-4065/acd125](https://doi.org/10.35848/1347-4065/acd125).
- [47] S. J. Pearton *et al.* “A review of Ga₂O₃ materials, processing, and devices”. In: *Applied Physics Reviews* 5.1 (2018), p. 011301. ISSN: 1931-9401. DOI: [10.1063/1.5006941](https://doi.org/10.1063/1.5006941).

- [48] Duyoung Yang *et al.* “Epitaxial growth of alpha gallium oxide thin films on sapphire substrates for electronic and optoelectronic devices: progress and perspective”. In: *Electronic Materials Letters* 18.2 (2022), pp. 113–128. ISSN: 1738-8090, 2093-6788. DOI: [10.1007/s13391-021-00333-5](https://doi.org/10.1007/s13391-021-00333-5).
- [49] Kentaro Kaneko *et al.* “Evaluation of misfit relaxation in α -Ga₂O₃ epitaxial growth on α -Al₂O₃ substrate”. In: *Japanese Journal of Applied Physics* 51 (2R 2012), p. 020201. ISSN: 0021-4922, 1347-4065. DOI: [10.1143/JJAP.51.020201](https://doi.org/10.1143/JJAP.51.020201).
- [50] Sofie Vogt *et al.* “Realization of Conductive n-Type Doped α -Ga₂O₃ on *m*-Plane Sapphire Grown by a Two-Step Pulsed Laser Deposition Process”. In: *physica status solidi (a)* 220.3 (2023), p. 2200721. ISSN: 1862-6300, 1862-6319. DOI: [10.1002/pssa.202200721](https://doi.org/10.1002/pssa.202200721).
- [51] Rien Jinno *et al.* “Reduction in edge dislocation density in corundum-structured α -Ga₂O₃ layers on sapphire substrates with quasi-graded α -(Al,Ga)₂O₃ buffer layers”. In: *Applied Physics Express* 9.7 (2016), p. 071101. ISSN: 1882-0778, 1882-0786. DOI: [10.7567/APEX.9.071101](https://doi.org/10.7567/APEX.9.071101).
- [52] Rien Jinno *et al.* “Crystal orientation dictated epitaxy of ultrawide-bandgap 5.4- to 8.6-eV α -(AlGa)₂O₃ on *m*-plane sapphire”. In: *Science Advances* 7.2 (2021), eabd5891. ISSN: 2375-2548. DOI: [10.1126/sciadv.abd5891](https://doi.org/10.1126/sciadv.abd5891).
- [53] Kazuaki Akaiwa *et al.* “Electrical properties of sn-doped α -ga₂o₃ films on *m*-plane sapphire substrates grown by mist chemical vapor deposition”. In: *physica status solidi (a)* 217.3 (2020), p. 1900632. ISSN: 1862-6300, 1862-6319. DOI: [10.1002/pssa.201900632](https://doi.org/10.1002/pssa.201900632).
- [54] Anna Hassa *et al.* “Control of phase formation of (Al_xGa_{1-x})₂O₃ thin films on *c*-plane Al₂O₃”. In: *Journal of Physics D: Applied Physics* 53.48 (2020), p. 485105. ISSN: 0022-3727, 1361-6463. DOI: [10.1088/1361-6463/abaf7d](https://doi.org/10.1088/1361-6463/abaf7d).
- [55] S. Vogt *et al.* “Zr doping in pulsed-laser-deposited α -Ga₂O₃ for device applications”. In: *Physical Review Applied* 21.6 (2024), p. 064016. ISSN: 2331-7019. DOI: [10.1103/PhysRevApplied.21.064016](https://doi.org/10.1103/PhysRevApplied.21.064016).
- [56] Neil W. Ashcroft and N. David Mermin. *Solid State Physics*. Saunders College Publishing, 1976. 826 pp.
- [57] Marius Grundmann and Michael Lorenz. “Azimuthal anisotropy of rhombohedral (corundum phase) heterostructures”. In: *physica status solidi (b)* 258.7 (2021), p. 2100104. ISSN: 1521-3951. DOI: [10.1002/pssb.202100104](https://doi.org/10.1002/pssb.202100104).
- [58] George F. Harrington and José Santiso. “Back-to-Basics tutorial: X-ray diffraction of thin films”. In: *Journal of Electroceramics* 47.4 (2021), pp. 141–163. ISSN: 1385-3449, 1573-8663. DOI: [10.1007/s10832-021-00263-6](https://doi.org/10.1007/s10832-021-00263-6).
- [59] Lothar Spieß, ed. *Moderne Röntgenbeugung: Röntgendiffraktometrie für Materialwissenschaftler, Physiker und Chemiker*. 2., überarb. und erw. Aufl. Studium. Wiesbaden: Vieweg + Teubner, 2009. 564 pp. ISBN: 978-3-8351-0166-1.
- [60] L. D. Landau and E. M. Lifshitz. *Theory of Elasticity*. Course of Theoretical Physics vol. 7. Pergamon Press Ltd., 1970. 165 pp. ISBN: 978-0-08-057069-3.

- [61] Marius Grundmann. “Elastic theory of pseudomorphic monoclinic and rhombohedral heterostructures”. In: *Journal of Applied Physics* 124.18 (2018), p. 185302. ISSN: 0021-8979, 1089-7550. DOI: [10.1063/1.5045845](https://doi.org/10.1063/1.5045845).
- [62] H.L. Alberts and J.C.A. Boeyens. “The elastic constants and distance dependence of the magnetic interactions of Cr₂O₃”. In: *Journal of Magnetism and Magnetic Materials* 2.4 (1976), pp. 327–333. ISSN: 03048853. DOI: [10.1016/0304-8853\(76\)90044-5](https://doi.org/10.1016/0304-8853(76)90044-5).
- [63] Marius Grundmann. “A most general and facile recipe for the calculation of heteroepitaxial strain”. In: *physica status solidi (b)* 257.12 (2020), p. 2000323. ISSN: 0370-1972, 1521-3951. DOI: [10.1002/pssb.202000323](https://doi.org/10.1002/pssb.202000323).
- [64] Max Kneiß *et al.* “Strain states and relaxation for α -(Al_xGa_{1-x})₂O₃ thin films on prismatic planes of α -Al₂O₃ in the full composition range: Fundamental difference of a- and m-epitaxial planes in the manifestation of shear strain and lattice tilt”. In: *Journal of Materials Research* 36.23 (2021), pp. 4816–4831. ISSN: 0884-2914, 2044-5326. DOI: [10.1557/s43578-021-00375-3](https://doi.org/10.1557/s43578-021-00375-3).
- [65] Marius Grundmann. *The Physics of Semiconductors: An Introduction Including Nanophysics and Applications*. Graduate Texts in Physics. Cham: Springer International Publishing, 2016. ISBN: 978-3-319-23879-1 978-3-319-23880-7. URL: <http://link.springer.com/10.1007/978-3-319-23880-7>.
- [66] Derek Hull and D. J. Bacon. *Introduction to Dislocations*. 5th ed. Elsevier Ltd., 2011. 268 pp. ISBN: 978-0-08-096673-1.
- [67] M. Grundmann and M. Lorenz. “Anisotropic strain relaxation through prismatic and basal slip in α -(Al, Ga)₂O₃ on R-plane Al₂O₃”. In: *APL Materials* 8.2 (2020), p. 021108. ISSN: 2166-532X. DOI: [10.1063/1.5144744](https://doi.org/10.1063/1.5144744).
- [68] M. Grundmann, T. Stralka, and M. Lorenz. “Epitaxial growth and strain relaxation of corundum-phase (Al,Ga)₂O₃ thin films from pulsed laser deposition at 1000 °C on r-plane Al₂O₃”. In: *Applied Physics Letters* 117.24 (2020), p. 242102. ISSN: 0003-6951, 1077-3118. DOI: [10.1063/5.0030675](https://doi.org/10.1063/5.0030675).
- [69] Michael Lorenz. “Pulsed laser deposition”. In: *Encyclopedia of Applied Physics*. Wiley, 2019. URL: <http://dx.doi.org/10.1002/3527600434.eap810>.
- [70] Holger von Wenckstern *et al.* “A review of the segmented-target approach to combinatorial material synthesis by pulsed-laser deposition”. In: *Phy. Status Solidi B* 257.7 (2020), p. 1900626. ISSN: 0370-1972, 1521-3951. DOI: [10.1002/pssb.201900626](https://doi.org/10.1002/pssb.201900626).
- [71] V. Srikant, J. S. Speck, and D. R. Clarke. “Mosaic structure in epitaxial thin films having large lattice mismatch”. In: *Journal of Applied Physics* 82.9 (1997), pp. 4286–4295. ISSN: 0021-8979, 1089-7550. DOI: [10.1063/1.366235](https://doi.org/10.1063/1.366235).
- [72] L. J. van der Pauw. “A method of measuring specific resistivity and Hall effect of discs of arbitrary shape”. In: *Philips Research Reports* 13.1 (1958), pp. 1–9.
- [73] Hiroyuki Fujiwara. *Spectroscopic Ellipsometry. Principles and Applications*. Tōkyō: John Wiley & Sons, Ltd, 2007. ISBN: 978-4-621-07253-0.

- [74] J.C. Manifacier *et al.* “Optical and electrical properties of SnO₂ thin films in relation to their stoichiometric deviation and their crystalline structure”. In: *Thin Solid Films* 41.2 (1977), pp. 127–135. ISSN: 00406090. DOI: [10 . 1016 / 0040 - 6090\(77\)90395 - 9](https://doi.org/10.1016/0040-6090(77)90395-9).
- [75] A. R. Zanatta. “Revisiting the optical bandgap of semiconductors and the proposal of a unified methodology to its determination”. In: *Scientific Reports* 9.1 (2019), p. 11225. ISSN: 2045-2322. DOI: [10 . 1038 / s41598 - 019 - 47670 - y](https://doi.org/10.1038/s41598-019-47670-y).
- [76] Jan Tauc. “Optical properties of amorphous semiconductors and solar cells”. In: *Fundamentals of Semiconductors*. 3rd ed. Berlin, Heidelberg: Springer, 2005. ISBN: 3-540-41323-5.
- [77] Alex Dolgonos, Thomas O. Mason, and Kenneth R. Poeppelmeier. “Direct optical band gap measurement in polycrystalline semiconductors: A critical look at the Tauc method”. In: *Journal of Solid State Chemistry* 240 (2016), pp. 43–48. ISSN: 00224596. DOI: [10 . 1016 / j . jssc . 2016 . 05 . 010](https://doi.org/10.1016/j.jssc.2016.05.010).
- [78] Mohamed A. Hafez, Mohamed K. Zayed, and Hani E. Elsayed-Ali. “Review: Geometric interpretation of reflection and transmission RHEED patterns”. In: *Micron* 159 (2022), p. 103286. ISSN: 09684328. DOI: [10 . 1016 / j . micron . 2022 . 103286](https://doi.org/10.1016/j.micron.2022.103286).
- [79] Anubhav Jain *et al.* “Commentary: The Materials Project: A materials genome approach to accelerating materials innovation”. In: *APL Materials* 1.1 (2013), p. 011002. ISSN: 2166-532X. DOI: [10 . 1063 / 1 . 4812323](https://doi.org/10.1063/1.4812323).